Studies of seismic deconvolution and low-frequency earthquakes

by

Alexandra Amélie Royer

B. Sc. Université Joseph Fourier, 2007

M. Sc. Université Joseph Fourier, 2009

A THESIS SUBMITTED IN PARTIAL FULFILLMENT OF
THE REQUIREMENTS FOR THE DEGREE OF

DOCTOR OF PHILOSOPHY

in

The Faculty of Graduate and Postdoctoral Studies

(Geophysics)

THE UNIVERSITY OF BRITISH COLUMBIA

(Vancouver)

August 2014

Abstract

Deconvolution of seismic data is an important component of signal processing that aims to remove the seismic source from seismograms, thereby isolating the Green's function. By considering seismograms of multiple earthquakes from similar locations recorded at a given station and that therefore share the same Green's function, we investigate a system of equations where the unknowns are the sources and source durations. Our solution is derived using direct linear inversion to recover the sources and Newton's method to recover source durations. For the short seismogram durations considered, we are able to recover source time functions for noise levels at 1% of the direct P-wave amplitude. However, the nonlinearity of the problem renders the system expensive to solve and sensitive to noise; therefore consideration is limited to short seismograms with high signal-to-noise ratio (SNR). When SNR levels are low, but a large multiplicity of seismograms representing a common source-receiver path are available, we can apply a different deconvolution approach to recover the Green's function. In an application to tectonic tremor in northern Cascadia, we implement an iterative blind deconvolution method that involves correlation, threshold detection and stacking of 1000's of low frequency earthquakes (LFEs) that form part of tremor to generate templates that can be considered as empirical Green's functions. We exploit this identification to compute hypocentres and moment tensors. LFE hypocentres follow the general epicentral distribution of tremor and occur along tightly defined surfaces in depth. The majority of mechanisms are consistent with shallow thrusting in the direction of plate motion. We analyze the influence of ocean tides on the triggering of LFEs and find a spatially variable sensitivity to tidally induced up-dip shear stress (UDSS), suggesting that tidal sensitivity must partially depend on laterally heterogeneous physical properties. The majority of LFEs fail during positive and increasing UDSS, consistent with combined contributions from background slow slip and from tides acting directly on LFEs. We identified rapid tremor reversals in southern Vancouver Island with higher sensitivity to UDSS than the main front and which at least partially explains an observed increase in LFE sensitivity to UDSS with time.

Preface

All of the work presented herein was carried out at The University of British Columbia by me, with advice, supervision and editorial authorship by my supervisor, Michael Bostock. My thesis committee (Catherine Johnson, Eldad Haber and Andrew Calvert) provided comments and suggestions during committee meetings and in personal discussions.

Chapter 2 has been published as *Royer, A. A., M. G. Bostock and E. Haber (2012), Blind deconvolution of seismograms regularized via minimum support, Inverse problems, 28, 127,010, doi:10.1088/0266-5611/28/12/125010.* It is reproduced unmodified, except for formatting changes and minor corrections for clarity. I was the lead author and was responsible for the analysis of the data and composition of the paper. Michael Bostock and Eldad Haber provided feedback, advice and editorial supervision throughout the development of this paper.

Chapter 3 has been published as *Royer, A. A. and M. G. Bostock (2013), A comparative study of low frequency earthquake templates in northern Cascadia, Earth Planet. Sci. Lett., doi:10.1016/j.epsl.2013.08.040.* It is reproduced unmodified, except for formatting changes and minor corrections for clarity. I was the lead author and was responsible for the analysis of the data and composition of the paper. Michael Bostock provided feedback, advice and editorial supervision throughout the development of this paper.

Chapter 4 has been submitted in July 2014, entitled "Tidal modulation of low frequency earthquakes and triggering of secondary events in northern Cascadia". I am the lead author and I am responsible for the analysis of the data and composition of the paper. Co-author Amanda Thomas from Stanford University, California, provided data, technical advice and editorial supervision. Michael Bostock provided feedback, advice and editorial supervision throughout the development of this paper.

Table of Contents

Abstract ii
Preface iii
Table of Contents iv
List of Tables vi
List of Figures vii
List of Abbreviations viii
List of Symbols ix
Acknowledgements xii

1 Introduction 1
1.1 Research objectives 1
1.2 Overview of deconvolution approaches 2
1.3 Tectonic context of the northern Cascadia subduction zone 4
1.3.1 Overview 4
1.3.2 Tremor, slow slip and low frequency earthquakes 7
1.3.3 Earth tides and low frequency earthquakes 9
1.3.4 Rapid tremor reversals 10

2 Blind deconvolution of seismograms regularized via minimum support 11
2.1 Introduction 11
2.2 Problem formulation 13
2.3 Methodology 16
2.3.1 Source duration 16
2.3.2 Introduction of source durations as unknowns 16
2.3.3 Combined system 18
2.3.4 Separation of variables 18
2.3.5 Stopping criterion 21
2.4 Algorithm 23
2.5 Results 23
2.6 Conclusion 28

3 A comparative study of low frequency earthquake templates in northern Cascadia 35
3.1 Introduction 35
3.2 Data 36
3.2.1 Washington state 36
3.2.2 Vancouver Island 37
3.3 Data Processing 37
3.3.1 Network autocorrelation 39
3.3.2 Waveform-correlation cluster analysis 39
3.3.3 Network cross-correlation 40
3.4 LFE templates as empirical Green's functions 40
3.5 LFE template locations 44
3.6 LFE template moment tensors 47

3.7 Discussion and conclusions 49

4 Tidal modulation of low frequency earthquakes and triggering of secondary events in northern Cascadia 58
4.1 Introduction 58
4.2 Data 60
4.3 Methodology 62
4.3.1 Tidal model 62
4.3.2 LFE correlation with tidal stress 64
4.3.3 Time dependent tidal sensitivity 71
4.3.4 Tidal sensitivity of rapid tremor reversals vs the main front . . . 73
4.3.5 Diurnal variation of LFE occurrence 77
4.4 Results 78
4.4.1 LFE correlation with tidal stress 78
4.4.2 Time dependent tidal sensitivity 79
4.4.3 Tidal sensitivity of RTRs vs the main front 79
4.5 Discussion 80
4.5.1 Spatial distribution of tidal sensitivity 80
4.5.2 The role of secondary events 83
4.5.3 Tidal sensitivity and LFE recurrence intervals 85
4.5.4 Phase of LFE asperity failure relative to tidal stress 87
4.5.5 Evolution of tidal sensitivity through slow slip events. 89
4.5.6 24 hour periodicity of LFE detections 89
4.6 Conclusions 90

5 Conclusions 92
5.1 Key contributions and limitations 92
5.1.1 Blind deconvolution 92
5.1.2 Comparative study of LFE templates in northern Cascadia . . . 93
5.1.3 Tidal modulation of LFEs 94
5.2 Future research directions 95
5.2.1 Multigrid strategies in deconvolution 95
5.2.2 Green's function recovery applications 95
5.2.3 High resolution detection and location of LFEs using cross-station approaches 96
5.2.4 Structural studies using LFE templates 96
5.2.5 Tidal modulation of RTRs and streaks and implication for plate boundaries 97

Bibliography 111

A Supplementary material for Chapter 3 112
B Supplementary material for Chapter 4 116

List of Tables

2.1 Inversion parameters employed in numerical experiments. 26
2.2 Schematic representation of the 3 classes of experiment. 27

4.1 RTRs documentation for 2003, 2004, 2005, 2008. 75
4.2 RTRs documentation for 2010, 2011, 2012 76

A.1 Parameters employed in hypoDD inversion 113

B.1 UDSS and FNS N_{ex} values for RTRs and non-RTR events 120

List of Figures

1.1 Map of Cascadia subduction zone 6
1.2 Picture of the subducting Juan de Fuca plate 7
1.3 2012 Tremor episode 8

2.1 Problem configuration in the context of global seismology 15
2.2 Weighting function $w(t, \tau)$ for different values of a and $\tau = 4$ 17
2.3 *P*- and *S*-component of Green's function employed in numerical experiments 25
2.4 *P*- and *S*-seismograms generated with random Gaussian source 25
2.5 *P*- and *S*-seismograms generated with band-limited source 26
2.6 Inversion using random Gaussian sources and P-components 29
2.7 Inversion using random Gaussian sources and *S*-components 30
2.8 Inversion using random Gaussian sources and *P*- and *S*-components 31
2.9 Inversion using band-limited sources and *P*-components 32
2.10 Inversion using band-limited sources and *S*-components 33
2.11 Inversion using band-limited sources and *P*- and *S*-components 34

3.1 Distribution of stations used in the study of LFE templates 38
3.2 North, east and vertical components of 3 LFE templates 41
3.3 Three-component LFE template waveforms 43
3.4 Maps of LFE locations computed using the Hyp2000 software 45
3.5 Depth profiles of seismicity in Vancouver Island and Washington state . . . 47
3.6 Example of waveform matching in moment tensor inversion 53
3.7 Map of double couple mechanisms determined from moment tensor inversion 54
3.8 Map of double couple mechanisms for NVI subarray 55
3.9 Map of double couple mechanisms for SW subarray 56
3.10 Map of double couple mechanisms for NW subarray 57

4.1 Map of LFE family locations 61
4.2 2007 tremor episode time series of tidally-induced normal and shear stresses 63
4.3 Map of tidal stress amplitudes 65
4.4 Map of N_{ex} values relative to tidal stresses and stress rates 67
4.5 N_{ex} values relative to tidal stresses and stress rates plotted against each other 68
4.6 Correlation between N_{ex} values and mean envelope amplitude 69
4.7 LFE rate plots as a function of the magnitude of the 4 tidal components . . 70
4.8 Phase histograms 72
4.9 N_{ex} UDSS histograms 73
4.10 Along-strike profile and time-distance plots for 2003 and 2012 tremor episodes 74
4.11 LFE rate plots as a function of hour of day (Pacific time) 81
4.12 Cumulative Distribution functions 86

A.1 Map of LFE locations from hypoDD inversion 113
A.2 Depth profiles A-A' to J-J' of seismicity in northern Cascadia 114
A.3 Condition number 114
A.4 Histograms of strike, dip and rake distribution 115

B.1 hypothesis test for spurious correlation 121

List of Abbrevations

CNSN	**C**anadian **N**ational **S**eismograph **N**etwork
dFNS	**F**ault **N**ormal **S**tress rate
dUDSS	**U**p **D**ip **S**hear **S**tress rate
ETS	**E**pisodic **T**remor and **S**lip
FNS	**F**ault **N**ormal **S**tress
GCV	**G**eneralized **C**ross **V**alidation
GPS	**G**lobal **P**ositionning **S**ystem
LFE	**L**ow **F**requency **E**arthquake
LVZ	**L**ow **V**elocity **Z**one
NVI	**N**orthern **V**ancouver **I**sland
NW	**N**orthern **W**ashington
PBO	**P**late **B**oundary **O**bservatory
PC	**P**rincipal **C**omponent
PCA	**P**rincipal **C**omponent **A**nalysis
PNSN	**P**acific **N**orthwest **S**eismic **N**etwork
RTR	**R**apid **T**remor **R**eversal
SNR	**S**ignal to **N**oise **R**atio
SSE	**S**low **S**lip **E**vent
SVI	**S**outhern **V**ancouver **I**sland
SW	**S**outhern **W**ashington
TA	**T**ransportable US**A**rray
UDSS	**U**p **D**ip **S**hear **S**tress

List of Symbols

Chapter 1

$c(t)$	cross-correlation function
$\mathcal{F}\{\delta(t)\}$	filtered Dirac delta function
$g(t)$	Green's function
$\hat{g}(t)$	Green's function estimate
$s_i(t)$	i^{th} source signature time series
$u_i(t)$	i^{th} seismogram time series
V_P	elastic P-wave velocity
V_S	elastic S-wave velocity
$\delta(t)$	Dirac delta function
$\hat{\Phi}^g(t)$	estimate of the true autocorrelation of the Green's function $g(t)$
$\star$	convolution product
$\otimes$	cross-correlation product

Chapter 2

a	steepness parameter
$\mathbf{A}$	matrix comprising a combination of $\mathbf{U}_i$, $\mathbf{U}_j$ and zero blocks
$\mathbf{B}$	matrix containing the derivatives $\frac{\partial w_i(t,\boldsymbol{\tau})}{\partial \tau_i}$
$\mathbf{e}$	scaling constraint
$g(t)$	Green's function
$H(t)$	Heaviside function
$\mathbf{H}$	Hessian matrix
L	Lagrange function
p	slowness
$s_i(t)$	i^{th} source signature time serie
$u_i(t)$	i^{th} seismogram time serie
$\mathbf{U}_i$	Toeplitz matrice containing the seismogram $u_i(t)$

V_P	elastic P-wave velocity
V_S	elastic S-wave velocity
$w_i(t, \boldsymbol{\tau})$	windowing function
$\mathbf{W}$	diagonal weighting matrix containing $w_i(t, \boldsymbol{\tau})$
$\mathbf{x}$	source function vector
$\mathbf{y}$	"pre-weighted" source function vector
$\mathbf{Y}$	diagonal matrix containing $\mathbf{y}$
α	constant
β	Tikhonov parameter
$\delta(t)$	Dirac delta function
λ	Lagrange multiplier
∇L	gradient of Langrange function
ρ	density
$\boldsymbol{\Sigma}$	covariance matrix
$\boldsymbol{\tau}$	duration
$\boldsymbol{\tau}_0$	initial duration
$\star$	convolution product

Chapter 3

$g(t)$	Green's function
$\hat{g}(t)$	Green's function estimate
$s_i(t)$	i^{th} source signature time series
$u_i(t)$	i^{th} seismogram time series
$\hat{\Phi}^g(t)$	estimate of the true autocorrelation of the Green's function $g(t)$
$\otimes$	cross-correlation product

Chapter 4

a	friction coefficient
D	total amount of slip accumulated over a tremor episode

D_c	characteristic length scale
e_{rr},$e_{\theta\theta}$,$e_{\lambda\lambda}$	vertical and horizontal strains
L_m	length of main slip front
L_{patch}	LFE patch dimension
L_s	along-dip distance
N_{ex}	degree of correlation of LFE occurrence with tidal stress
R	sample correlation coefficient
T	tidal period
T_θ	period that defines time scale for the evolution of state variable
V	creep rate of the fault surrounding an LFE patch
V_L	long-term displacement averaged creep rate
V_{ss}	steady state velocity during SSE
ΔV	velocity perturbation
V_P	elastic P-wave velocity
V_S	elastic S-wave velocity
$\Delta\tau_{sd}$	stress drop
$\Delta\tau_{ss}$	tidal shear stress amplitude
μ	shear modulus
ν	Poisson's ratio
σ_e	effective normal stress
τ	shear resistance
τ_0	shear resistance at creep rate V_L
θ	phase advance wrt peak UDSS

Chapter 5

V_P	elastic P-wave velocity
V_S	elastic S-wave velocity
$\mathbf{y}$	"pre-weighted" source function
$\boldsymbol{\Delta\tau}$	positive change of source duration with iterations

Acknowledgements

First and foremost, I would like to express my profound gratitude and utmost respect to my research advisor Michael Bostock. I benefited from his exemplary guidance, monitoring and constant encouragements throughout the course of this thesis. I will not forget the opportunities Michael gave me to travel and share my work with the "big shots" of seismology.

I would like to thank the co-authors of my publications Eldad Haber and Amanda Thomas. I am very grateful for their contributions to the development of my research. Their participation, discussions and our meetings have been of greatest benefit.

My gratitude also goes to the members of my PhD committee, Eldad Haber, Catherine Johnson and Andrew Calvert from Simon Fraser University, for discussion and guidance during committee meetings.

I gratefully acknowledge the helpful comments of Nick Beeler, Roland Burgmann, Jessica Hawthorne, Allan Rubin and David Shelly on chapter 4.

I would also like to show my appreciation to the feedback of Professor Simon Peacock on the development of my findings and extend my thanks to the computer technicians of the EOAS department for their help in running my code.

I thank my colleagues Ben Postlethwaite, Gian Matharu, Geneviève Savard and Brendan Smithyman for their participation in many ways.

The completion of this Ph.D is the culmination of 10 years of university studies in France and Canada. I will always remember my professors Alexandre Fournier, Andrea Walsperdorf, Etienne Jaillard, Jean-Robert Grasso and Helle Pedersen from the Université Joseph Fourier for their encouragements and support to reach this level of understanding.

I would like to give my loving thanks to my family and particularly to my aunt and uncle Annick and Pierre Spierer and to my grandparents Jacques and Jacqueline Royer, for their support and love. I am very grateful for their encouragements to find my own path far from them and honored to join the exclusive Ph.D club in our family! Thank you to my family of heart, Babeth, Roland, Coraline, Clément, Fabien, Lisa, Marilou, Alice, Nathalie and Mustapha. They have been there for me and with me every day and I am very grateful for having them in my life.

Lastly, I thank Ralf Hansen. His support in the good moments, but also in the more difficult ones, has been a precious help. His presence became essential, particularly this past year, for the final climb to the summit. Thank you.

Je dédie cette thèse à mon défunt père Pierre Royer. En gravant les plus hauts sommets enneigés, tu m'as inculqué le goût de l'effort et de l'ambition. Tu m'as rendu curieuse des forces de la nature et aujourd'hui, je ne serais pas là sans toi.
Je dédie cette thèse à ma défunte mère Martine Royer. Comme une étoile dans le ciel, tu me guides et me soutiens. Tu m'as appris à combattre l'adversité, à croire en moi et à réaliser mes rêves. Aujourd'hui, je ne serais pas là sans toi.
Merci à tous les deux. Merci pour tout.

"You can't stop the waves,
but you can learn to surf"
Joseph Goldstein

Chapter 1

Introduction

1.1 Research objectives

I present in this thesis three different research topics that can be read independently of each other. However, it is possible to relate them through the general concept of deconvolution to estimate a Green's function. The first topic relates to the blind deconvolution of seismograms regularized via minimum support. Through an algebraic analysis, I have built a mathematical model to recover the earthquake source signature in terms of amplitude and source duration from recorded seismograms. The second topic exploits a semi-empirical deconvolution approach involving iterative correlation–detection–stacking to generate low frequency earthquake (LFE) templates from tremors recorded in northern Vancouver Island and Washington state, thereby extending a previous LFE catalogue for southern Vancouver Island [*Bostock et al.*, 2012] through much of northern Cascadia. I provide empirical and semi-analytical arguments justifying the identification of LFE templates with "Green's function" sections corresponding to moment tensor point sources. I proceed to compare the distribution and excitation of LFE sources across northern Cascadia as revealed by LFE templates and discuss implications for plate boundary structure and LFE genesis. The third topic of this thesis relates to the influence of the solid Earth and ocean tides on a catalog of LFEs as derived from LFE templates for southern Vancouver Island and Washington state. The spatial and temporal sensitivity of LFEs provides insight into the source

region (i.e plate boundary) properties such as friction and pore fluid pressure, but also on the mechanism of displacement and conditions of triggering.

1.2 Overview of deconvolution approaches

In seismology, the Green's function describes the impulse response of the Earth through which seismic waves travel. It describes the effects of reflections and refractions of seismic waves at interfaces between rocks of different properties, the phase delays/advances and geometrical spreading due to lateral changes in velocity structure, and the influence of attenuation due to anelasticity. Knowledge of the Green's function can aid significantly in imaging the internal structure of the Earth. Deconvolution of seismic data is an important component of signal processing that aims to remove the seismic source from seismograms, thereby isolating the Green's function.

The two deconvolution approaches I employ in this thesis start from the same mathematical description in which a seismic record $u(t)$ is defined as the convolution of a seismic source $s(t)$ with a Green's' function $g(t)$, expressed in the time domain as:

$$u(t) = s(t) \star g(t), \tag{1.1}$$

where $\star$ denotes the convolution product. Blind deconvolution, the main topic of chapter 2, refers to the isolation of either $s(t)$ or $g(t)$ without prior knowledge of the other. In this approach, I consider seismograms of multiple earthquakes from similar locations recorded at a given station and that therefore share the same Green's function. We can write a linear relation in the time domain:

$$\begin{aligned} & u_j(t) \star s_i(t) - u_i(t) \star s_j(t) \\ & = g(t) \star s_i(t) \star s_j(t) - g(t) \star s_j(t) \star s_i(t) \\ & = 0, \end{aligned} \tag{1.2}$$

where $u_i(t)$ is the seismogram for the ith source and $s_j(t)$ is the jth unknown source. From two or more seismograms, we obtain a system where the unknowns are the sources. Our approach is to identify the Green's function as the common convolutional element within a set of seismograms, but the approach might equally well apply to a common

source, as implied by the symmetry of $s(t)$ and $g(t)$ in 1.1. Although the topic of blind deconvolution has been addressed by many authors, the originality of this first approach is that it requires only multiple seismograms recording the same sources (or receivers), and regularization by minimum support. However, the nonlinearity of this analysis renders the system expensive to solve and sensitive to noise, and therefore it can be applied to only short duration seismograms with high SNR.

Non-volcanic or tectonic tremors are weak signals with low SNR originating from major convergent or transform plate boundaries. It has been shown that this tremor comprises swarms of many small, repeating earthquakes known as LFEs [*Shelly et al.*, 2007]. Since the SNR levels are low we must rely on a different deconvolution approach that exploits the multiplicity of repeating sources. The second blind deconvolution approach described in this thesis employs an iterative strategy that involves correlation, threshold detection and stacking to isolate the Green's function. It correlates a small windowed section of a Green's function estimate (e.g. a single LFE) at a number of channels with the corresponding tremor time series. Times for which the summed correlation coefficient exceeds a specified threshold are considered further detections of LFEs representing the same Green's function. An individual tremor episode typically lasting 2-3 weeks may contain more than 1000 LFE detections emanating from the same location. These detections can be aligned and stacked to produce a high SNR template. The template can be used as an updated Green's function estimate and the same process is then iterated until there is no further improvement in SNR. The interpretation of the template as an empirical Green's function can be justified as follows. Consider the cross correlation $c(t)$ of a Green's function estimate $\hat{g}(t)$ with a seismogram $u(t)$. We can write, using 1.1:

$$c(t) = \hat{g}(t) \otimes u(t) = \hat{g}(t) \otimes g(t) \star s(t) = \hat{\Phi}^g(t) \star s(t), \tag{1.3}$$

where $\otimes$ denotes cross-correlation. $\hat{\Phi}^g(t)$ is an estimate of the true autocorrelation of $g(t)$ and so will peak near lag t=0. The timing of the maximum of $c(t)$ will then occur at or near the time $t = t^{max}$ at which $s(t)$ possesses its maximum. Times for which $c(t)$ exceeds a certain threshold are considered as detections and the stack of corresponding

seismograms $u_i(t)$, each shifted by the corresponding detection time t_i^{max}, can be written as:

$$\sum_i u_i(t - t_i^{max}) = g(t) \star \sum_i s_i(t - t_i^{max}). \tag{1.4}$$

As the number N of detections increases, the sum of shifted band-limited source functions $s_i(t - t^{max})$ will tend toward a scaled, filtered delta function (since LFEs and tremor are inherently band limited to 1-10Hz),

$$\lim_{N\to\infty} \sum_i^N s_i(t - t_i^{max}) \to \mathcal{F}\{\delta(t)\}, \tag{1.5}$$

and a scaled, band-limited version of $g(t)$ can be approximated by summing the shifted $u_i(t)$. The detection of LFEs that repeat 1000's of times from the same location over periods of a few years allow us to assemble fully 3-D empirical Green's functions, in contrast with previous studies (stacking of phase-normalized long-period body waves [*Shearer*, 1991] and broadband teleseismic $P-$waves [*Kumar et al.*, 2010]) for which the relative infrequency of regular seismicity limits Green's function retrieval to 1-D estimates.

1.3 Tectonic context of the northern Cascadia subduction zone

1.3.1 Overview

The Cascadia subduction zone is located along the western coast of North America, where the oceanic Juan de Fuca, Explorer and Gorda plates are being subducted beneath the continental North American plate. It stretches over 1000 km from northern Vancouver Island to northern California. For the purpose of this thesis, we will focus on the northern part of Cascadia from northern Vancouver Island to southern Washington state (Figure 1.1). The Juan de Fuca plate subducts at a rate of ∼40 mm/year beneath the North American plate and, due to its relatively young age (≤ 11Myr), it is associated with warmer temperatures than most other subduction zones.

The analysis of seismic waves affords several different means for studying the internal structure of the subduction zone and the geological processes that are actively reshaping it. Deep slab structure (> 100 km depth) has been primarily imaged using teleseismic P-wave traveltime tomography. Below Washington and western British Columbia, the slab is characterized by a quasi-planar, high P-velocity slab evident to at least 400 km depth [*Audet et al.*, 2008]. The slab dip varies from about 50° to 60° to 45° below southern Vancouver island, northern Washington and southern Washington, respectively [*Bostock and Vandecar*, 1995, *Burdick et al.*, 2008, *Chu et al.*, 2012, *Mercier et al.*, 2009, *Michaelson and Weaver*, 1986, *Obrebski et al.*, 2011, *Rasmussen and Humphreys*, 1988]. It dips to the northeast below Vancouver Island and to the east below Washington state. Slab structure at shallower levels (<100 km depth) beneath southern British Columbia and Washington state has been investigated using seismic reflection and receiver functions analysis, that reveal a landward-dipping, low-velocity zone (LVZ), first observed by *Langston* [1977, 1981] and interpreted as the subducting oceanic crust. It coincides with a reflective and conductive layer originally identified in seismic reflection studies [*Clowes et al.*, 1987, 1990, *Green et al.*, 1986] and later in magnetotelluric surveys [*Kurtz et al.*, 1990, *Soyer and Unsworth*, 2006], known as the "E"-layer on the southern Vancouver Island LITHOPROBE transect. The LVZ has been most recently interpreted to be upper oceanic crust [*Bostock*, 2013, *Hansen et al.*, 2012]. A schematic cartoon illustrating important tectonic elements of the Cascadia subduction zone is provided in Figure 1.2.

In this study I will use 2 different models for the Juan de Fuca subducting plate, one constructed by *Audet et al.* [2010] and the other by *McCrory et al.* [2012], to analyse LFE signals. *Audet et al.* [2010] identified the plate boundary with the top of the LVZ using scattered teleseismic P arrivals and by assuming fixed P-velocity of the overriding plate with locally variable V_P/V_S ratio. In contrast, *McCrory et al.* [2012] used intraplate earthquake locations and regional seismic velocity profiles to synthesize information of the depth structure. The authors identified the top of the Juan de Fuca slab near the upper surface of intraplate seismicity and weighted these seismicity constraints more highly than structural information derived from velocity profiles in areas where both sources of information were available. The two slab models are plotted in

Figure 1.1.

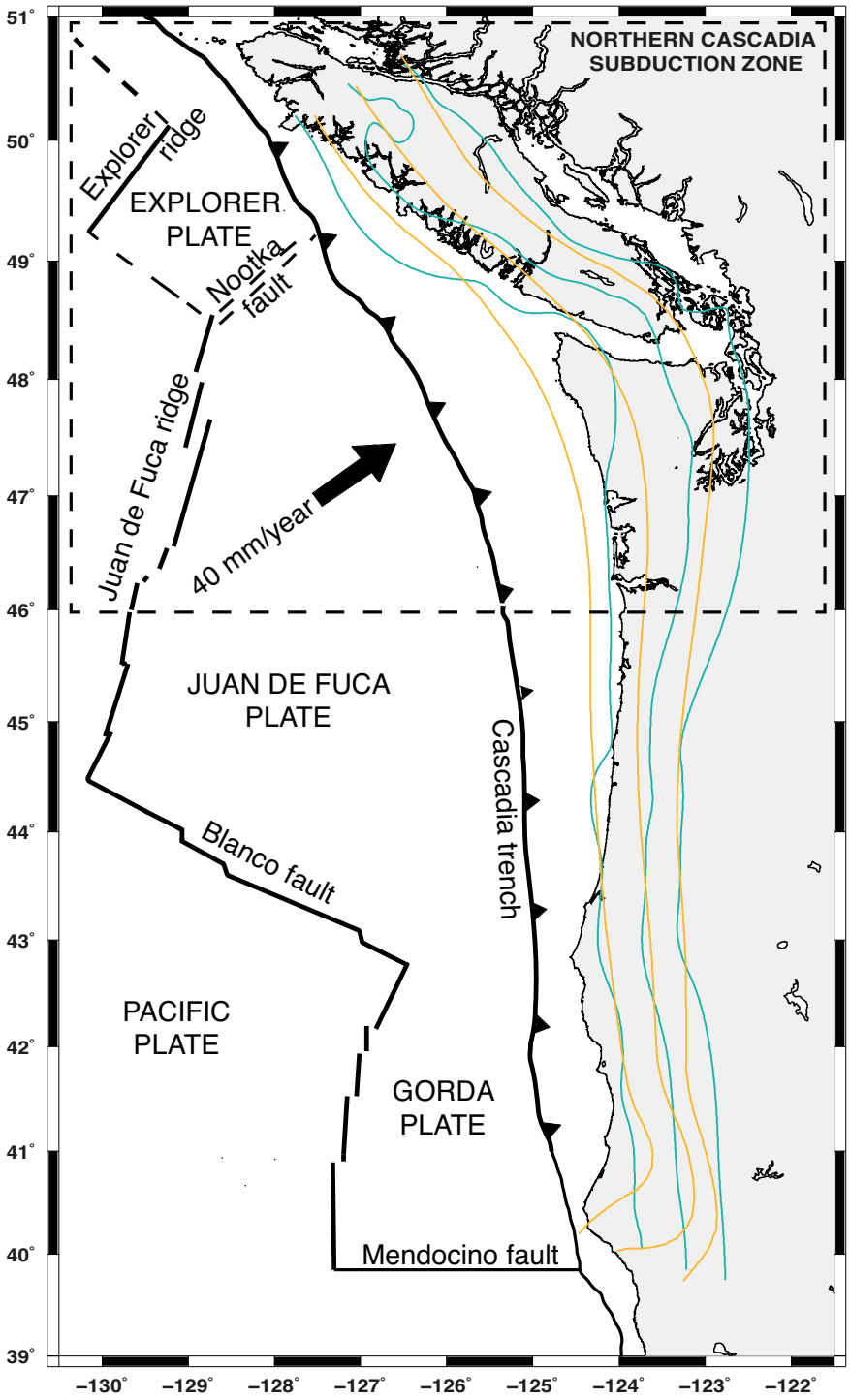

FIGURE 1.1: Map of Cascadia subduction zone. Northern Cascadia subduction zone is delimited by a dashed square. Cyan and orange lines indicate the 20, 30 and 40 km depth contours to the top of the subducting Juan de Fuca plate modeled by *Audet et al.* [2010] and *McCrory et al.* [2012], respectively.

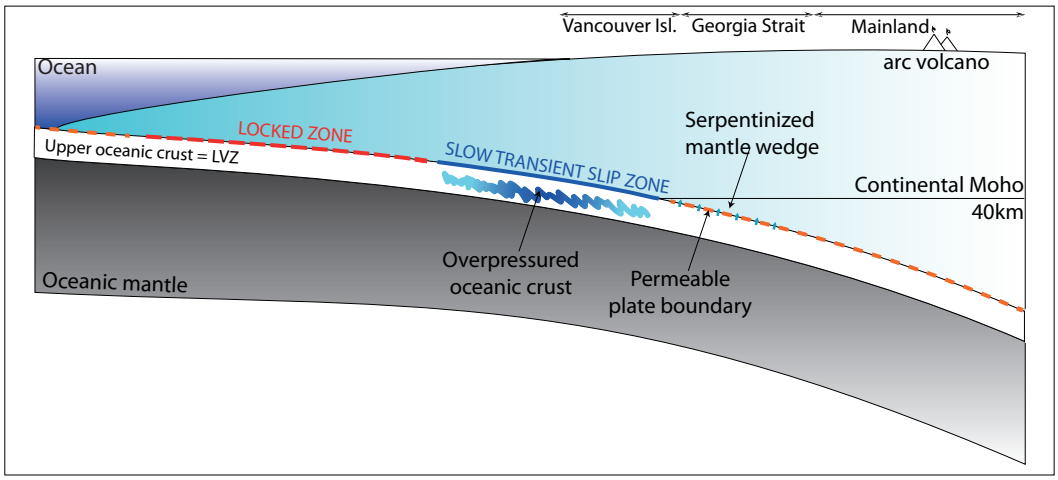

FIGURE 1.2: Schematic cartoon of subducting plate in northern Cascadia, modified from *Audet et al.* [2009]

1.3.2 Tremor, slow slip and low frequency earthquakes

The Juan de Fuca plate does not subduct continuously. At shallow depths (< 25 km depth), thermal and deformation studies [*Dragert et al.*, 1994, *Wang et al.*, 1994] indicate a locked zone approximately 60 km wide in which strain energy is accumulated without rupture over a period of few hundred years (Figure 1.2). Using Global Positioning System (GPS) monitoring, slow slip events equivalent to a M ∼6-7 magnitude earthquake have been detected farther downdip (depths of 25-40 km, referred as "slow transient slip zone" in Figure 1.2) beneath Vancouver Island and Washington state. These slow slip events occur over a period of a few weeks [*Dragert et al.*, 2001] and repeat at intervals of 13 to 16 months [*Miller et al.*, 2002]. First thought to be seismically silent, the slip is accompanied by pulsating, tremorlike seismic signals [*Rogers and Dragert*, 2003], that is, the tremor signals described in section 1.2. These tectonic tremors are weak, semi-continuous and characterized by a frequency spectrum that is peaked between 1 and 10 Hz. Figure 1.3 show the 2012 tremor episode locations in northern Cascadia. Tremor locations in Cascadia can been viewed on an interactive webpage (*http* : *//tunk.ess.washington.edu/map_display*), built by Aaron Wech [*Wech and Creager*, 2008].

Improvements in seismic monitoring networks and in signal processing techniques led to the discovery that LFEs form part of tectonic tremor [*Shelly et al.*, 2007]. Despite their low magnitudes and limited bandwidth, these signals can be detected at low

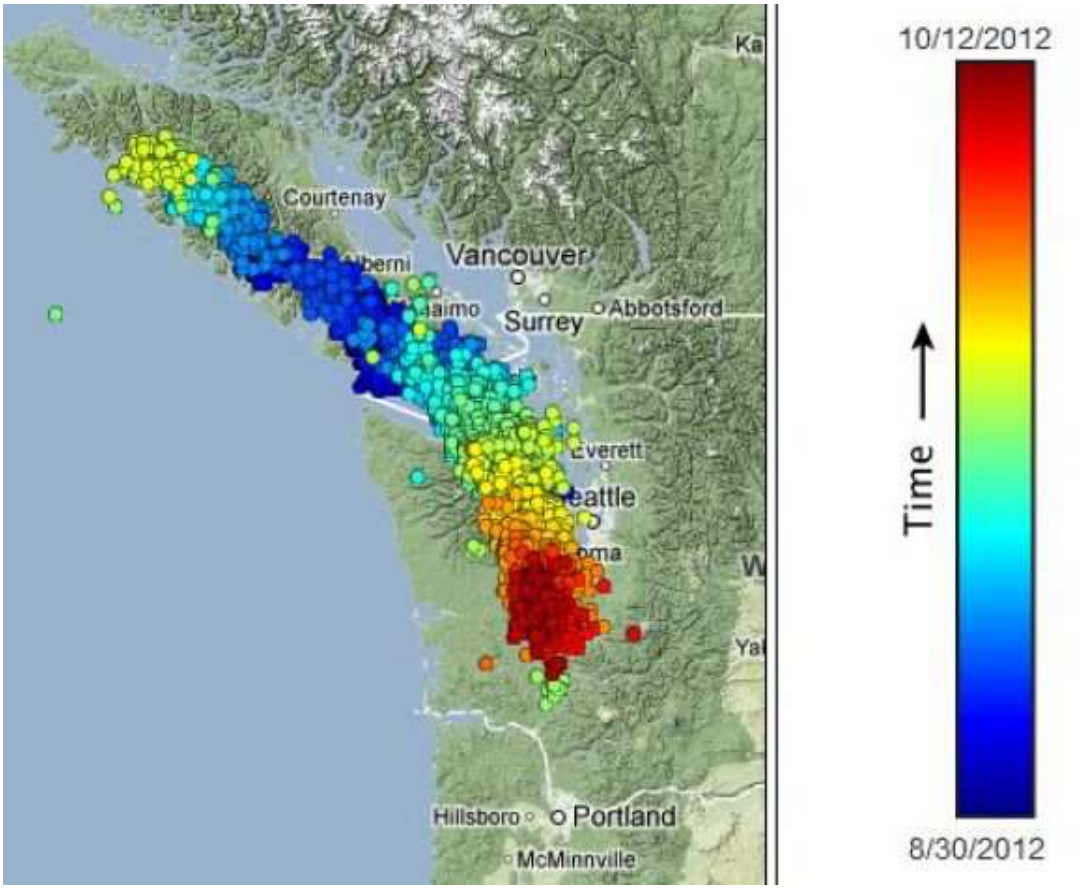

FIGURE 1.3: 2012 episodic tremor and slip event (picture from Wech's interactive webpage displaying automatic tremor locations, referred in text).

SNR thresholds and with high temporal precision using powerful network correlation techniques [*Brown et al.*, 2008, *Gibbons and Ringdal*, 2006, *Shelly et al.*, 2006] as summarized in section 1.2 and further developed in chapter 3.

The fact that LFE templates can be considered as empirical Green's functions is useful in the identification of arrivals for location and for waveform matching as required in moment tensor inversion. Previous spatio-temporal studies of LFEs in Shikoku and Cascadia suggest that tremor and LFEs are the result of slow slip at the plate interface [*Bostock et al.*, 2012, *Shelly et al.*, 2007, *Wech and Creager*, 2007] and the combination of tremor and slow slip is often referred to as Episodic Tremor and Slip (ETS). A comparative study of LFEs across northern Cascadia is developed in chapter 3 of this thesis.

1.3.3 Earth tides and low frequency earthquakes

The combined action of the Sun and the Moon on the Earth produces periodic tidal stress variations of the order of 4 kPa in the Earth's crust to depths of 10's of km. The amplitudes of the tidal stress variations are up to three orders of magnitude smaller than the stress drop produced by earthquakes. However, tidal stress rate is generally higher than the tectonic stress accumulation on a fault. Therefore, tidal stresses could trigger earthquakes on a weak fault close to the critical rupture level. The correlation between tides and earthquake occurrence has been investigated for the past century and it has transpired that most studies have not been able to highlight a correlation between earthquakes and tides [*Knopoff*, 1964, *Rydelek et al.*, 1992, *Schuster*, 1897, *Shudde and Barr*, 1977, *Simpson*, 1967, *Vidale et al.*, 1998]. However, more recent studies on large numbers of earthquakes with input from laboratory experiments [*Beeler and Lockner*, 2003] show the existence of a weak correlation between the two phenomena [*Cadicheanu et al.*, 2007, *Enescu and Enescu*, 1999, *Stavinschi and Souchay*, 2003, *Tanaka et al.*, 2002, 2006].

In regions where tectonic tremor and LFEs occur, the presence of high pore fluid pressure as revealed by teleseismic receiver function and regional tomographic studies [*Audet et al.*, 2009, *Hansen et al.*, 2012, *Shelly et al.*, 2006], suggests that fluids may play an important role in allowing slow slip to occur by reducing the effective normal stress to near zero. The peculiar physical conditions represented within the transition from plate locking to continuous creep have prompted new investigations into the sensitivity of ETS to the tides. It has become increasingly evident in recent years that slow slip, tectonic tremor and LFEs are sensitive to stresses from tidal forces during periods of ETS [*Hawthorne and Rubin*, 2010, 2013, *Klaus*, 2012, *Lambert et al.*, 2009, *Nakata et al.*, 2008, *Rubinstein et al.*, 2008, *Shelly et al.*, 2007, *Thomas et al.*, 2012, 2013]. Tremors analysis in northern Cascadia shows a clear pulsing of activity with a period of 12.4h, corresponding to the M2 tide [*Rubinstein et al.*, 2008], with a peak at times of maximum tidal shear stress [*Lambert et al.*, 2009]. Simulations from laboratory experiments [*Hawthorne and Rubin*, 2010, 2013] are able to reproduce a quasi-sinusoidal tidal modulation of the slip rate, with a maximum moment rate close to the maximum applied tidal stress. The phase between peak LFE excitation and peak tidal stress is an

important factor as it may reflect how the background loading rate influences the timing of LFEs in response to the tidal load. *Beeler et al.* [2013] proposed a model for which LFE sources are small seismic patches that fail at a threshold stress on a otherwise creeping fault. From this model, LFE rate can be explained by adding stressing rate contributions from the plate motion, the background creep and the tides directly acting on the LFE patches. In chapter 4 of this thesis I analyze the influence of tidal stresses on LFE catalogues in southern Vancouver Island and Washington state. The 1000's of detections that constitute an LFE template and their locations allow a high-resolution analysis of the spatial and temporal sensitivity of LFEs to tidally induced up-dip shear stress (UDSS), fault normal stress and their derivatives. We use our observations and the *Beeler et al.* [2013] model to constrain fault rheology, such as the effective normal stress on the LFE patches and their dimension, and the characteristic slip for friction to evolves between two steady state.

1.3.4 Rapid tremor reversals

Observed during ETS, Rapid tremor reversals (RTRs) are linear streaks of tremor migration (or LFE detections) moving at high apparent velocities in the "opposite" direction to the main front [*Houston et al.*, 2011]. *Thomas et al.* [2013] note that RTRs in northern Washington occur almost exclusively during times of positive UDSS. Consequently, RTRs may play an important role in slip processes and their characterization may lead to improvements in our overall understanding. In chapter 4 of this thesis, I identify RTRs in southern Vancouver Island and examine their sensitivity to UDSS.

Chapter 2

Blind deconvolution of seismograms regularized via minimum support

2.1 Introduction

The blind deconvolution problem has a long history in seismology owing to the importance of separating effects of the source (or "wavelet") from details of wave propagation (the Earth's "Green's function", "impulse response" or "reflectivity") in studies of earthquake rupture, earth structure and hydrocarbon exploration. A range of approaches has been considered that includes i) homomorphic deconvolution, ii) higher-order statistics (cumulants), iii) representation theorems and iv) multichannel blind deconvolution.

Homomorphic deconvolution is a non-linear deconvolution technique that satisfies a generalized principle of superposition. *Ulrych* [1971] and *Tribolet* [1978] applied this technique to the analysis of seismic wavelets by considering the complex cepstrum of a seismogram, defined as the complex logarithm of its z-transform. The structure of the complex cepstrum is such that it contains the additive contribution of the seismic wavelet and of the impulse response. These contributions may in some instances be separated by windowing the cepstrum. A narrow window around the quefrency origin, for example, tends to retain the contribution from the source pulse. Using this

approach, these authors were able to produce reasonable source estimates but others such as Buttkus (*Buttkus* [1975]) have noted that the success of wavelet estimation by low-quefrency windowing is largely dependent on the signal-to-noise ratio of the input data, the degree of overlapping of the wavelet cepstrum and impulse response cepstrum, and the choice of the window function.

In cumulant methods, as proposed by *Sacchi and Ulrych* [2000], higher-order cumulants of seismic signals are employed in conjunction with spectral factorization to recover seismic wavelets. Higher-order cumulants are obtained by multiplying the n^{th} order moment of the seismic wavelet by the central lag of the n^{th} order cumulant of the reflectivity. Spectral factorization of higher-order cumulants enables estimation of the wavelet through the recovery of its minimum-phase and non-minimum-phase components. This procedure requires the assumption of a non-Gaussian, white reflectivity. Moreover, the authors note that the estimation of higher-order cumulants from data is not simple. The procedure is computationally intensive and requires long records that are not always available when working with real data.

Weglein and Secrest [1990] proposed a wave-theoretical source estimation method based on the Lippmann-Schwinger equation and Green's theorem for seismic reflection geometries. These two equations lead to a relationship between the Fourier transform of the source and the Green's function that characterizes the propagation within the medium. Results show that this multi-dimensional, deterministic technique allows one to estimate either an acoustic or an elastic earth wavelet, without any assumptions concerning Earth structure. However, it does require that both the field and its normal derivative be measured at the surface.

In multichannel blind deconvolution, one exploits the redundancy of multiple seismograms sharing a common convolutional element in either sources or Green's functions, and the problem can be reduced to finding the greatest common divisor of two polynomials (e.g., *Gogonenkov* [1990]). *Rietsch* [1997a,b] exploited this relation in implementing an algorithm that allows one to estimate the source wavelet shared by several seismic traces. A matrix is constructed from the autocorrelations and cross correlations of the traces. The number of zero eigenvalues of this matrix is equal to the number of samples of the wavelet and the eigenvectors associated with these eigenvalues

are related to the reflection coefficients. Numerical experiments show that the method works well for data that have reasonably met all assumptions (the data share the same wavelet, incorporate different reflectivities, and are not contaminated by noise). In the presence of noise, however, the performance of this algorithm deteriorates and is difficult to assess.

Another method proposed by *Mazzucchelli and Spagnolini* [2001] extracts the Green's function by solving an overdetermined linear system in the least squares sense within the frequency domain. The results demonstrate that multichannel deconvolution can correctly recover the Green's function when starting from noisy traces convolved with a mixed-phase wavelet, without any assumptions on the source's signature and on the whiteness properties of the Green's function. However, the authors remain unclear regarding the implementation of a scaling constraint and indicate that the estimation of the source signature remains difficult when processing large datasets.

Here we reexamine the multichannel approach in exploiting the commonality of a convolutional element within a set of seismograms. Our examples identify the Green's function as this element, but our approach might equally apply to a common source. The extraction of the complementary element (the source in our case) will be accomplished by solving a system of equations comprising differences of convolutions between data and unknowns sources with regularization through minimum support.

2.2 Problem formulation

We will cast the blind deconvolution problem in the context of teleseismic body-wave, receiver-side scattering as depicted in Figure 2.1, commonly referred to as receiver function analysis [*Bostock*, 2007, *Langston*, 1977, *Vinnik*, 1977]. We consider separate recordings (or "seismograms") $u_i(t)$ of multiple earthquake sources in close proximity, made at a single, distant receiver. Each earthquake is characterized by a distinct source signature $s_i(t)$ but the propagation path is the same, so that the seismograms share a common convolutional element in the Green's function $g(t)$, that is,

$$u_i(t) = s_i(t) \star g(t), \tag{2.1}$$

where $\star$ denotes convolution, and index i enumerates the source. In actual fact, earthquake recordings are typically made in 3 orthogonal components of particle velocity. However, for simplicity we shall, for the time beginning, consider $u_i(t)$ to represent only one component.

This component could be one of the vectorial components, e.g. the horizontal component in the vertical plane that includes both source and receiver, also known as the "radial" component, or it might represent a linear combination of vectorial components designed to isolate energy within a single scattering mode (i.e. *P* or *S*, [*Bostock*, 2007]).

By considering seismograms from any pair of earthquakes $s_i(t)$, $s_j(t)$, we may write the following expression:

$$u_i(t) \star s_j(t) - u_j(t) \star s_i(t) = 0. \tag{2.2}$$

We further assume that $s_i(t)$ should be independent of $s_j(t)$; that is, their z-tranforms should not share zeros, or equivalently, the convolutional elements common to $u_i(t)$ and $u_j(t)$ should reside only within $g(t)$. This expression can be recast as a homogeneous matrix system:

$$\mathbf{A} \quad \mathbf{x} \quad = \quad \mathbf{0}. \tag{2.3}$$

In the case of 2 sources, the system can be written in block form as:

$$\left[\begin{array}{c:c} \mathbf{U}_2 & -\mathbf{U}_1 \end{array}\right] \left[\begin{array}{c} \mathbf{s}_1 \\ \hdashline \mathbf{s}_2 \end{array}\right] = \mathbf{0}, \tag{2.4}$$

where $\mathbf{U}_1$ and $\mathbf{U}_2$ are Toeplitz matrices containing the seismograms $u_1(t)$ and $u_2(t)$. If more than 2 sources are included within the system, that matrix $\mathbf{A}$ will comprise a combination of blocks $\mathbf{U}_i$, $\mathbf{U}_j$ and zero blocks. By imposing a scaling constraint, for example, by setting the first sample of the first source equal to 1, as $s_1(1) = 1$, the system Equation 2.3 becomes:

$$\begin{cases} \mathbf{A}\mathbf{x} = \mathbf{0} \\ \mathbf{e}^T\mathbf{x} = 1 \end{cases} \tag{2.5}$$

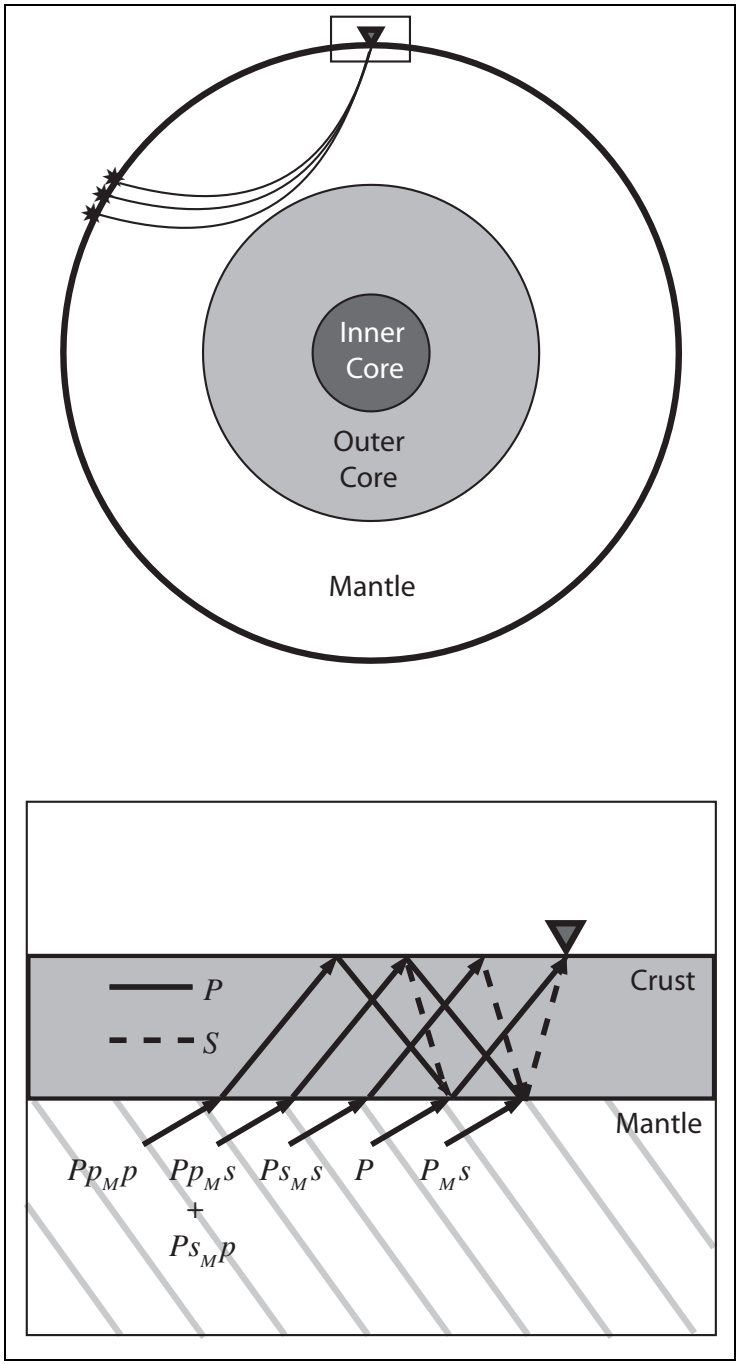

FIGURE 2.1: Problem configuration in the context of global seismology. Top panel shows three earthquakes (stars) in close proximity (location separation exaggerated) characterized by source functions $\mathbf{s}_1$, $\mathbf{s}_2$, $\mathbf{s}_3$. P-waves generated by these sources travel effectively the same propagation path through the Earth's mantle to a receiver on the Earth's surface. At the receiver side (inset, bottom panel), the incident P-wave (quasi planar wavefronts within the mantle indicated in light gray) interact with material property contrasts, e.g. the boundary between crust and mantle or "Moho", through the generation of a suite of scattered phases some of which are initially reflected at the Earth's free surface and some of which involve mode conversion from P (solid ray paths) to S (dashed ray paths).

with $\mathbf{e}^T = [1 \quad 0 \cdots 0 \quad 0]$. The linear system will, in general, be underdetermined and there are therefore infinitely many solutions. To solve this system, we need to impose meaningful information about the sources and, in particular, their durations (i.e number of points in the time series) which are not known *a priori*.

2.3 Methodology

2.3.1 Source duration

If the earthquake source durations $s_j(t)$ are specified as too short, i.e too few points, we have an overdetermined, inconsistent system. For example, at one extreme if we set the source durations equal to 1, i.e $s_1(t) = \delta(t)$ and $s_2(t) = \alpha\delta(t)$, then $u_2(t) = \alpha u_1(t)$ which cannot generally be true since $u_1(t)$ and $u_2(t)$ are required to be independent and so not equal to scaled versions of one another. If the source durations are specified as too long, we have an underdetermined, inconsistent system. For example, if we set the durations equal to the durations of the corresponding seismograms, one solution is $s_1(t) = u_1(t)$ and $s_2(t) = u_2(t)$, since $u_2(t) \star u_1(t) - u_1(t) \star u_2(t) = 0$. Moreover any function $f(t)$ convolved with both $u_1(t)$ and $u_2(t)$ will produce time series that also satisfy the system. Consequently we will select as our target the shortest solution which satisfies the system Equation 2.5. The solution is thereby regularized as "minimum support" and we assume that all the sources are "minimum support".

2.3.2 Introduction of source durations as unknowns

We choose to introduce the source durations as unknowns to be solved for as part of our solution since we do not know the length of the sources *a priori*. Consequently, it will prove useful to construct a diagonal weighting matrix $\mathbf{W}(\boldsymbol{\tau})$ which has for each source i the windowing function $w_i(t, \tau_i)$ defined as follows:

$$w_i(t,\tau_i) = \begin{cases} 1 & \text{for } t \le \tau_i \\ 1 - \frac{t-\tau_i}{a} - \frac{1}{2\pi a}\cos\frac{2\pi(t-\tau_i)}{a} & \text{for } \tau_i < t \le \tau_i + a \\ 0 & \text{for } t > \tau_i + a \end{cases} \tag{2.6}$$

The integer a controls the steepness of the cutoff such that $w_i(t, \tau_i)$ tends toward the Heaviside function $H(t-\tau)$ as a goes to zero. Note also that this function is continuous with continuous 1^{st} and 2^{nd} derivatives. Figure 2.2 shows an example of the discretized weighting function $w(t, \tau)$ for different values of a and $\tau = 4$.

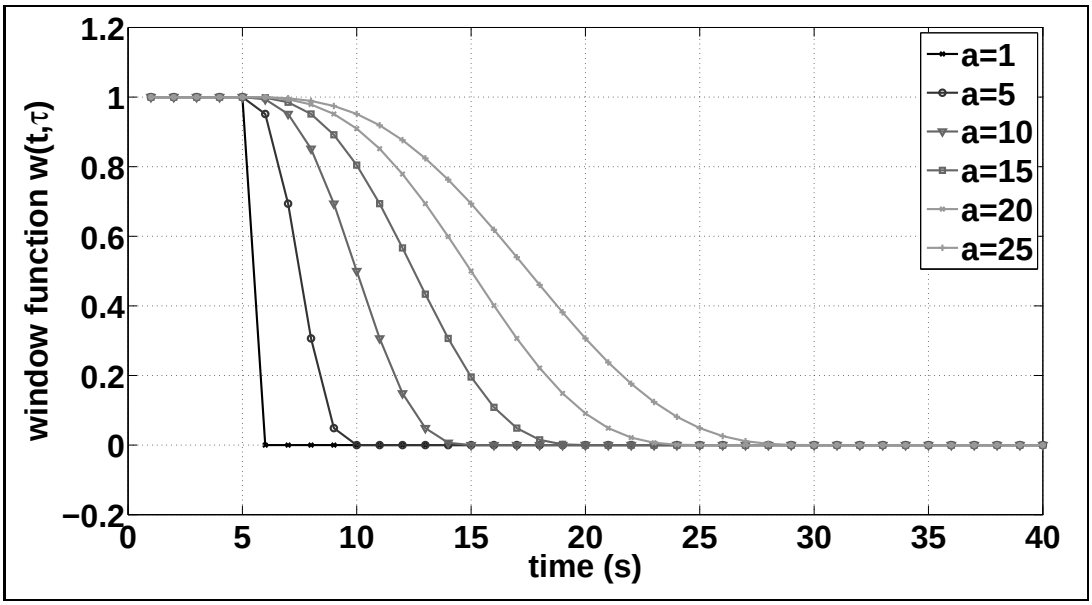

FIGURE 2.2: Weighting function $w(t, \tau)$ for different values of a and $\tau = 4$.

The matrix $\mathbf{W}(\boldsymbol{\tau})$, for e.g. 2 sources, can thus be written as:

$$\mathbf{W}(\boldsymbol{\tau}) = \mathsf{diag}\left[w_1(t, \tau_1), w_2(t, \tau_2)\right]. \tag{2.7}$$

The weighting matrix allows us to define a new vector $\mathbf{y}$ where $\mathbf{x} = \mathbf{W}(\boldsymbol{\tau})\mathbf{y}$, such that the matrix system in Equation 2.5 is recast as:

$$\begin{cases} \mathbf{A}\mathbf{W}(\boldsymbol{\tau})\mathbf{y} \approx \mathbf{0} \\ \mathbf{e}^T\mathbf{W}(\boldsymbol{\tau})\mathbf{y} = 1 \end{cases}. \tag{2.8}$$

Here we purposely choose $\mathbf{x}$ and $\mathbf{y}$ to have dimensions that are considerably longer than the anticipated source durations (for example, we may set them to have the length of $u_1(t)$ and $u_2(t)$).

2.3.3 Combined system

We now have a combined system where our unknowns are the source durations $\boldsymbol{\tau}$ and what we will refer to as the "pre-weighted" source functions $\mathbf{y}(= \mathbf{W}^{-1}\mathbf{x})$. Our aim is to obtain $\mathbf{y}$ such that $\mathbf{AWy} = \mathbf{0}$, subject to the constraint $\mathbf{e}^T\mathbf{Wy} - 1 = 0$. We write the Lagrange function as

$$L(\mathbf{y}, \lambda, \boldsymbol{\tau}) = \frac{1}{2} \parallel \mathbf{AW}(\boldsymbol{\tau})\mathbf{y} \parallel^2 + \frac{\beta}{2}\mathbf{y}^T\boldsymbol{\Sigma}^{-1}\mathbf{y} - \lambda(\mathbf{e}^T\mathbf{W}(\boldsymbol{\tau})\mathbf{y} - 1) \tag{2.9}$$

where λ is a Lagrange multiplier. Since the matrix $\mathbf{W}^T(\boldsymbol{\tau})\mathbf{A}^T\mathbf{AW}(\boldsymbol{\tau})$ is singular or close to singular, we add a regularization term with Tikhonov parameter β. We introduce the model prior covariance matrix $\boldsymbol{\Sigma} = E[\mathbf{y}\mathbf{y}^T]$ into the regularization term in order to take into account the band limited nature of the seismograms. The term $\frac{1}{2} \parallel \mathbf{AW}(\boldsymbol{\tau})\mathbf{y} \parallel^2$ refers to the error misfit, $\frac{\beta}{2}\mathbf{y}^T\boldsymbol{\Sigma}^{-1}\mathbf{y}$ to the model variance and $\lambda(\mathbf{e}^T\mathbf{W}(\boldsymbol{\tau})\mathbf{y} - 1)$ to the scaling constraint. We shall minimize the Lagrange function L with respect to $\mathbf{y}$, λ and $\boldsymbol{\tau}$.

2.3.4 Separation of variables

It is difficult to minimize the objective function in Equation 2.9 since there is a non-linear dependence on $\boldsymbol{\tau}$. We will use the separation of variables approach suggested by *Golub and Pereyra* [1973] (see also review in *Golub and Pereyra* [2003]) to solve the non-linear problem. Our approach will be to alternately minimize a modified objective function with respect to the linear parameters $\mathbf{y}$ and λ, and then with respect to the non-linear parameters $\boldsymbol{\tau}$. The approach is particularly attractive since the problem is quadratic with respect to $\mathbf{y}$. Thus, given $\boldsymbol{\tau}$ we solve a quadratic programing problem for $\mathbf{y}$ and λ,

$$\begin{bmatrix} \mathbf{W}(\boldsymbol{\tau})^T\mathbf{A}^T\mathbf{AW}(\boldsymbol{\tau}) + \boldsymbol{\Sigma}^{-1} & \mathbf{W}(\boldsymbol{\tau})\mathbf{e} \\ \mathbf{e}^T\mathbf{W}(\boldsymbol{\tau}) & 0 \end{bmatrix} \begin{bmatrix} \mathbf{y}(\boldsymbol{\tau}) \\ \lambda(\boldsymbol{\tau}) \end{bmatrix} = -\nabla L \tag{2.10}$$

and rewrite the Lagrange function in terms of $\boldsymbol{\tau}$ alone

$$L(\mathbf{y}(\boldsymbol{\tau}),\lambda(\boldsymbol{\tau}),\boldsymbol{\tau}) = \tfrac{1}{2} \parallel \mathbf{AW}(\boldsymbol{\tau})\mathbf{y}(\boldsymbol{\tau}) \parallel^2 + \tfrac{\beta}{2}\mathbf{y}(\boldsymbol{\tau})^T\boldsymbol{\Sigma}^{-1}\mathbf{y}(\boldsymbol{\tau}) \tag{2.11}$$

$$-\lambda(\boldsymbol{\tau})(\mathbf{e}^T\mathbf{W}(\boldsymbol{\tau})\mathbf{y}(\boldsymbol{\tau}) - 1). \tag{2.12}$$

The solution is then obtained by finding a stationary point of the Lagrange function with respect to $\boldsymbol{\tau}$.

To be more specific, to solve the linear system Equation 2.10 we note that we can solve for $\mathbf{y}$ as a function of λ

$$\mathbf{y}(\boldsymbol{\tau}) = \lambda(\mathbf{W}^T(\boldsymbol{\tau})\mathbf{A}^T\mathbf{AW}(\boldsymbol{\tau}) + \beta\boldsymbol{\Sigma}^{-1})^{-1}\mathbf{W}^T\mathbf{e}. \tag{2.13}$$

Setting $\hat{\mathbf{y}} = \frac{\mathbf{y}}{\lambda}$ yields

$$\hat{\mathbf{y}}(\boldsymbol{\tau}) = (\mathbf{W}^T(\boldsymbol{\tau})\mathbf{A}^T\mathbf{AW}(\boldsymbol{\tau}) + \beta\boldsymbol{\Sigma}^{-1})^{-1}\mathbf{W}^T\mathbf{e}, \tag{2.14}$$

and, by multiplying the both sides of Equation 2.13 by $\mathbf{e}^T\mathbf{W}$ from the left, we obtain using the second equation in Equation 2.10

$$\lambda = \frac{1}{\mathbf{e}^T\mathbf{W}\hat{\mathbf{y}}}. \tag{2.15}$$

The non-linear problem in $\boldsymbol{\tau}$ is addressed by differentiating L with respect to the elements of $\boldsymbol{\tau}$, i.e.

$$\frac{dL}{d\boldsymbol{\tau}} = \frac{\partial\mathbf{y}}{\partial\boldsymbol{\tau}}\frac{\partial L}{\partial\mathbf{y}} + \frac{\partial\lambda}{\partial\boldsymbol{\tau}}\frac{\partial L}{\partial\lambda} + \frac{\partial L}{\partial\boldsymbol{\tau}}, \tag{2.16}$$

exploiting $\frac{\partial L}{\partial\mathbf{y}} = \mathbf{0}$ and $\frac{\partial L}{\partial\lambda} = 0$ from the linear problem and setting Equation 2.16 to zero, to obtain

$$\mathbf{B}^T(\boldsymbol{\tau})\mathbf{Y}^T(\mathbf{A}^T\mathbf{AW}(\boldsymbol{\tau})\mathbf{y} - \lambda\mathbf{e}) = \mathbf{0}, \tag{2.17}$$

where $\mathbf{Y} = \mathsf{diag}(\mathbf{y})$ and $\mathbf{B}$ is a matrix containing the derivatives $\frac{\partial w_i(t,\boldsymbol{\tau})}{\partial \tau_i}$ along its columns. For example, for 2 sources, $\mathbf{B}(\boldsymbol{\tau})$ is written as follows:

$$\mathbf{B}(\boldsymbol{\tau}) = \begin{bmatrix} \frac{\partial w_1(t,\tau_1)}{\partial \tau_1} & \mathbf{0} \\ \mathbf{0} & \frac{\partial w_2(t,\tau_2)}{\partial \tau_2} \end{bmatrix}. \tag{2.18}$$

However, since the unknowns τ_i enter this system through $\mathbf{W}(\boldsymbol{\tau})$ in a non-linear fashion we must solve it using non-linear optimization. In particular, we use Newton's method to solve the linear system:

$$\mathbf{H}(\boldsymbol{\tau})\Delta\boldsymbol{\tau} = -\mathbf{g}(\boldsymbol{\tau}), \tag{2.19}$$

with

$$\mathbf{g}(\boldsymbol{\tau}) = (\mathbf{AYB})^T(\mathbf{AW}(\boldsymbol{\tau})\mathbf{y}) - \lambda\mathbf{B}^T\mathbf{Ye}). \tag{2.20}$$

The Hessian $\mathbf{H}(\boldsymbol{\tau})$ equals

$$\mathbf{H}(\boldsymbol{\tau}) = \mathbf{C}(\boldsymbol{\tau}) + \mathbf{D}(\boldsymbol{\tau}), \tag{2.21}$$

where

$$\mathbf{C}(\boldsymbol{\tau}) = (\mathbf{AYB})^T\mathbf{AYB} + \mathsf{diag}(\sum \frac{\partial^2}{\partial \boldsymbol{\tau}^2}(\mathbf{w}(\boldsymbol{\tau},\mathbf{t}))\,\mathbf{Y}^T\mathbf{A}^T\mathbf{AWy}), \tag{2.22}$$

and

$$\mathbf{D}(\boldsymbol{\tau}) = -\lambda\mathsf{diag}(\sum \frac{\partial^2}{\partial \boldsymbol{\tau}^2}(\mathbf{w}(\boldsymbol{\tau},\mathbf{t}))\,\mathbf{Ye}). \tag{2.23}$$

Using separation of variables, we proceed iteratively to converge to a solution. At each iteration we first recover $\mathbf{y}$ and λ by solving the linear system Equation 2.10 and then solve the linearized system Equation 2.19 to update $\boldsymbol{\tau}$. This procedure is repeated until a stopping criterion is satisfied.

The separation of variables approach is useful and efficient in our case since the

number of unknowns in the non-linear problem Equation 2.17 (which is difficult to solve) is small relative to the linear problem Equation 2.13 (which is relatively easy to solve). Indeed, the number of unknowns in the non-linear problem corresponds to the number of sources we are trying to obtain whereas the number of unknowns in the linear problem corresponds to the number of points of all the sources. The alternative of solving one very large non-linear optimization problem would be extremely difficult.

2.3.5 Stopping criterion

From one perspective, the elements of $\boldsymbol{\tau}$ can be regarded as regularization parameters that are to be chosen such that the source time functions embodied in $\mathbf{x}$ are as short as possible while still solving the system in Equation 2.8. While the τ_i are too short, the data misfit (or, more accurately the first term in the LHS of Equation 2.9) is large. When the τ_i are larger than some set of "optimum" values, the data misfit remains effectively unchanged. In this sense our solution is one of regularization by minimum support. Adopting this rationale, we consider a stopping criterion that invokes Generalized Cross Validation (GCV) with $\boldsymbol{\tau}$ as the regularization parameter. Note that β in Equation 2.13 is held fixed in our work at a small value that is just sufficient to render the linear system non-singular and does not enter the primary regularization enforced by $\boldsymbol{\tau}$. To construct the GCV parameter $GCV_{mod}(\boldsymbol{\tau})$ we first recast the constrained minimization problem as an equivalent least squares problem. Consider, for example, the case where our scaling in Equation 2.5 is applied to the first point of the first source, that is $s_1(1) = 1$. We rewrite the system in Equation 2.5 as:

$$\mathbf{A}_1 s_1(1) + \mathbf{A}'\mathbf{s}' = \mathbf{0}, \tag{2.24}$$

in which

$$\mathbf{A} = \left[\begin{array}{c:c} \mathbf{A}_1 & \mathbf{A}' \end{array}\right] \quad \text{and} \quad \mathbf{x} = \left[\begin{array}{c} s_1(1) \\ \hdashline \mathbf{s}' \end{array}\right]. \tag{2.25}$$

Setting $s_1(1) = 1$ and introducing $\mathbf{s}' = \mathbf{W}'\mathbf{y}'$, the system Equation 2.24 becomes

$$\mathbf{A}'\mathbf{W}'\mathbf{y}' = -\mathbf{A}_1, \tag{2.26}$$

where $\mathbf{W}'$ is equivalent to $\mathbf{W}$ with the first column and first row removed. It can be easily shown, using the leave-one-out lemma [*Aster et al.*, 2005] that the modified GCV parameter employing $\mathbf{W}'(\boldsymbol{\tau})$ as the regularization agent, can be written as:

$$GCV_{mod}(\boldsymbol{\tau}) = \frac{m||\mathbf{A}'\mathbf{W}'\mathbf{y}' + \mathbf{A}_1||^2}{(\mathsf{trace}(\mathbf{I} - \mathbf{A}'\mathbf{W}'\mathbf{A}^{\#}))^2} \tag{2.27}$$

with

$$\mathbf{A}^{\#} = (\mathbf{W}'^T\mathbf{A}'^T\mathbf{A}'\mathbf{W}' + \beta\boldsymbol{\Sigma}'^{-1})^{-1}\mathbf{W}'^T\mathbf{A}'^T, \tag{2.28}$$

where $\boldsymbol{\Sigma}'$ is equivalent to $\boldsymbol{\Sigma}$ with the first column and first row removed, and m is the column dimension of $\mathbf{A}'$. The numerator in Equation 2.27 represents the misfit in the regularized system whereas the denominator represents the effective degrees of freedom squared [*Hansen*, 1998].

As $\boldsymbol{\tau}$ increases, $GCV_{mod}(\boldsymbol{\tau})$ decreases, though sometimes irregularly, but eventually bottoms out as opposed to reaching a minimum and subsequently increasing, as in classical problems. From visual inspection, acceptable solutions are recovered for $\boldsymbol{\tau}$ corresponding to the corner of this "L"-shaped $GCV_{mod}(\boldsymbol{\tau})$ function.

2.4 Algorithm

1. Select a set of initial (short) lengths $\boldsymbol{\tau}_0$ for the sources.

2. Solve linear problem:

$$\mathbf{y}(\boldsymbol{\tau}_0) = \lambda(\mathbf{W}^T(\boldsymbol{\tau}_0)\mathbf{A}^T\mathbf{A}\mathbf{W}(\boldsymbol{\tau}_0) + \beta\boldsymbol{\Sigma}^{-1})^{-1}\mathbf{W}^T(\boldsymbol{\tau}_0)\mathbf{e}$$

3. Compute threshold $GCV_{mod}(\boldsymbol{\tau}) = \frac{m||\mathbf{A}'\mathbf{W}'\mathbf{y}'+\mathbf{A}_1||^2}{(\mathsf{trace}(\mathbf{I}-\mathbf{A}'\mathbf{W}'\mathbf{A}^{\#}))^2}$

4. While stopping criterion not satisfied

   4.1 Solve non linear part

$$\Rightarrow \quad \Delta\boldsymbol{\tau} = -\mathbf{H}^{-1}(\boldsymbol{\tau}_k)\mathbf{g}(\boldsymbol{\tau}_k)$$

   4.2 Update $\boldsymbol{\tau}_{k+1} = \boldsymbol{\tau}_k + \Delta\boldsymbol{\tau}$

   4.3 Repeat parts 2. and 3.

5. Solution $\mathbf{x} = \mathbf{W}\mathbf{y}$ if the stopping criterion is satisfied

2.5 Results

The algorithm explained in previous sections has been tested on several synthetic datasets. These examples are meant to be simplified representations of teleseismic body wave seismograms [*Bostock*, 2007]. Primary body wave phases, such as teleseismic P, are recorded from distant ($> 30^\circ$) earthquakes on three-component seismometers with geometries like those indicated in Figure 2.1. The dominant scattering contributions arise from structures in the near-source and/or near-receiver regions (Earth's heterogeneity tends to be more pronounced in the crust and upper mantle than at greater depths). Receiver-side structure which is of interest here is conventionally accessed through so-called receiver function analysis [*Langston*, 1977, *Vinnik*, 1977] that relies

heavily upon the minimum phase nature of the seismogram component in the incident mode [*Bostock*, 2007]. In *P*-receiver function analysis, the *S*-components of motion are deconvolved by the *P*-components to produce a source free impulse response (i.e. the receiver function) that approximates the *S*-component of the Green's function and can be interpreted in terms of discontinuities in various shear related properties (e.g. *S*-velocity, *S*-impedance). However, this approach sacrifices information residing within the *P*-component that pertains to different (compressional) modulli and so a more general approach that retrieves the full three-component Green's function is desired. We examine multichannel deconvolution to this end. We may consider three-component seismograms as representing three different components of the Green's function each convolved with the same source, thereby creating a redundancy of up to a factor of 3 over the single component system represented in Equation 2.3.

The *P*-component and *S*-component Green's functions used in the numerical experiments are shown in Figure 2.3 and represent the leading order response of a simplified crustal model comprising a 36 km thick layer (elastic wave velocities and density equal to $V_P = 6000$ m/s, $V_S = 3464$ m/s, $\rho = 2700$ kg/m^3) bounded by free surface above and half-space mantle (elastic wave velocities and density equal to $V_P = 8000$ m/s, $V_S = 4619$ m/s, $\rho = 3300$ kg/m^3) below, to an impulsive plane *P*-wave with slowness $p = 0.06$ s/km. The large arrival on the *P*-component at time $t = 0$ s represents the incident *P*-wavefield whereas the remaining arrivals on both P and S components comprise first-order scattering interactions formed through either direct *P*-to-*S* mode conversion (the $P_M s$ arrival at time $t = 4$ s on the *S*-component) or through reverberation at the free surface ($Pp_M p$ at $t = 12$ s, $Ps_M p$ at $t = 16$ s on the *P*-component and $Pp_M s$ at $t = 16$ s, $Ps_M s$ at $t = 19$ s on the *S*-component, see Figure 2.1). Because the model is 1-D and isotropic we consider only the *P*-component and the sagittal *S*-component that couples to the incident *P*-wavefield, since the transverse *S*-component is zero. Figure 2.4 and Figure 2.5 display the convolution of these Green's functions with 2 sets of 4 sources. The first set of sources comprises random Gaussian time series of length 35.5 seconds (Figure 2.4), whereas the second set is slightly more realistic in that the sources are band limited and extracted from real (decimated) *P*-wave seismograms (Figure 2.5). Both sets of seismograms are used as input to the blind deconvolution algorithm upon

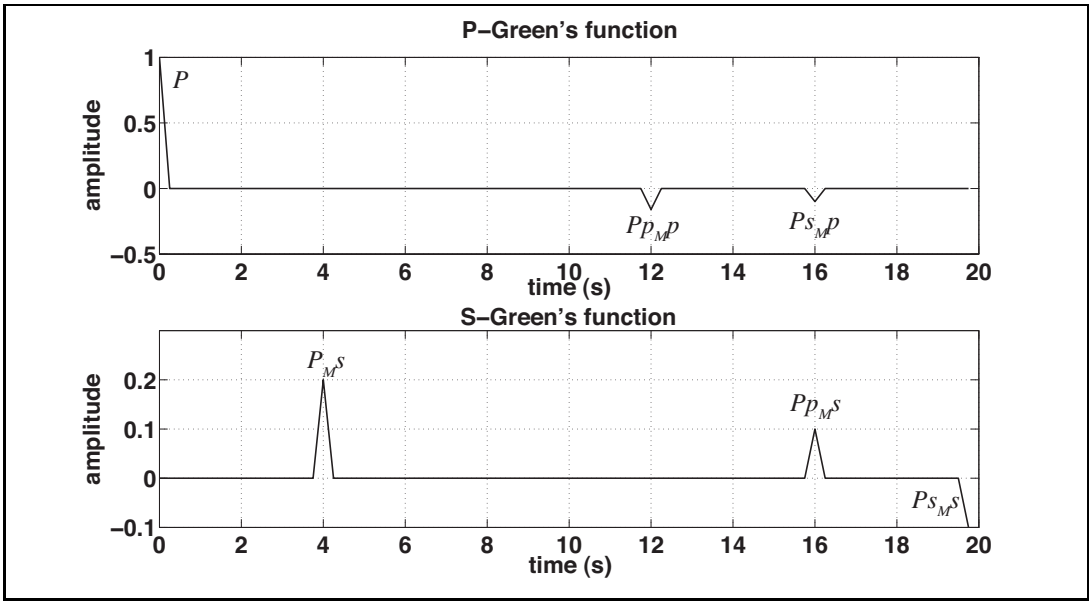

FIGURE 2.3: *P*-component of Green's function (upper panel) and *S*-component (lower panel) of Green's function employed in numerical experiments. Phase labels refer to scattered wave geometries illustrated in lower panel of Figure 2.1.

addition of random white noise at 1% of the peak amplitude of *P*-component seismograms (or, equivalently, approximately 10% of the scattered mode amplitudes).

The parameters used to perform the inversion are summarized in Table 2.1. The

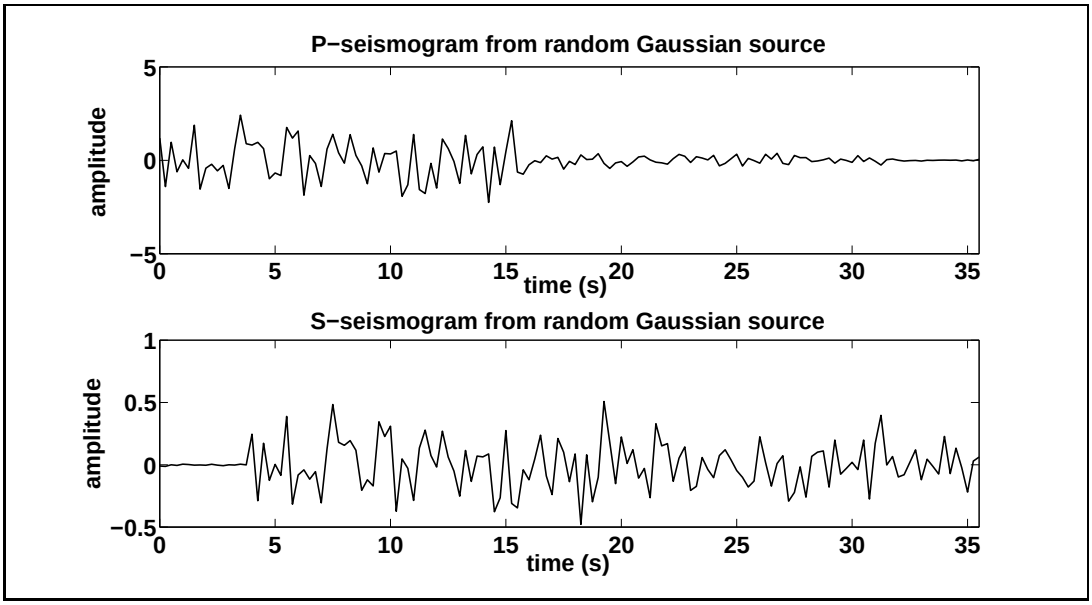

FIGURE 2.4: Example *P*- and *S*-seismograms generated from the convolution of *P*-component Green's function (upper panel) and *S*-component Green's function (lower panel) with random Gaussian source number 1.

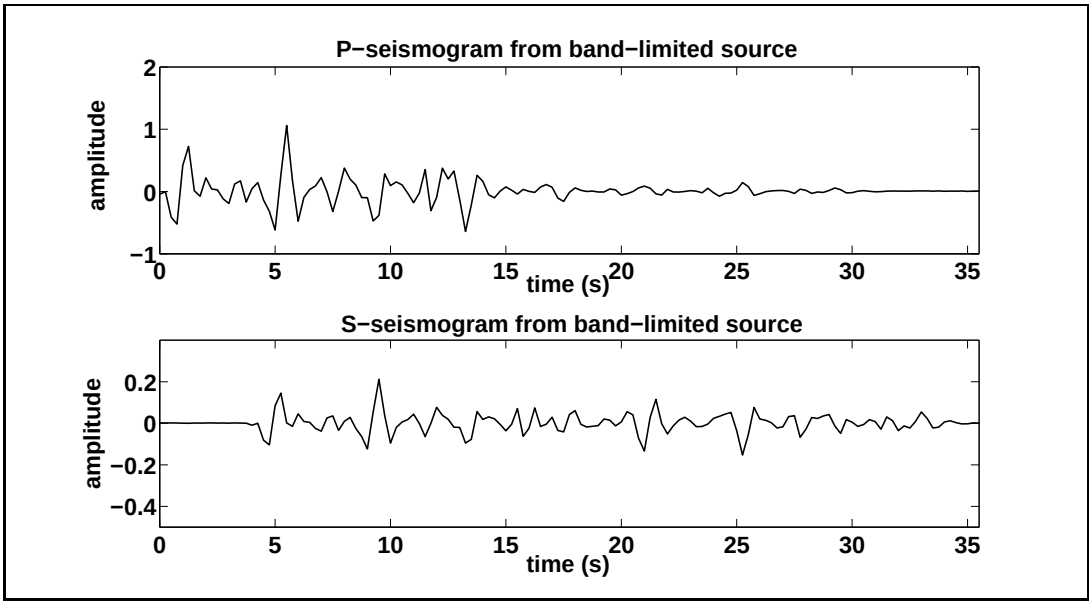

FIGURE 2.5: Example *P*- and *S*-seismograms generated from convolution of *P*-component Green's function (upper panel) and *S*-component Green's function (lower panel) with band-limited source number 1.

fig.	initial system	noise (% of peak P)	β	constraint	$\boldsymbol{\tau}_0(1:4)$	a	iter.
8	P Gaussian	1	1e-3	e(15)=1	15	20	910
9	S Gaussian	1	1e-3	e(15)=1	15	16	2060
10	P+S Gaussian	1	1e-3	e(15)=1	15	16	1200
11	P band-limited	1	5e-5	e(23)=1	23	20	1230
12	S band-limited	1	1e-5	e(23)=1	23	16	900
13	P+S band-limited	1	1e-4	e(23)=1	23	20	355

TABLE 2.1: Inversion parameters employed in numerical experiments.

β parameter is held fixed in our work at a small value that is just sufficient to render the linear system non-singular and does not enter the primary regularization enforced by $\boldsymbol{\tau}$. Because the *P*-component in the Green's function is minimum phase and, in particular, dominated by the direct arrival at $t = 0$ s, we may choose our scaling constraint $s_i(t) = 1$ to correspond to a point t on the observed *P*-component seismogram that exhibits large relative amplitude. In addition, this point must be chosen so as to fall within a time interval that does not exceed the length of the corresponding source function. Accordingly, the parameters $\boldsymbol{\tau}_0$ should be chosen to be consistent with the choice of scaling point, that is they should correspond to times equal to or greater than the timing of the scaling constraint. Needless to say, for computational efficiency sake, the $\boldsymbol{\tau}_0$ should be chosen to be as long as possible while remaining shorter than the

true source durations. The parameter a controls the steepness of the window function $w_i(t, \tau_i)$, (see Equation 2.6). Choice of too small a value for a forces $\Delta\boldsymbol{\tau}$ to be small at each iteration and substantially increases computation time. If the a is chosen too large, the effective support of $\mathbf{x}$ will exceed the true length of the sources.

Figure 2.6 to Figure 2.11 display results from 3 classes of experiments summarized schematically in Table 2.2 using the 2 sets of sources described above. These experiments include inversion using P-components alone, S-components alone, and P- and S-components simultaneously. Figure 2.6(a), Figure 2.7(a) and Figure 2.8(a) show results

experiment 1	experiment 2	experiment 3
$\mathbf{A} =$ [P-seismograms]	$\mathbf{A} =$ [S-seismograms]	$\mathbf{A} =$ [P-seismograms / S-seismograms]

TABLE 2.2: Schematic representation of the 3 classes of experiment.

for the 4 random Gaussian sources. The solutions (dashed grey curves) are retrieved at the corners of the GCV_{mod} parameter versus iteration number curves (black triangles in Figure 2.6(b), Figure 2.7(b) and Figure 2.8(b)) corresponding to 910, 2060 and 1200 iterations for the 3 experiments, and are compared to the true solution (solid black curves). Here we note that the $GCV_{mod}(\boldsymbol{\tau})$ parameter defined in Equation 2.27 behaves differently from that used in more standard (i.e. regularized least-squares) problems as is evident in Figure 2.6(b), Figure 2.7(b) and Figure 2.8(b). As we proceed from low levels of regularization (small $\boldsymbol{\tau}$ and short source time functions) to high levels (large $\boldsymbol{\tau}$ and long source time functions), $GCV_{mod}(\boldsymbol{\tau})$ decreases, though sometimes irregularly, but eventually bottoms out as opposed to reaching a minimum and subsequently increasing, as in classical problems. This behavior is presumably due to the fact that the misfit ($m||\mathbf{A}'\mathbf{W}'\mathbf{y}' + \mathbf{A}_1||^2$) in Equation 2.27 remains constant after the optimum (shortest) solution is reached regardless of the values of $\boldsymbol{\tau}$. We have found from visual inspection that acceptable solutions are recovered for $\boldsymbol{\tau}$ corresponding to the corner of

this "L"-shaped $GCV_{mod}(\boldsymbol{\tau})$ function. The GCV_{mod} curve in our experiments did not increase as $\boldsymbol{\tau}$ increased. We believe that this behaviour is due to the special structure of the noise associated with our problem, notably that it enters the RHS of the system in Equation 2.3. Indeed, in experiments where random noise was added to the right hand side of Equation 2.26, the GCV behaved "normally" decreasing at first and then increasing as β increased. Stopping at the corner of the GCV_{mod} curve implies that we select the solution with the least degrees of freedom that generates a small generalized cross validation measure. In all experiments source waveforms, durations and relative amplitudes are well recovered. Figure 2.9(a), Figure 2.10(a) and Figure 2.11(a) show results of 3 experiments using the set of 4 band-limited sources presented earlier in the section. The solutions (dashed-grey curve) are retrieved using GCV_{mod} at 1230, 900 and 355 iterations (black triangles in Figure 2.9(b), Figure 2.10(b) and Figure 2.11(b)), and again are compared to the true solutions (solid black curves). In this case we have employed a model prior covariance matrix $\boldsymbol{\Sigma}$ computed from a large number of decimated real *P*-wave seismograms. Again, source waveforms, durations and relative amplitudes are well recovered. The 3 classes of experiments yield good results, with a smaller number of iterations required to arrive to a solution for the P+S combination. However, the latter case involves an increase in the number of rows of the matrix A by a factor of 2 and thus increasing the computational burden.

2.6 Conclusion

We have described a method that is capable of solving the blind deconvolution problem when 2 or more seismograms are available that share a common convolutional element (source or Green's function). For the time series lengths considered here we are able to recover source time functions for noise levels at 1% of the direct P wave amplitude (time 0) (or approximately 10% of scattered wave amplitudes). One main challenge in future work will be to improve computational efficiency (execution' speed) so that realistic seismograms comprising time series with $10^3 - 10^4$ points can be accommodated. At present updating of $\Delta\boldsymbol{\tau}$ in the non-linear problem proceeds slowly (few

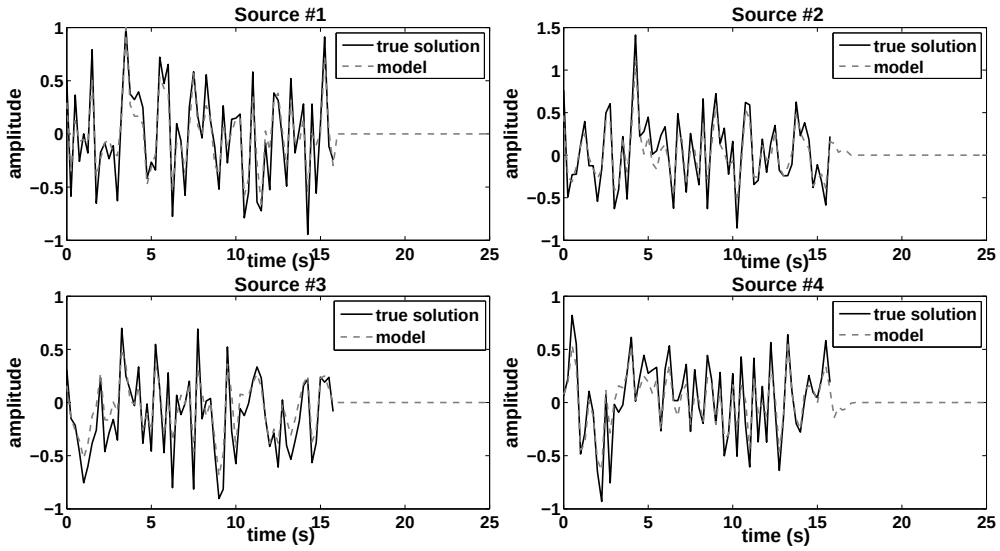

(a)

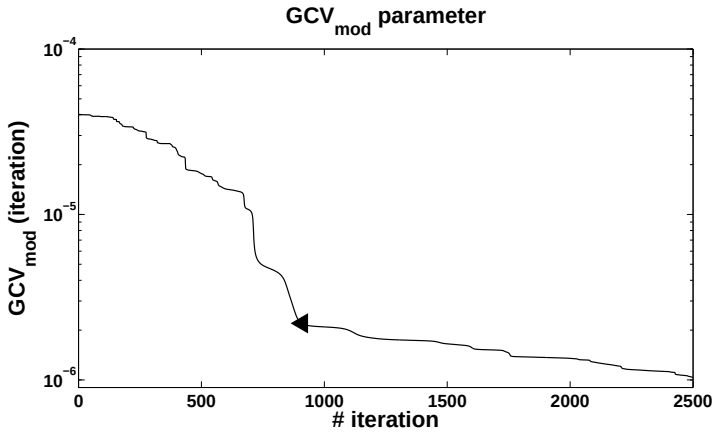

(b)

FIGURE 2.6: (a)Experiment 1: Inversion using random Gaussian sources and P-components alone. The true solution is shown in solid black and the recovered solution in dashed grey. (b) $GCV_{mod}(\boldsymbol{\tau})$ on random Gaussian sources. This example is set for 4 random Gaussian source-time functions, a noise-level equal to 1% of the peak P amplitude, $\beta = 1e-3$, $\boldsymbol{\tau}_0 = 15$, the scaling constraint $e(15) = 1$, $a = 20$. At the corner of the $GCV_{mod}(\boldsymbol{\tau})$ function (black triangle), a good solution is provided (panel (a)).

hours) through 1000's of iterations to achieve a short duration source solution. Multi-level methods that work first at low frequencies through to higher frequencies may offer solutions in this regard.

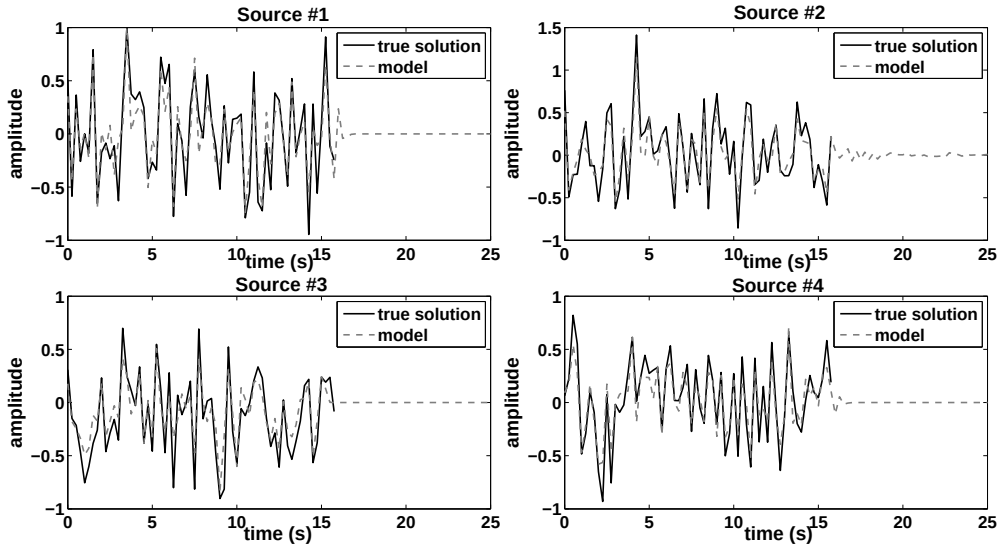

(a)

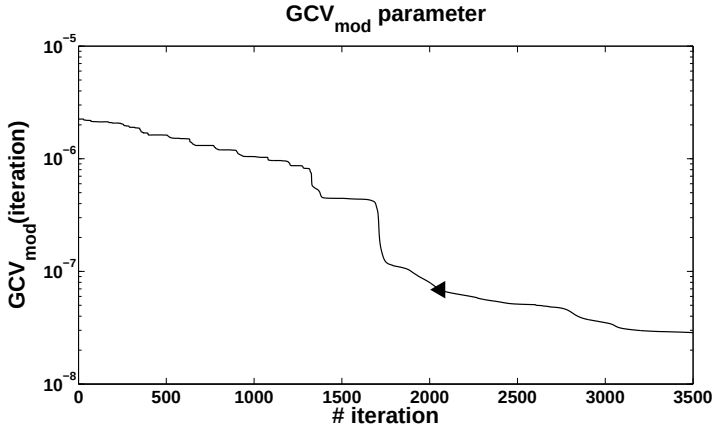

(b)

FIGURE 2.7: (a)Experiment 2: Inversion using random Gaussian sources and S-components alone. The true solution is shown in solid black and the recovered solution in dashed grey. (b) $GCV_{mod}(\boldsymbol{\tau})$ on random Gaussian sources. This example is set for 4 random Gaussian source-time functions, a noise-level equal to 1% of the peak P amplitude, $\beta = 1e-3$, $\boldsymbol{\tau}_0 = 15$, the scaling constraint $e(15) = 1$, $a = 16$. At the corner of the $GCV_{mod}(\boldsymbol{\tau})$ function (black triangle), a good solution is provided (panel (a)).

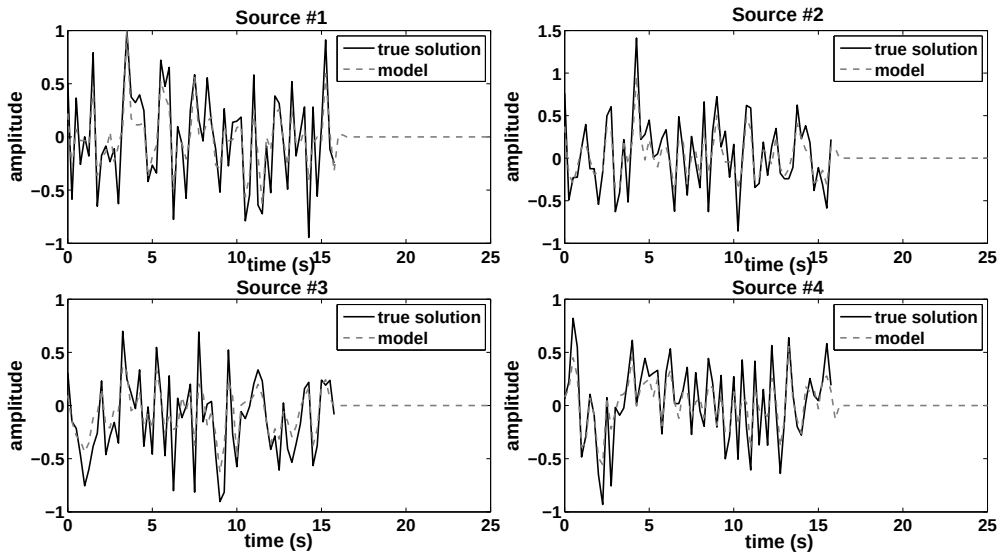

(a)

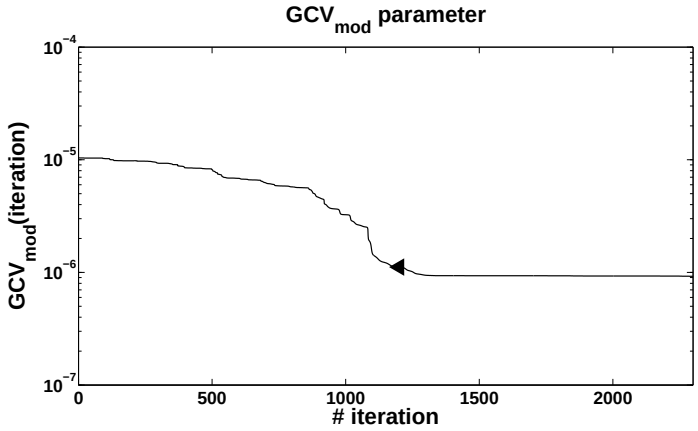

(b)

FIGURE 2.8: (a)Experiment 3: Inversion using random Gaussian sources and P- and S-components simultaneously. The true solution is shown in solid black and the recovered solution in dashed grey. (b) $GCV_{mod}(\boldsymbol{\tau})$ on random Gaussian sources. This example is set for 4 random Gaussian source-time functions, a noise-level equal to 1% of the peak P amplitude, $\beta = 1e-3$, $\boldsymbol{\tau}_0 = 15$, the scaling constraint $e(15) = 1$, $a = 16$. At the corner of the $GCV_{mod}(\boldsymbol{\tau})$ function (black triangle), a good solution is provided (panel (a)).

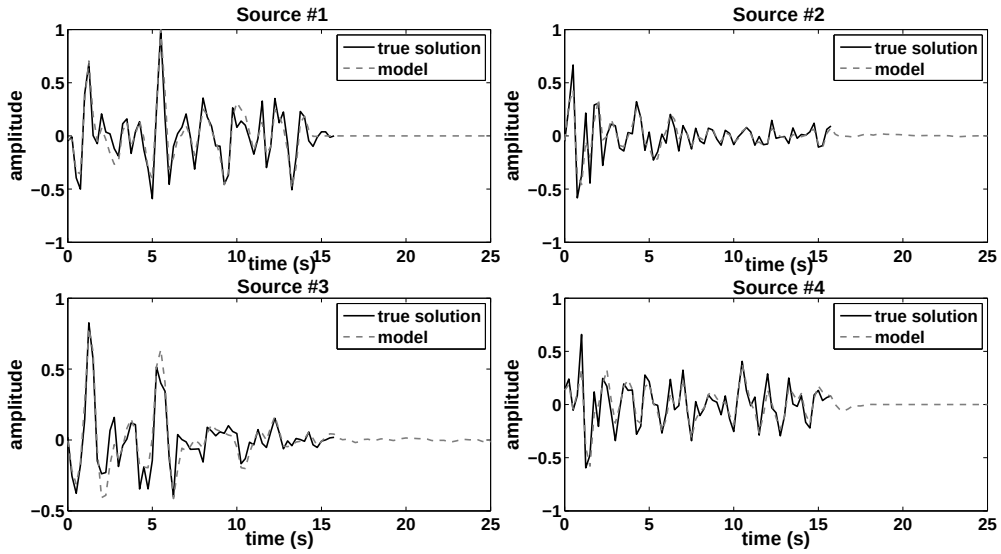

(a)

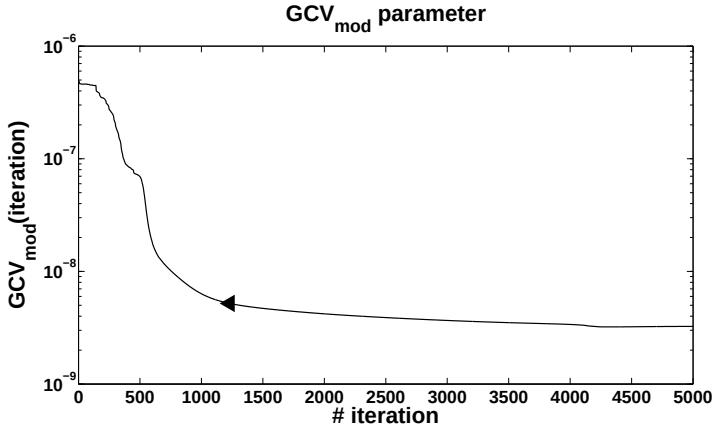

(b)

FIGURE 2.9: (a)Experiment 1: Inversion using band-limited sources and P-components alone. The true solution is shown in solid black and the recovered solution in dashed grey. (b) $GCV_{mod}(\boldsymbol{\tau})$ on band-limited sources. This example is set for 4 band-limited sources, a noise-level equal to 1% of the peak P amplitude, $\beta = 1e-5$, $\boldsymbol{\tau}_0 = 23$, the scaling constraint $e(23) = 1$, $a = 16$. At the corner of the $GCV_{mod}(\boldsymbol{\tau})$ function (black triangle), a good solution is provided (panel (a)).

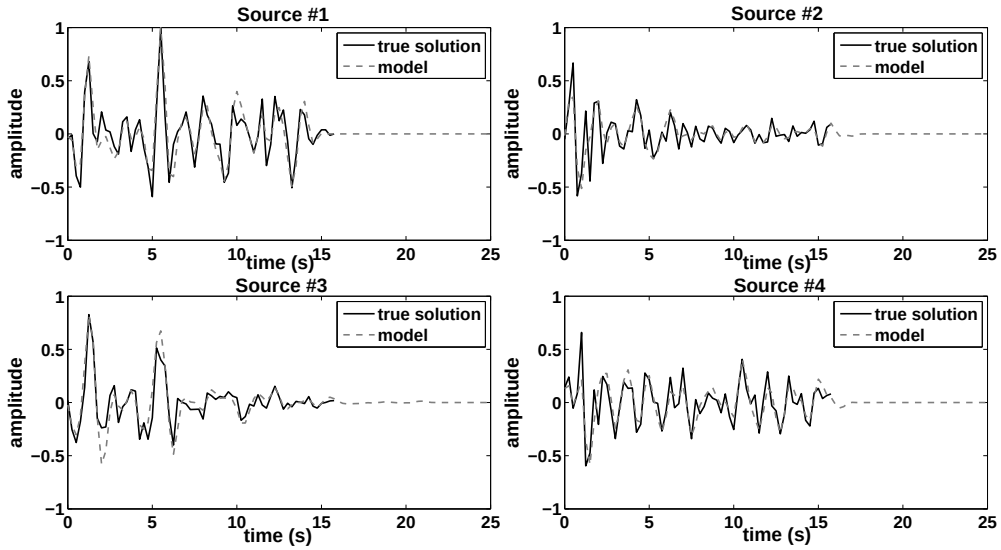

(a)

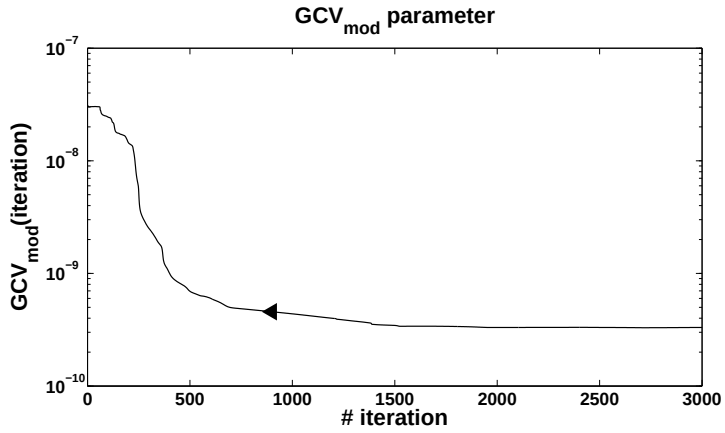

(b)

FIGURE 2.10: (a)Experiment 2: Inversion using band-limited sources and S-components alone. The true solution is shown in solid black and the recovered solution in dashed grey. (b) $GCV_{mod}(\boldsymbol{\tau})$ on band-limited sources. This example is set for 4 band-limited sources, a noise-level equal to 1% of the peak P amplitude, $\beta = 5e-5$, $\boldsymbol{\tau}_0 = 23$, the scaling constraint $e(23) = 1$, $a = 16$. At the corner of the $GCV_{mod}(\boldsymbol{\tau})$ function (black triangle), a good solution is provided (panel (a)).

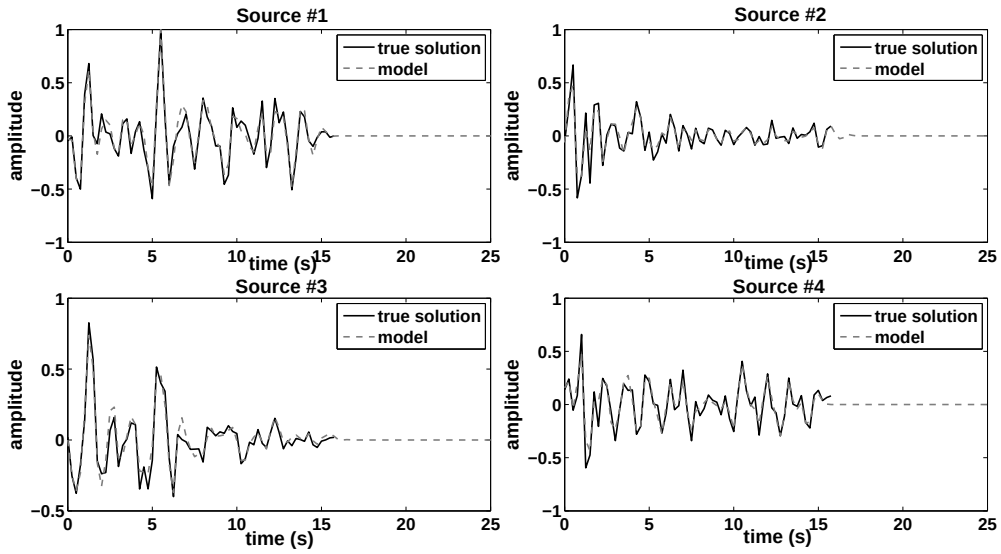

(a)

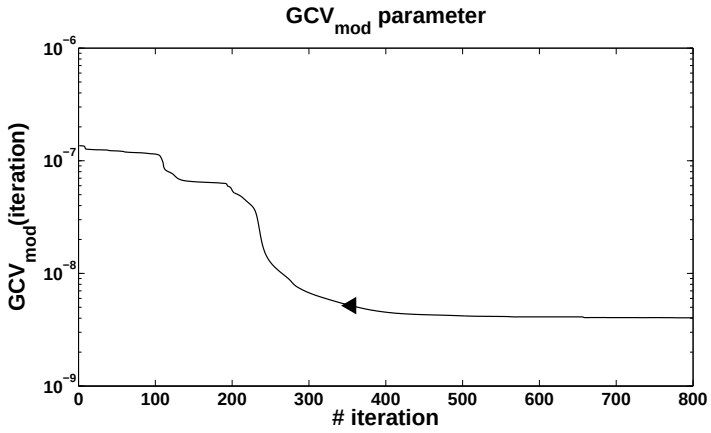

(b)

FIGURE 2.11: (a)Experiment 3: Inversion using band-limited sources and P- and S-components simultaneously. The true solution is shown in solid black and the recovered solution in dashed grey. (b) $GCV_{mod}(\boldsymbol{\tau})$ on band-limited sources. This example is set for 4 band-limited sources, a noise-level equal to 1% of the peak P amplitude, $\beta = 1e{-}4$, $\boldsymbol{\tau}_0 = 23$, the scaling constraint $e(23) = 1$, $a = 20$. At the corner of the $GCV_{mod}(\boldsymbol{\tau})$ function (black triangle), a good solution is provided (panel (a)).

Chapter 3

A comparative study of low frequency earthquake templates in northern Cascadia

3.1 Introduction

The discoveries of non-volcanic tremor by *Obara* [2002] just over a decade ago and its associations with slow slip [*Rogers and Dragert*, 2003] and low-frequency earthquakes [*Shelly et al.*, 2006] have opened many new avenues of study in seismology. Unlike regular earthquakes, the LFEs that constitute tremor may repeat 1000's of times over periods of a few years. Despite low magnitudes ($M < 3$) and limited bandwidth (1-10 Hz), these signals can be detected at low signal-to-noise ratio (SNR) thresholds and with high temporal precision using powerful network correlation techniques [*Brown et al.*, 2008, *Gibbons and Ringdal*, 2006, *Shelly et al.*, 2006]. Analysis of LFEs, and tremor more generally, can be facilitated through the generation of high SNR LFE templates assembled by stacking multitudes of aligned, repeating waveforms [e.g. *Bostock et al.*, 2012, *Frank et al.*, 2013, *Nowack and Bostock*, 2013, *Shelly and Hardebeck*, 2010]. The templates accentuate impulsive body wave arrivals allowing traveltimes to be measured more accurately, polarities to be determined with greater confidence and waveform distortion and scattered signals related to structure to be identified.

In this paper, we generate LFE templates from tremor recorded in northern Vancouver Island and Washington state, thereby extending a previous LFE catalogue for southern Vancouver Island [*Bostock et al.*, 2012] through much of northern Cascadia. We then provide empirical and semi-analytical arguments justifying the identification of LFE templates with "Green's function" sections corresponding to moment tensor point sources exhibiting a step-function time dependence in displacement. We proceed to compare the distribution and excitation of LFE sources across northern Cascadia as revealed by LFE templates and discuss implications for plate boundary structure and LFE genesis.

3.2 Data

Data employed in this study were collected from a variety of EarthScope sources that include Plate Boundary Observatory (PBO) short-period borehole installations, the transportable USArray (TA), and the Flexible Array experiments CAFE and FACES. In addition, we also employ data from permanent stations of the Canadian National Seismograph Network (CNSN) and the Pacific Northwest Seismic Network (PNSN), as well as portable POLARIS deployments on Vancouver Island. Data from southern Vancouver Island have been described previously by *Bostock et al.* [2012] and are included in this work for comparative purposes. The full suite of stations are shown in figure 3.1. Data were divided into 4 subarrays, namely northern Washington (NW), southern Washington (SW), northern Vancouver Island (NVI) and southern Vancouver Island (SVI), that were processed independently.

3.2.1 Washington state

The majority of data employed in the analysis of LFEs in Washington state were collected as part of the Flexible array CAFE experiment [*Abers et al.*, 2009, *Calkins et al.*, 2011]. We separate the dataset into NW and SW components. The former comprises 25 stations skirting the eastern flanks of the Olympic Peninsula to the west of Puget Sound, whereas the latter includes 25 stations running approximately east-west to the southwest of Puget Sound. Figure 3.1d displays the distribution of these stations.

For the NW dataset, major tremor episodes in 2007, 2008, 2009, 2010 and 2011 were recorded, but only data from the 2007 and 2008 tremor episodes were available for the SW subarray. Episodic tremor and slip episodes such as these typically last up to ∼3 weeks in Washington and southern Vancouver Island [*Rogers and Dragert*, 2003].

3.2.2 Vancouver Island

Tremor data for the NVI dataset were assembled from a portable POLARIS deployment on northern Vancouver Island that comprised 27 broadband seismometers deployed along two mutually perpendicular arms [*Audet et al.*, 2008], as shown in figure 3.1b. Two tremor episodes in 2006 and 2007 were available for analysis, each episode lasting under 1 week in duration. Analysis of LFEs for SVI relied heavily on a line of some 10 stations extending from the west coast of Vancouver Island (PFB) to the Gulf Islands (SNB) but also incorporated an additional >20 stations from surrounding areas. Tremor episodes in 2003, 2004 and 2005 were recorded at a majority of the stations, but data from subsequent episodes through 2012 have been incorporated for stations as available.

3.3 Data Processing

All data were divided into 24 hour-long segments, band-pass filtered between 1 and 8 Hz, resampled to 40 sps, and subjected to three distinct data processing steps to obtain LFE templates. These steps comprised i) network autocorrelation to identify pairs of repeat LFEs [*Brown et al.*, 2008], ii) waveform-correlation cluster analysis [*Rowe et al.*, 2002] to sort LFE detections into initial templates based on waveform similarity, and iii) network correlation [*Gibbons and Ringdal*, 2006, *Shelly et al.*, 2006] and stacking to increase detections and improve LFE template SNR. *Bostock et al.* [2012] provide details on processing of the SVI dataset, so we consider only NW, SW and NVI datasets below.

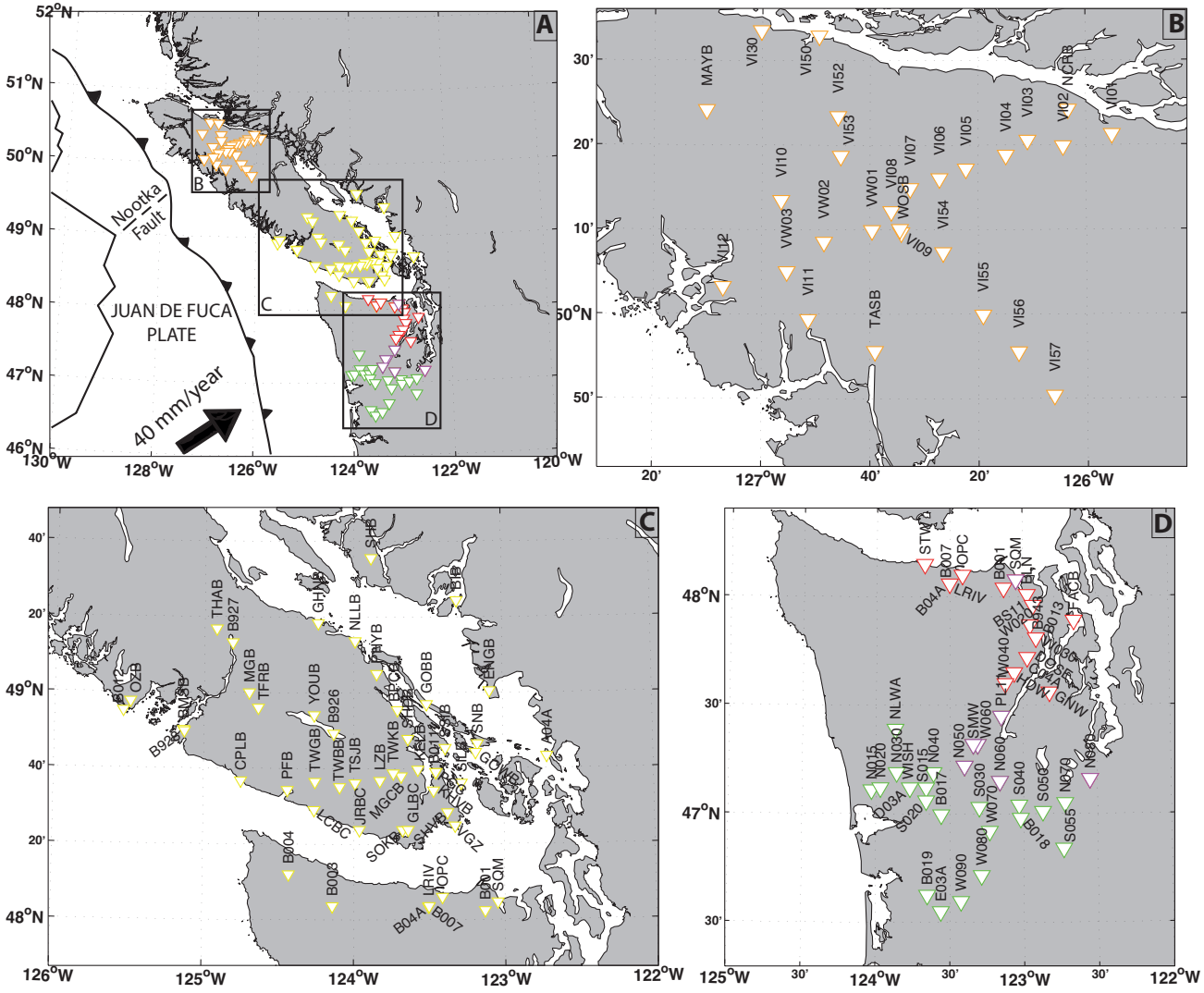

FIGURE 3.1: Distribution of stations used in the study of LFE templates in Washington state and Vancouver Island. Top left panel a) shows northern Cascadia region including plate boundary and color-coded station locations (NVI-orange, SVI-yellow, NW-red, SW-green, shared NW/SW-purple). Remaining panels b), c), d) show map insets of station locations for the NVI, SVI and collective NW and SW subarrays, respectively.

3.3.1 Network autocorrelation

For the NW dataset, we applied network autocorrelation to 4 tremor episodes (January 17-30 2007, May 01-23 2008, August 07-24 2010 and August 04-23 2011) using the 7 three-component stations B001, SQM, BS11, W020, W040, GNW and PL11. For the SW dataset, we performed network autocorrelation using 2 tremor episodes (January 14-February 01 2007, May 01-25 2008) and employed the 7 three-component stations N050, S030, W070, N060, PL11, S040 and N070. Network autocorrelation for the NVI dataset was applied to two tremor episodes (September 05-11 2006, June 13-18 2007) for different combinations of 7 of the 10 three-component stations VI10, VW03, VI11, VW02, VI52, VI53, VI05, VI08, VI06, VI04.

Each of these data sets was independently analysed on an hour-by-hour basis. Each hour-long segment was divided into 15 s windows lagged by 0.5 s to produce a total of 7170 individual windows per hour. Each window was correlated with all other windows in the same 1-hour record for an individual (station-component) channel. The resulting time-series from all stations and all components corresponding to the same hour were stacked to create "network autocorrelation" records. When the network autocorrelation exceeded 8 times the median absolute deviation [*Shelly et al.*, 2006], we registered the corresponding window pairs as LFE detections. This catalogue was then culled to exclude overlapping detections and retain only those with high SNR. After processing all data, we had selected 4915, 3306 and 4267 initial detections for further analysis from the NW, SW and NVI datasets, respectively.

3.3.2 Waveform-correlation cluster analysis

We proceeded to combine all channels corresponding to a given detection into a single "super" trace and cross-correlated all such traces against one another to determine maximum correlation coefficients and corresponding lags. The correlation coefficients were used to populate a similarity matrix employed within a hierarchical cluster analysis, allowing the detection waveforms to be grouped into clusters. Waveforms for all channels (stations/components) available for detections within a given cluster were shifted and stacked to produce an initial LFE template. This procedure resulted in 224, 70 and 54 initial templates for the NW, SW and NVI datasets, respectively.

3.3.3 Network cross-correlation

Iterative network cross-correlation and stacking was used to register further detections and improve template SNR. We performed network cross-correlation by choosing subsets of 7 to 10 high SNR, three-component stations available within a template and scanning through all available tremor dates. As before, when the summed network cross-correlation coefficient exceeded 8 times the median absolute deviation, now for a 24-hour period, we logged detections. New templates were formed by stacking waveforms (normalized to unit maximum amplitude across three components) for all newly registered detections. After several iterations of network cross-correlation and stacking, we obtained final sets of templates suitable for location and waveform analysis. Our final suites of templates number 122, 54 and 47 for the NW, SW and NVI datasets, respectively. Each template comprises 100's to 1000's of independent detections. Figure 3.2 shows examples of LFE templates from each of the NW, SW, NVI datasets. *S* arrivals can be clearly seen on both horizontal and vertical components and *P* arrivals can be clearly seen on the vertical component.

3.4 LFE templates as empirical Green's functions

In figure 3.3 we plot *P* and *S* waveforms at stations located near the center of NVI (top panels), NW (middle panels) and SW (bottom panel) arrays. In each panel, waveforms are ordered in increasing epicentral distance (ranging from 1 to 71 km, see following section) and aligned with respect to the dominant *P* or *S* arrival. *Bostock et al.* [2012, Figure 6] present a similar figure for the SVI data. In contrast to this previous study, we have applied a 90° phase shift (Hilbert transform) to the template waveforms that accomplishes partial transformation from particle velocity to particle displacement without altering the amplitude spectrum. The effects of post-critical scattering interactions that induce complex waveform distortions are minimized for these station selections because the majority of the propagation paths are near-vertical [*Booth and Crampin*, 1985].

As remarked by *Bostock et al.* [2012], the *P* and *S* waveforms for the full selection

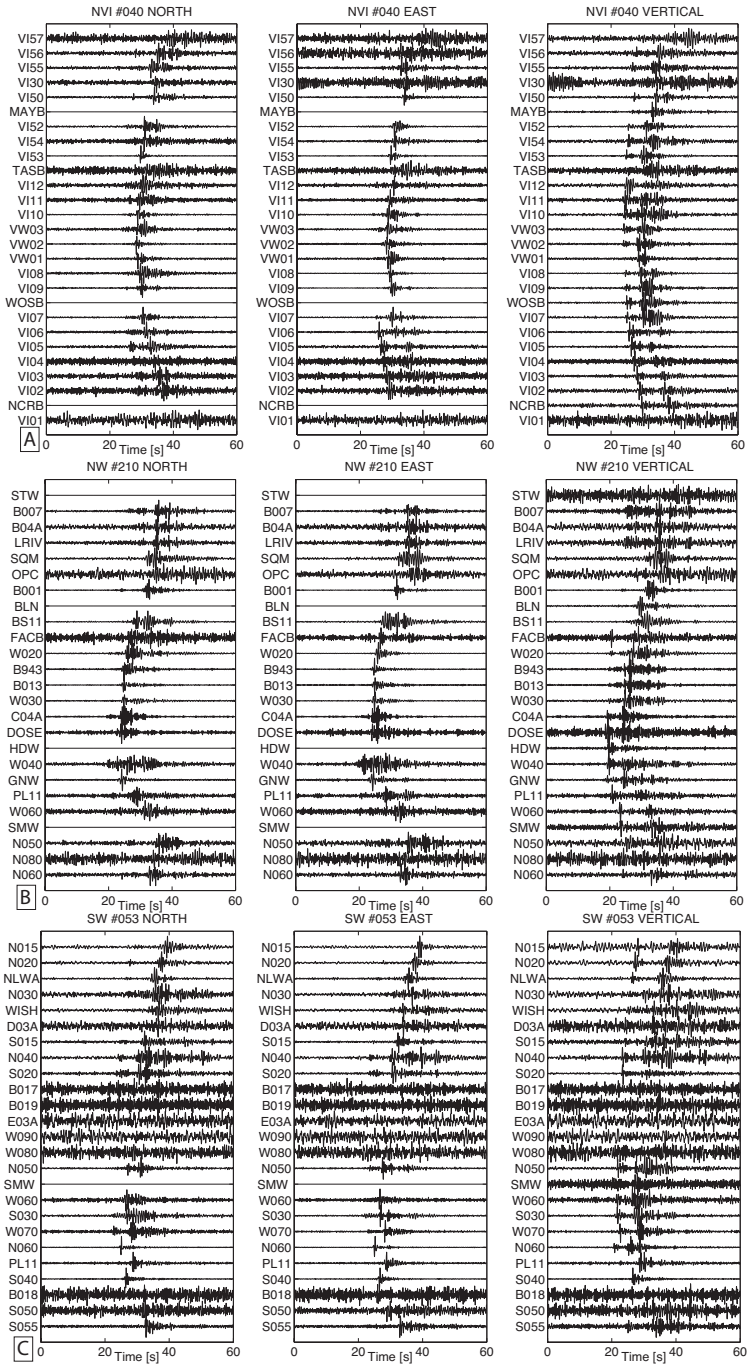

FIGURE 3.2: North (left), east (center) and vertical (right) components of 3 LFE templates from the a) NVI (template 040), b) NW (template 210) and c) SW (template 053) subarrays.

of templates at a given station display remarkable uniformity across the range of epicentral distances. Furthermore, the dipolar pulses observed in the earlier study and the bandlimited zero-phase pulses evident in figure 3.3 imply that the LFE templates can be considered as empirical Green's functions originating from a moment tensor point source with a step-function time dependence in displacement. Hilbert transformation of

the particle velocity records is practically useful because it aids in the identification of (band-limited) arrivals for location (section 3.5) and for waveform matching as required in moment tensor inversion (section 3.6) and recovery of structure from scattered waves [*Nowack and Bostock*, 2013].

The assertion that LFE templates produced by the iterative correlation-detection-stacking procedure can be considered as empirical Green's functions can be further justified as follows. Consider the single-channel cross correlation $c(t)$ of a (*e.g.* band-limited) Green's function estimate $\hat{g}(t)$ with a seismogram $u(t)$ that is itself the convolution of a source $s(t)$ with the corresponding true Green's function $g(t)$:

$$c(t) = \hat{g}(t) \otimes u(t) = \hat{g}(t) \otimes g(t) \star s(t) = \hat{\Phi}^g(t) \star s(t),$$

where $\otimes$ and $\star$ denote correlation and convolution, respectively. $\hat{\Phi}^g(t)$ is an estimate of the true autocorrelation of $g(t)$ and so will peak near lag $t = 0$. The timing of the maximum (or maxima) of $c(t)$ will depend on $s(t)$ but, owing to the timing of maximum in $\hat{\Phi}^g(t)$, will occur at or near the time(s) at which $s(t)$ possesses its maximum (maxima), say $t = t^{max}$. Note that $\hat{\Phi}^g(t)$ may contain significant subsidiary maxima at, for example, times equal to the *S*-*P* time if both *P*- and *S*-waves project onto the given channel with comparable amplitude and polarity. The contaminating influence of secondary peaks, any bias of the autocorrelation estimate maximum away from $t = 0$ and other forms of noise will be mitigated in the selection of t^{max} when the normalized cross correlations $c(t)/\sqrt{\int \hat{g}(\tau)^2 d\tau \int u(\tau)^2 d\tau}$ for many channels are combined within network correlation detection [*Gibbons and Ringdal*, 2006, *Shelly et al.*, 2006].

Once the detections are logged as described in section 3.3, the stack of corresponding seismograms $u_i(t)$ for a given channel, each shifted by the corresponding detection time t_i^{max}, can be written as

$$\sum_i u_i(t - t_i^{max}) = g(t) \star \sum_i s_i(t - t_i^{max}).$$

As the number of detections increases, the sum of band-limited source functions $s_i(t - t^{max})$, shifted such that their maxima align but assumed to be otherwise random, will tend toward a scaled, filtered delta function. The sum of shifted $u_i(t)$ thus becomes a

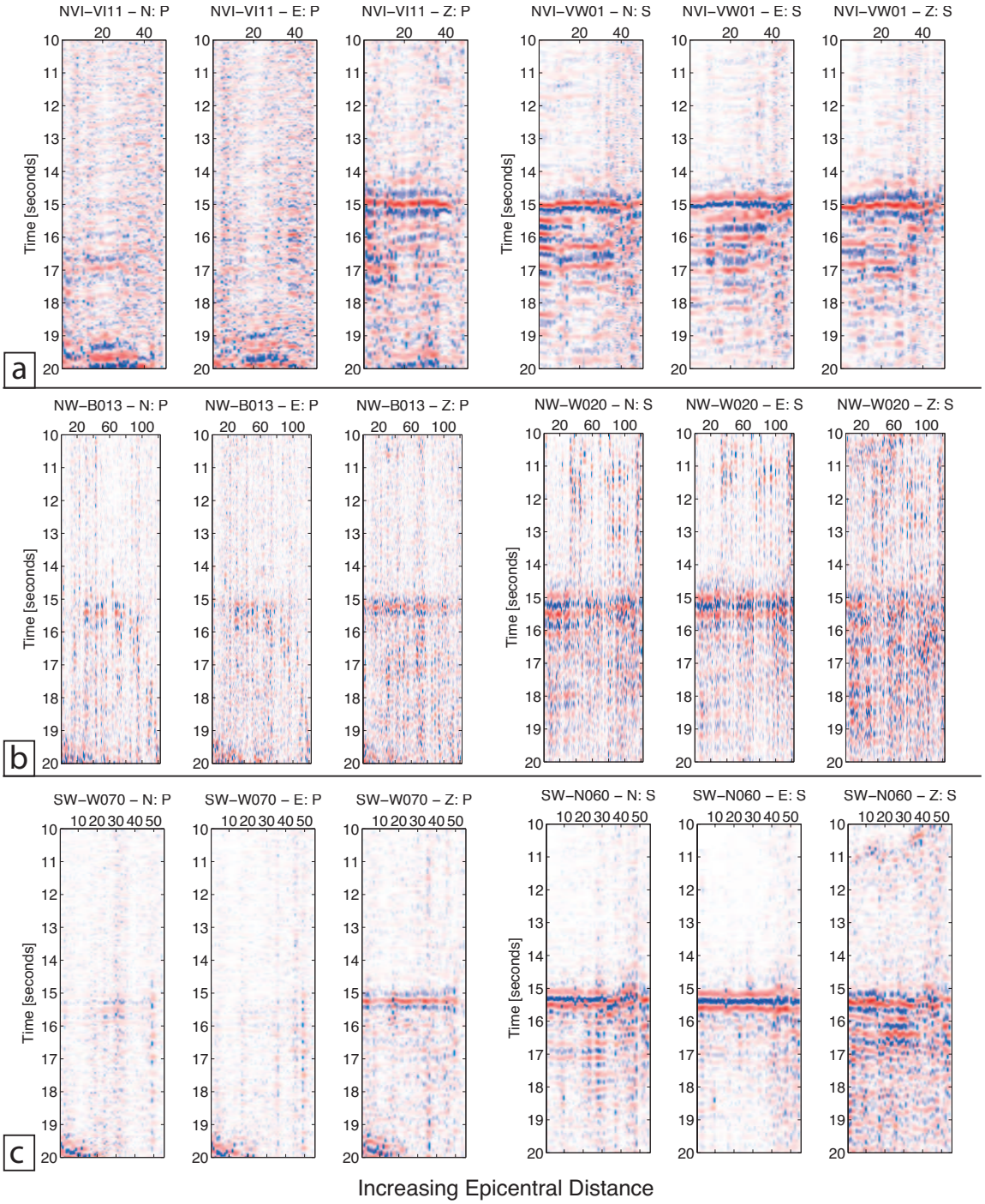

FIGURE 3.3: Three-component LFE template waveforms for individual stations aligned on direct P/S phases and plotted as functions of epicentral distance. a) NVI waveforms aligned on P for station VI11 and S for station VW01. b) NW waveforms aligned on P for station B013 and S for station W020. c) SW waveforms aligned on P for station 2070 and S for station N060. Red/blue polarities are positive/negative, respectively. Note simple zero-phase signatures of direct P and S.

scaled, band-limited approximation to $g(t)$ that can be used as an improved estimate $\hat{g}(t)$ to log further detections.

Approximate deconvolution through stacking of phase-normalized seismograms has been applied previously to long-period body waves [*Shearer*, 1991] and broadband teleseismic *P*-waves [*Kumar et al.*, 2010] using global earthquakes; however the relative infrequency of regular seismicity limits Green's function retrieval to 1-D estimates. In contrast, LFEs that repeat 1000's of times over periods of a few years allow fully 3-D empirical Green's functions to be assembled.

3.5 LFE template locations

A large proportion of stations represented within LFE templates display unambiguous zero-phase, impulsive P and S arrivals that can be timed and used to establish representative locations. We perform two locations, one using a standard linearized inversion [Hyp2000, *Klein*, 2002] and one using the double difference location algorithm [hypoDD, *Waldhauser*, 2001], both distributed by the United States Geological Survey. Figure 3.4 shows a map of LFE Hyp2000 epicenters (see supplementary figure A1 in Appendix A for hypoDD epicenters). Superimposed on this map are the 20, 30 and 40 km depth contours to the top of the subducting Juan de Fuca plate modelled by *Audet et al.* [2010] and *McCrory et al.* [2012].

Using the initial Hyp2000 locations, we apply the hypoDD algorithm to a combination of ordinary phase picks from our LFE catalog and differential travel times from phase correlation of *P*- and *S*-waves. The parameters used to perform the inversion are summarized in supplementary Table A1 in Appendix A. These parameters are set to produce a dynamic weighting scheme to optimize the least-squares solution. Solutions are found by iteratively adjusting the vector difference between nearby hypocentral pairs, with the locations and partial derivatives updated after each iteration. Events lacking close neighbours are automatically removed in this procedure such that 91%, 92%, 77% and 72% of the original events remain in hypoDD solutions for the NVI, SVI, NW and SW datasets, respectively. Mean, nominal uncertainties in horizontal and vertical locations as supplied by Hyp2000 for the individual subarrays are 1.8 km, 2.16 km (NVI), 1.1 km, 1.9 km (SVI), 2.0 km, 1.3 km (NW), and 3.7 km, 3.5 km (SW).

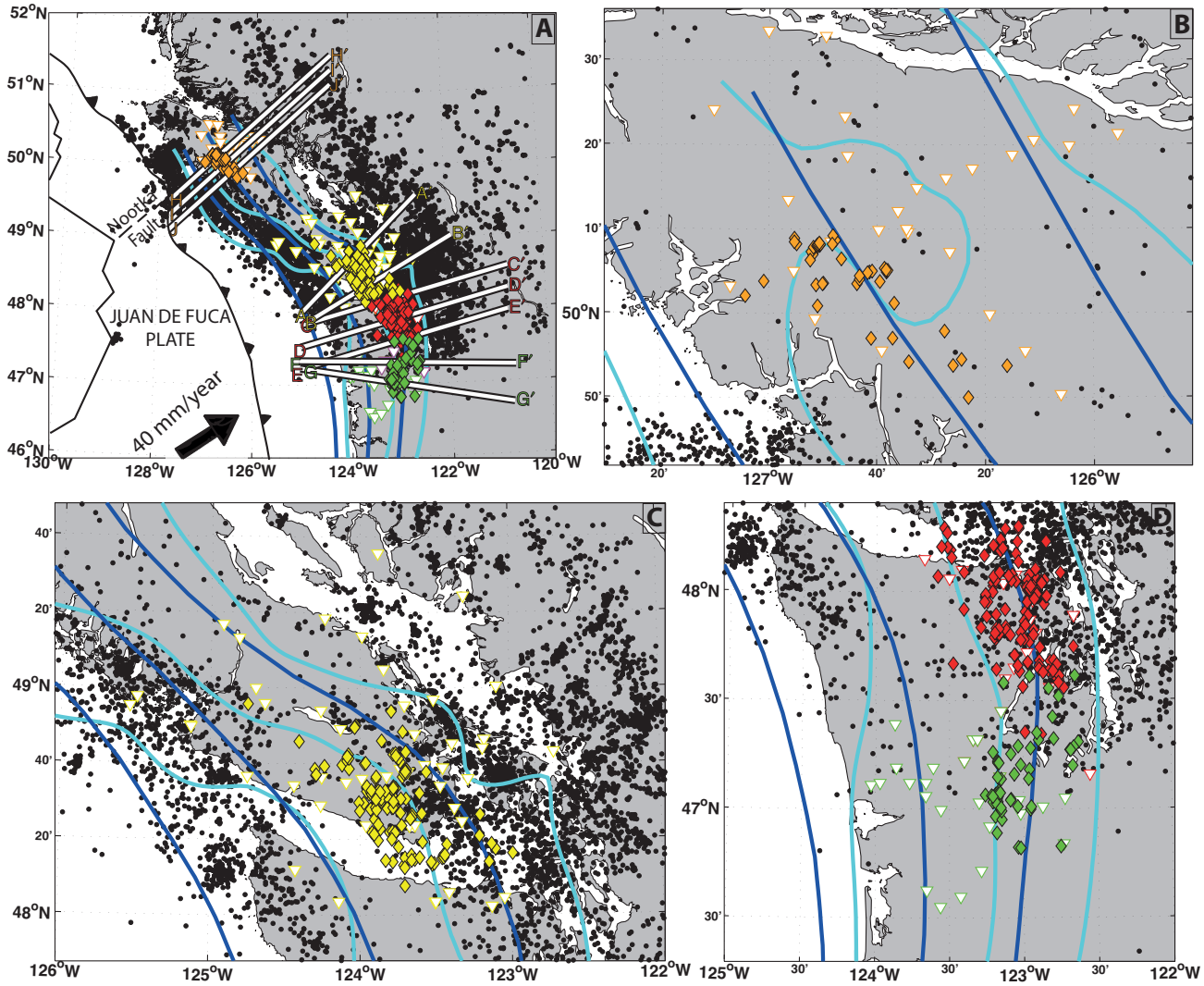

FIGURE 3.4: Maps of LFE locations computed using the Hyp2000 software organized as in figure 3.1. Orange, red and green diamonds are LFE locations from the NVI, NW and SW arrays, respectively. Yellow diamonds are locations of LFEs in southern Vancouver Island described by *Bostock et al.* [2012]. Cyan and blue lines indicate the 20, 30 and 40 km depth contours to the top of the subducting Juan de Fuca pate modelled by *Audet et al.* [2010] and *McCrory et al.* [2012], respectively. Black dots represent regular earthquake locations for the period 1985-2012.

LFE epicenters in northern Cascadia, shown in figures 3.4 and S1 fall within the general tremor epicenter distributions previously mapped by *Kao et al.* [2009, Figures 7,9] and *Wech et al.* [2009, Figures 1,3]. In the southern Vancouver Island (SVI) and Washington state (NW and SW) regions, LFE epicenters are bounded by the 25 and 38 km slab depth contours for the *Audet et al.* [2010] model and the 32 and 45 km contours for the *McCrory et al.* [2012] model. In northern Vancouver Island the LFE templates map close to the 30 km contour for both models. As noted by *Bostock et al.* [2012] for southern Vancouver Island LFEs and by *Kao et al.* [2005] for tremor more generally, LFEs epicenters tend to avoid regions with higher levels of regular seismicity, shown as black dots in figure 3.4 for the period 1985-2012.

Figure 3.5 plots the hypoDD locations of 10 depth profiles defined in figure 3.4 (analogous plots for the hyp2000 locations can be found in supplementary figure A2 in Appendix A). Note that A-A' and B-B' profiles below southern Vancouver Island were previously presented by *Bostock et al.* [2012]. Profiles are constructed using bins that extend ± 25 km to either side, and include the *Audet et al.* [2010] slab model quadratically interpolated through the 20,30 and 40 km contours and the *McCrory et al.* [2012] model linearly interpolated through 5 km depth intervals between 20 and 80 km. This figure further emphasizes the segregation of LFEs from regular earthquakes. LFEs tend to lie several km on average above intraplate earthquakes where their epicenters overlap. The two slab models bracket the LFE hypocenters below southern Vancouver Island and northern Washington (profiles A,B,C), the *Audet et al.* [2010] model from above and the *McCrory et al.* [2012] model from below. Hypocenters beneath SVI range between 29-40 km depth whereas those below Washington state fall between 31-46 km depth (NW) and 32-49 km depth (SW). Hypocenters along the SW profiles (E,F,G) coincide more closely with the *McCrory et al.* [2012] model, whereas hypocenters for LFEs for NVI profiles I,J are better aligned with the *Audet et al.* [2010] model where hypocenters fall between 33-39 km depth.

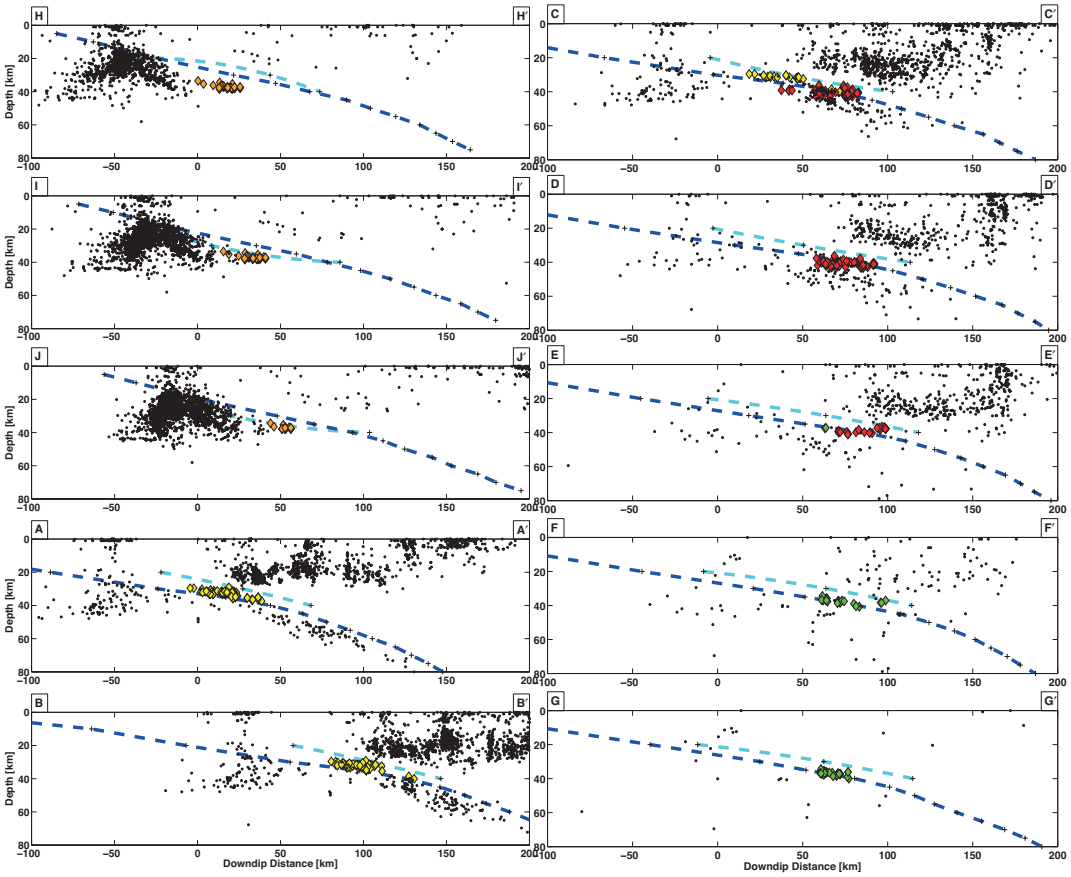

FIGURE 3.5: Depth profiles of seismicity in Vancouver Island and Washington state. Profile locations are identified in figure 3.4a. Black dots represent regular earthquake locations for the period 1985-2012. Orange, yellow, red and green diamonds are LFE template locations determined using hypDD for NVI, SVI, NW and SW arrays, respectively. Dashed cyan and blue lines represent depth estimates to the top of the subducting Juan de Fuca plate from *Audet et al.* [2010] and *McCrory et al.* [2012] models, respectively.

3.6 LFE template moment tensors

In our previous effort [*Bostock et al.*, 2012] to determine focal mechanisms of LFEs on southern Vancouver Island, we employed *P*-polarity estimates that were derived through correlation of vertical component seismograms with a reference pulse. That work suggested that LFE mechanisms comprised a mixture of thrust and strike slip faulting. We improve our analysis in the present study in several ways. First, 90° phase rotation of particle velocity seismograms provides a more robust means of producing zero-phase pulses and ascertaining the polarity of *P*- and *S*-arrivals at smaller epicentral distances than correlation with a reference pulse. Second, we have incorporated data from several previously unavailable stations along the southern coast of Vancouver

Island (CPLB,LCBC,JRBC,GLBC) that significantly improve coverage in the south-western quadrant. Finally, we now exploit the identification of the LFE templates with empirical Green's functions to perform a moment tensor inversion that, in addition to *P*-wave polarities, leverages constraints from *S*-wave polarities and relative amplitudes of both *P*- and *S*-waves.

Our moment tensor inversion procedure incorporates elements from *Kikuchi and Kanamori* [1991] and involves the following steps: i) each 3-component LFE template seismogram is normalized to unit, maximum absolute amplitude and phase rotated by 90° to aid in identication and picking of zero-phase, primary arrivals; ii) locations are determined from traveltime picks corresponding to those *P*- and *S*-arrivals judged to display unambiguous, zero-phase waveforms, iii) ray theoretic synthetic seismograms [*Cerveny et al.*, 1987] comprising direct *P*- and *S*-arrivals are generated for a basis of 6 independent moment tensors and normalized/phase rotated/filtered to match the spectral properties of the data; iv) synthetic and observed P and S waveforms are aligned based on their amplitude extrema to account for unmodelled velocity structure; v) least-squares inversion is performed for the coefficients of the moment tensor basis that best explain the relative amplitudes and polarities of the primary LFE arrivals; and vi) the best double couple mechanism is extracted from the general moment tensor solution using Newton optimization.

Figure 3.6 shows an example of the waveform matches derived for SVI template 005 with a double couple solution. The effect of a steeply inclined nodal plane roughly parallel to strike is evident in the change in *P*-wave polarity that occurs near station LZB on the vertical component and the large, negatively polarized *S*-arrivals on the north and east components at e.g., stations TWBB to PGC that straddle the plane. Best-fit double couple solutions are plotted in figure 3.7 for a geographically representative subset of SVI templates. SVI solutions are generally well modelled as double couple sources as indicated by F-tests that reveal no significant improvement in fit afforded by deviatoric or full moment tensor solutions. The majority of double couple solutions are characterized by thrust mechanisms oriented in a northeasterly direction, although there are two groupings of 3-4 LFE locations each near 48°12' N, 123°6' W and 48°42' N, 124°12' W that appear to show somewhat consistent strike-slip components.

In addition to the correct identification of wavelets on LFE templates as direct P and/or S, our ability to constrain the moment tensor depends on event-station geometry as quantified by the condition number of the normal equations. The extensive areal aperture of the NVI array and a localized distribution of LFEs near its center lead to condition numbers (mean=17, median=22 for the deviatoric solution, see supplementary figure A3 in Appendix A) that are less than those for SVI (mean=68, median=33), although this measure of solution quality does not account for the template SNR that is superior for SVI. Double couple solutions for the NVI templates (figure 3.8) like those for SVI tend to be shallow thrust in nature. The same characterization holds for the SW solutions (figure 3.9) with mean and median condition numbers of 17 and 27, respectively although there is greater variability in their orientation. In contrast, moment tensor solutions for NW templates (figure 3.10) are marked by large condition numbers (mean=366, median=89) that manifest the quasi-linear distribution of stations, and display still greater variability in orientation. Each of figures 3.7-3.10 contains an inset displaying the best double couple solution (*i.e.* with linear vector dipole component removed) determined from the average of individual double couple solutions for all templates within the respective subarray. The corresponding averaged plate motion vector determined from data in *McCaffrey et al.* [2007] is superposed on these plots. Supplementary figure A4 in Appendix A provides an alternative representation of the focal mechanism distributions as histograms of strike, rake and dip for the individual subarrays assuming that the nodal plane with shallower dip represents the fault plane.

3.7 Discussion and conclusions

Through the generation of LFE templates using data from EarthScope sources (Transportable array, PBO, FlexArray), POLARIS deployments and permanent networks (CNSN, PNSN), we have extended documentation of Cascadia LFEs from southern Vancouver Island south into Washington state and north to northern Vancouver Island. Not surprisingly, LFE epicenters in northern Cascadia fall within the tremor epicentral distributions previously mapped by, e.g. *Kao et al.* [2009], *Wech et al.* [2009],

and tend to avoid regions of denser, regular seismicity as reported previously for tremor [*Kao et al.*, 2005] and for LFEs below southern Vancouver Island [*Bostock et al.*, 2012]. In particular, LFEs typically define a surface several km above the upper envelope of intraplate earthquakes and several km below the lower envelope of overlying crustal seismicity where their epicenters overlap.

LFE hypocenters generally parallel but do not coincide precisely with either of two recent models for the plate boundary in Cascadia. In fact, the hypocenters frequently locate between the plate boundary estimates, lying below the *Audet et al.* [2010] model and above the *McCrory et al.* [2012] model. The two models are based on different assumptions and data sets, and both may be subject to bias. The *Audet et al.* [2010] model relies on the identification of the plate boundary with the top of a pronounced low-velocity zone (LVZ) that occurs throughout Cascadia and which has been most recently interpreted to be upper oceanic crust [*Bostock*, 2013, *Hansen et al.*, 2012]. This model was generated for the purposes of cross-Cascadia comparisons between the geometry of the LVZ and tremor epicentral distributions [e.g. *Wech and Creager*, 2011, figure 1]. It was derived using the timing of scattered teleseismic P-phases and the simplifying assumption of a homogeneous overriding plate with fixed P-velocity of 6.5 km/s but locally variable V_P/V_S ratio as opposed to the 1-D, fixed V_P/V_S model used for LFE location. The differences in underlying velocity models may result in depth biases that are locally significant.

The *McCrory et al.* [2012] model was constructed by synthesizing depth information from intraplate earthquake locations and regional seismic velocity profiles. The authors inferred the top of the Juan de Fuca slab to lie near the upper surface of intraplate seismicity where present, and weighted these seismicity constraints more highly than structural information derived from velocity profiles in areas where both sources of information were available. Plate boundary depth estimates based on this approach may be biassed deep by ~ 7 km if intraplate seismicity resides near the base of the subducting crust as has been inferred by *Shelly et al.* [2006] for southwest Japan. Comparison of hypocenters from southwest Japan with those from northern Cascadia [*Bostock et al.*, 2012, figure 8; see also figures 3.5,A2 herein] points to similar geometrical relations between LFEs, LVZs and intraplate seismicity, and implies that the structural controls

on seismogenesis in the two regions are the same.

The only region where the *Audet et al.* [2010] model maps the plate boundary to deeper levels than the *McCrory et al.* [2012] model, is along profiles I,J in northern Vancouver Island. In this region, the Explorer microplate is interpreted to be detaching from the Juan de Fuca plate along the Nootka fault and its NE landward extension [e.g *Audet et al.*, 2008, *Braunmiller and Nabelek*, 2002]. The majority of LFEs here lie along a relatively flat trajectory between 35-38 km depth coinciding with the *Audet et al.* [2010] model along profiles I,J, although they lie significantly deeper than that model on profile H immediately to the north. The LFE hypocenters are also slightly deeper than the 25-35 km depths quoted for tremor in this region by *Kao et al.* [2009].

We have outlined simple arguments justifying the identification of LFE templates with empirical Green's functions, thereby facilitating their treatment in waveform inversions for, *e.g.*, moment tensor solutions. Note that we do not mean to imply that all LFEs are characterized by single point-source, step displacements in time. Examination of individual LFEs detected via network correlation often does reveal impulsive, albeit noisy, signals resembling the template waveforms. Just as frequently, however, the signals display more complex temporal dependencies consistent, for example, with rapid tremor streaking that has been documented in northern Washington using beamforming techniques [*Ghosh et al.*, 2010].

Our examination of source mechanisms from the SVI subarray using moment tensor inversion improves on our analysis of *P*-wave polarities in *Bostock et al.* [2012] by including more stations from the previously poorly sampled southwestern quadrant, by employing *S*-wave polarities and relative amplitudes across individual station components, and by the use of a 90° phase rotation to facilitate phase identification within the bandlimited signals. SVI moment tensor solutions are generally well constrained and the large majority ($\sim 90\%$) of mechanisms are consistent with shallow thrust faulting in the direction of relative plate motion. The variability in focal mechanisms increases progressively through the NVI, SW and NW subarrays. We suspect that this variability may be due partly to poorer station coverage (for NW in particular) and partly to lower SNR resulting from smaller numbers of contributing detections. Diminished SNR renders it difficult to accurately isolate phases, especially *S*, within bandlimited data.

S is particularly problematic because, at larger epicentral distances, generation of post-critically reflected *P* at the free surface significantly distorts *S*-waveforms [*Booth and Crampin*, 1985] such that only the *SH* component retains its original source signature. In addition, strong anisotropy is known to occur in some areas [*Bostock and Christensen*, 2012] and may also contaminate waveforms through splitting. Notwithstanding variability in focal mechanism consistency across the different subarrays, the average double-couple solution for each (see insets in figures 3.7-3.10) is generally consistent with shallow thrusting in the direction of plate motion.

These subarray-averaged moment tensors and the preponderance of individual thrust mechanisms for the SVI, NVI (and to a lesser extent SW) subarrays approximately aligned with the plate motion direction leads us to suspect that shallow thrust faulting may prevail throughout the northern Cascadia region, as has been argued for SW Japan by *Ide et al.* [2012] and central Mexico by *Frank et al.* [2013]. In so doing, we interpret variability in focal mechanisms in figures 3.7-3.10 (for the NW array in particular) as due to variations in SNR and conditioning of the inverse problem. We acknowledge, however, the possibility that, locally, LFE mechanisms may depart from the shallow thrust orientation dependent, for example, upon structure in the downgoing plate. The likelihood that a majority of, if not all, LFE mechanisms are shallow thrust would weaken the argument by *Bostock et al.* [2012] that LFEs are distributed through a plate boundary shear zone coinciding with the (3-4 km thick) LVZ. Although our nominal depth location uncertainties ($\sim \pm 2$ km) do not allow us to address this issue directly, recent work by *Nowack and Bostock* [2013] employing scattered waves from a selection of templates requires LFEs to occur < 1 km below the top of the LVZ. This constraint together with the moment tensor results presented here are consistent with an origin for LFEs as shear slip along a relatively sharp plate boundary atop the LVZ.

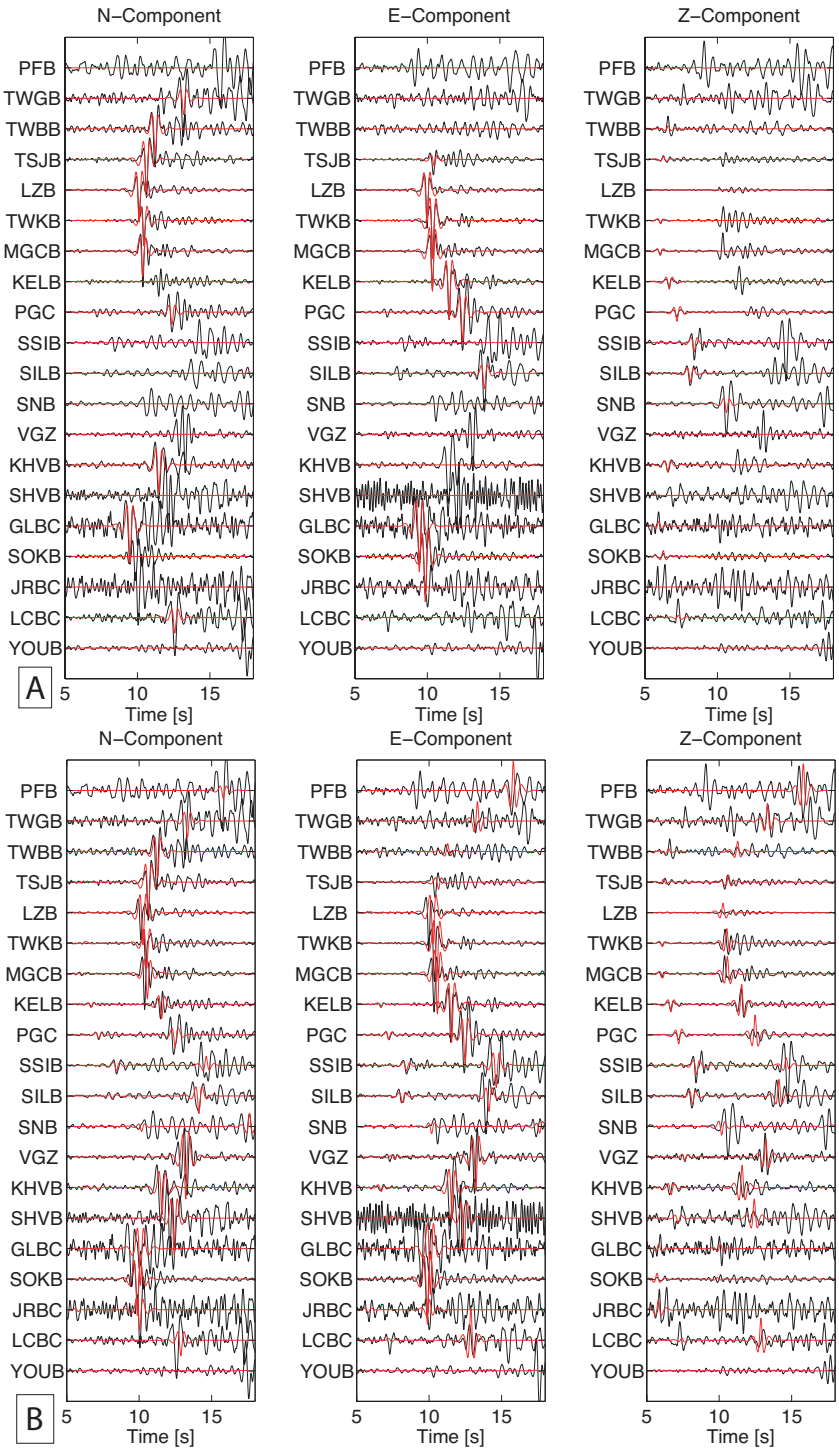

FIGURE 3.6: Example of waveform matching in moment tensor inversion for SVI template 005. a) Modelled data. Synthetics (red) are superimposed on data (black) for those channels selected for fitting; zero amplitude synthetic traces correspond to unused channels. *S*-waves are fit to horizontal components and *P*-waves to the vertical component with shifts up to ±0.2 s applied to maximize correlation. b) Synthetic seismograms for full station complement corresponding to double couple solution derived from selected channels in a). Timing misalignments result from errors in velocity model used to generate synthetics.

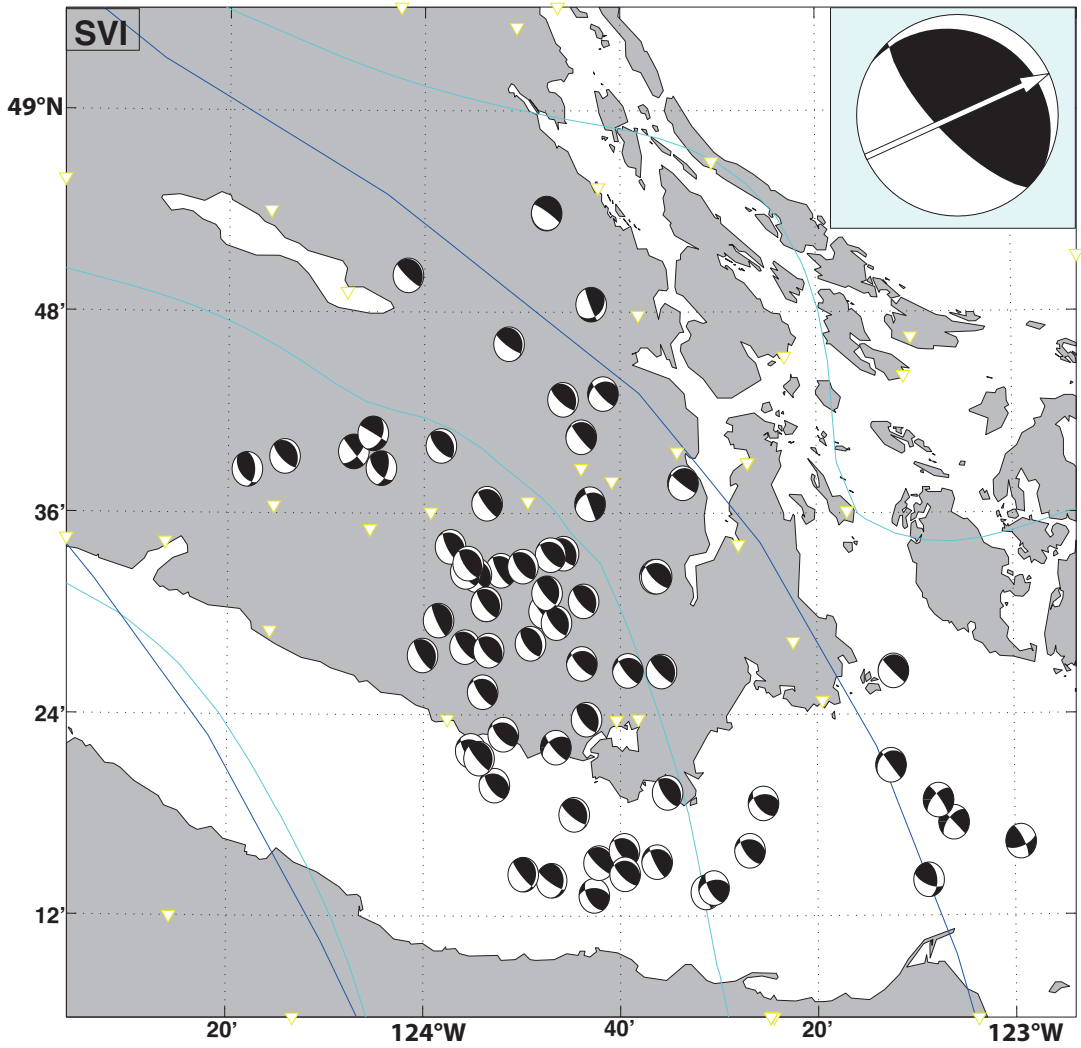

FIGURE 3.7: Map of double couple mechanisms determined from moment tensor inversion of a selection of LFE templates from the SVI subarray. Inset shows best double couple mechanism from average over all individual moment tensors with arrow indicating corresponding averaged plate motion direction [*McCaffrey et al.*, 2007].

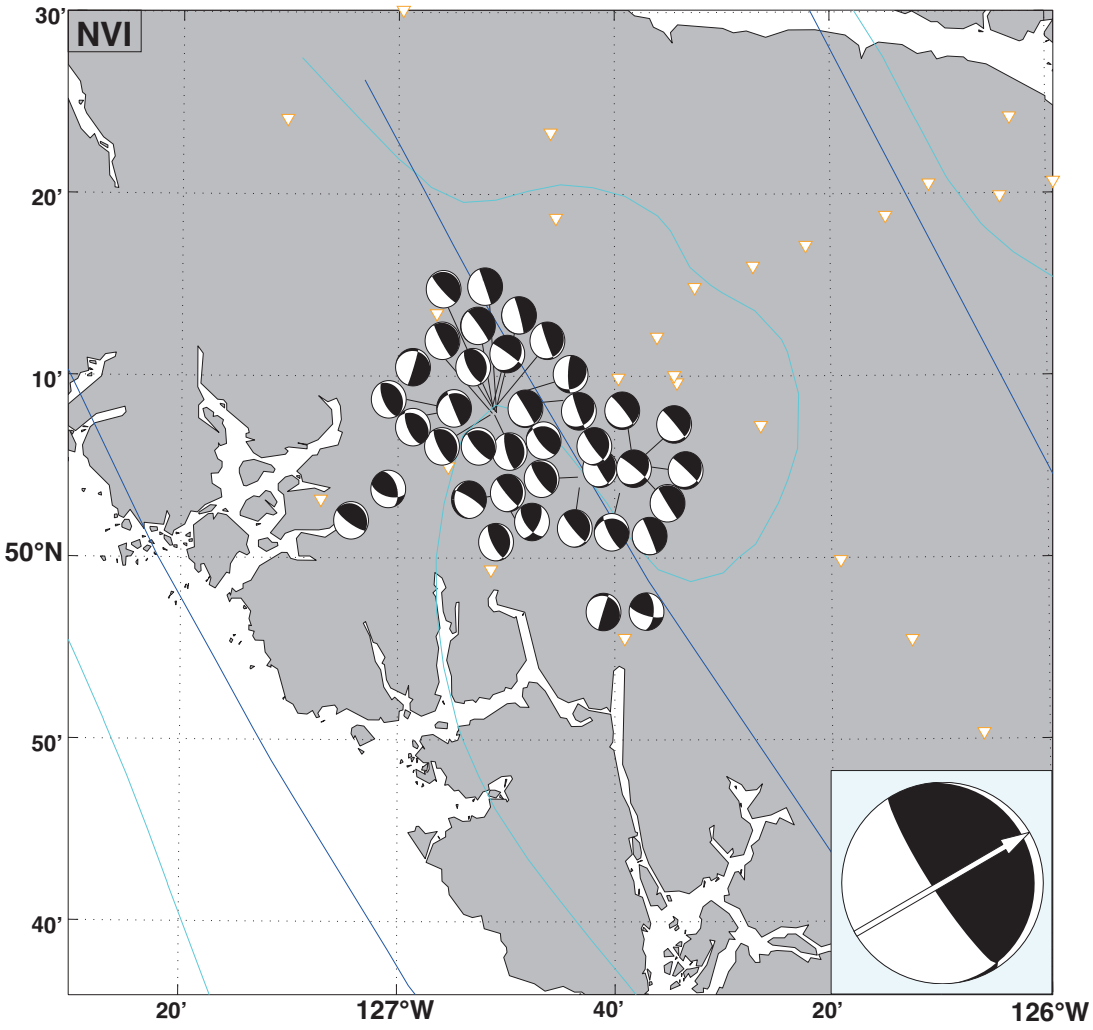

FIGURE 3.8: Map of double couple mechanisms for NVI subarray; see caption of figure 3.7 for explanation.

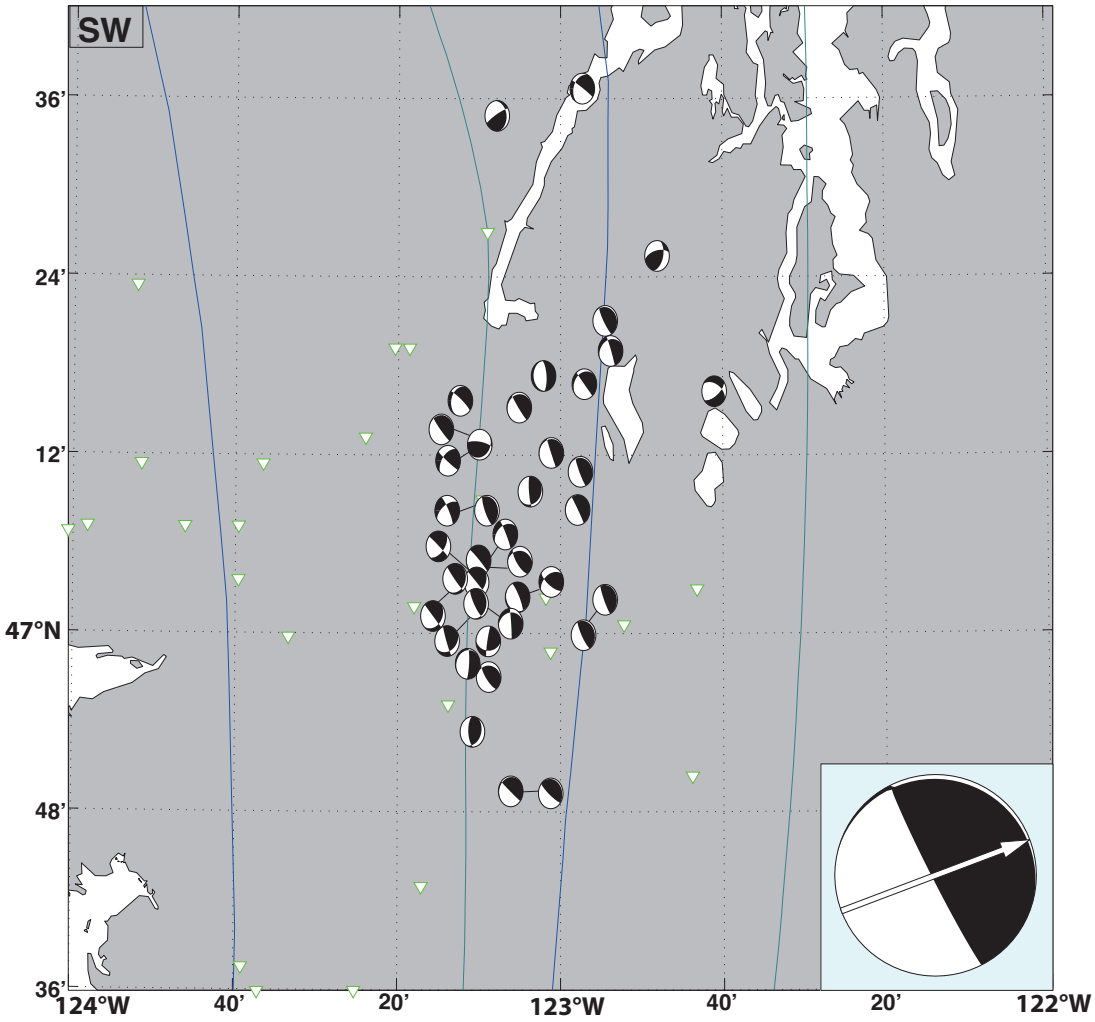

FIGURE 3.9: Map of double couple mechanisms for SW subarray; see caption of Figure 3.7 for explanation.

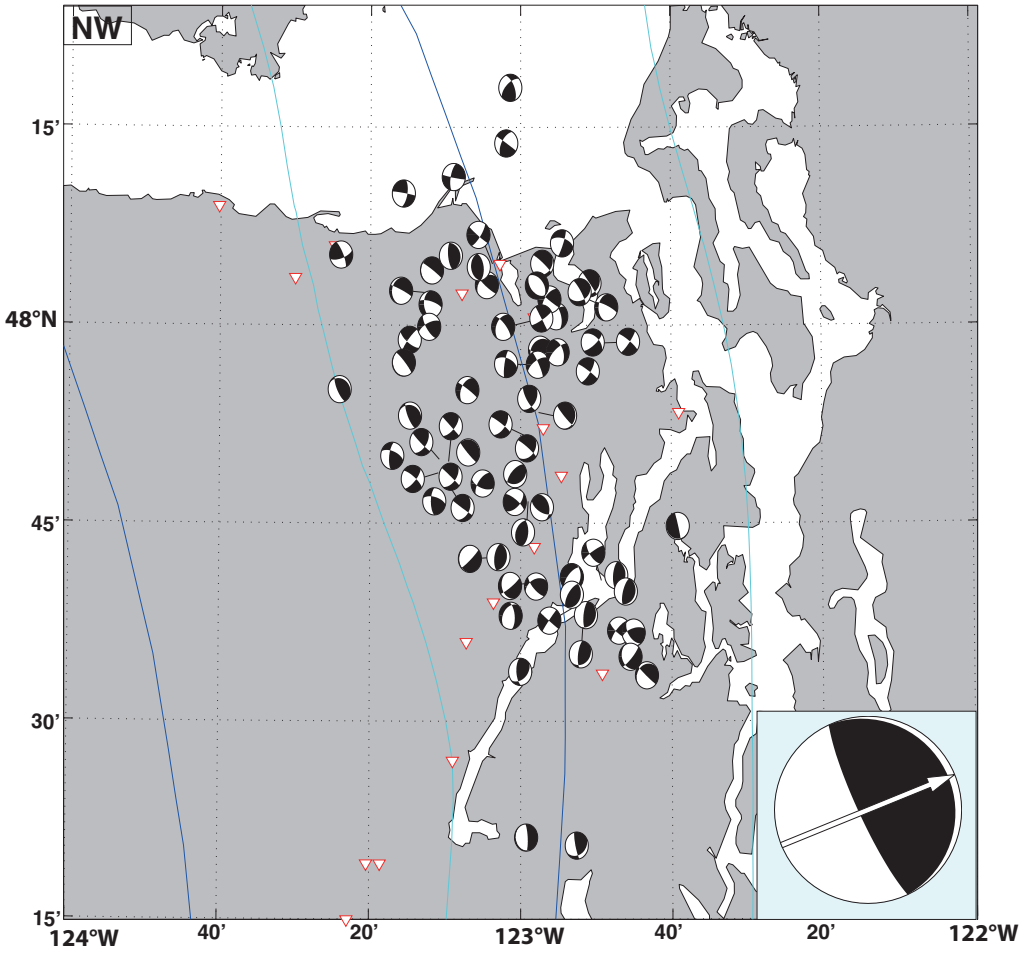

FIGURE 3.10: Map of double couple mechanisms for NW subarray; see caption of figure 3.7 for explanation.

Chapter 4

Tidal modulation of low frequency earthquakes and triggering of secondary events in northern Cascadia

4.1 Introduction

It has become increasingly evident in recent years that slow slip, tectonic tremor and LFEs are sensitive to small stress changes. Perturbations at levels of several 10's of kPa, as generated by surface wave trains from teleseismic events, are capable of triggering tremor [*Miyazawa and Mori*, 2005, *Peng and Chao*, 2008, *Peng et al.*, 2008, *Rubinstein et al.*, 2007, 2009] whereas tidal stresses at levels <10 kPa have been shown to modulate slip [*Hawthorne and Rubin*, 2010, 2013], tectonic tremor [*Gallego et al.*, 2013, *Klaus*, 2012, *Lambert et al.*, 2009, *Nakata et al.*, 2008, *Rubinstein et al.*, 2008, *Thomas et al.*, 2013] and LFEs [*Shelly et al.*, 2007, *Thomas et al.*, 2012] during periods of tremor and associated slip. The analysis of tidal modulation, in particular, has led to important insights into the mechanism underlying the phenomena.

The first report of tidal modulation of tectonic tremor in northern Cascadia was made by *Rubinstein et al.* [2008] who identified clear pulsing of tremor activity with

periods of 12.4 and 24 to 25 hours, corresponding to the principal lunar (M2) and lunisolar tides. A study of tremor below southern Vancouver Island by *Lambert et al.* [2009] demonstrated that peak tremor activity occurs at times of maximum tidal shear stress in the thrust direction suggesting that tidal tremor and slip are collocated. Similar modulation of tremor by tidal shear stress has been observed in southwest Japan beneath Shikoku [*Ide*, 2010, *Nakata et al.*, 2008] and northern Washington [*Klaus*, 2012]. To better understand the influence of tidal stresses on slow slip, *Hawthorne and Rubin* [2010] analyzed strainmeter records from northern Washington and southern Vancouver Island for episodic tremor and slip (ETS) events between 2007 and 2009. They observed tidal modulation of slow slip-induced strain at the 12.4h M2 period compatible with peak strain rate occurring somewhere between time of maximum shear stressing rate and maximum shear stress, depending on slip location. *Hawthorne and Rubin* [2013] used a velocity weakening-to-strengthening friction law to model slow slip events in the presence of periodic shear stress to simulate the tides. Their simulations produced quasi-sinusoidal tidal modulation of the slip rate, with the maximum moment rate occurring close to the maximum applied stress. *Thomas et al.* [2013] noted that large, high-amplitude rapid tremor reversals (RTRs, *Houston et al.* [2011]) and tremor streaks in northern Washington occur almost exclusively during times of positive, thrust-encouraging tidal shear stress on the plate interface, leading them to suggest that tidal stresses could trigger or intensify large, high-amplitude RTRs that propagate in reverse into previously ruptured and weakened zones on the fault. *Beeler et al.* [2013] used observations of LFE sensitivity to tidal stressing on the San Andreas fault to constrain fault rheology. They assumed LFEs are generated on small patches that fail at a threshold stress on an otherwise creeping fault plane. These seismic patches are loaded tectonically, directly by the tides and also by time-dependent creep of the surrounding fault. The authors' analysis dismissed dislocation creep and dislocation glide as too strong to be mechanisms for fault creep where LFEs occur, although rate dependent friction is permitted if effective normal stresses are low, implying near-lithostatic pore pressures. Observations of high V_P/V_S ratios in the LFE source region in Cascadia [*Audet et al.*, 2009] and southwest Japan [*Shelly et al.*, 2006] supply supporting evidence for near-lithostatic pore pressures in the subduction zone setting.

The aforementioned studies clearly establish that slow slip and tremor are modulated by tidal forcing. In this paper, we analyze the sensitivity of LFEs to tidal forces using three LFE detection catalogues for northern Cascadia, beneath southern Vancouver Island and Washington state. LFE catalogues determined using network correlation hold advantages over tremor in that the LFE source locations and their temporal recurrence are more precisely defined, enabling detailed studies of spatio-temporal variability on discrete fault patches [*Shelly et al.*, 2007, *Thomas et al.*, 2012]. Following the methodology proposed by *Thomas et al.* [2012], we quantify the correlation of our LFE families with tidal stresses, analyze the phase of LFE failure time relative to tidal load, compute the sensitivity to tidal shear stress as a function of time into an ETS event and the sensitivity of LFEs near the leading edge of slip versus that of RTRs. We compare results with previous work in Cascadia, Parkfield and Shikoku and discuss the implications of these observations for plate boundary properties.

4.2 Data

We employ three distinct LFE detection catalogues in northern Cascadia. The first LFE catalogue, assembled by *Bostock et al.* [2012] for southern Vancouver Island (SVI), was culled to 93 geographically independent LFE families with a total of 148,847 detections from ETS episodes between 2003-2013. The two other LFE catalogues were assembled by *Royer and Bostock* [2013] for Washington state (see Chapter 3). The northern Washington (NW) catalogue was regrouped into 100 geographically independent LFE families and includes a total of 60,527 detections from ETS episodes between 2007-2011. LFE locations for this catalogue span the eastern flanks of the Olympic Peninsula to the western reaches of Puget Sound. The southern Washington (SW) catalogue, regrouped into 49 geographically independent LFE families, includes a total of 22,868 detections from ETS episodes during the period 2007-2008, from a region to the southwest of Puget Sound. Figure 4.1 shows LFE family locations for the three different catalogues. LFE detection methodology, location procedure, depth profiles and focal mechanisms for the 3 catalogues are presented in *Bostock et al.* [2012] and in Chapter 3 [*Royer and Bostock*, 2013] .

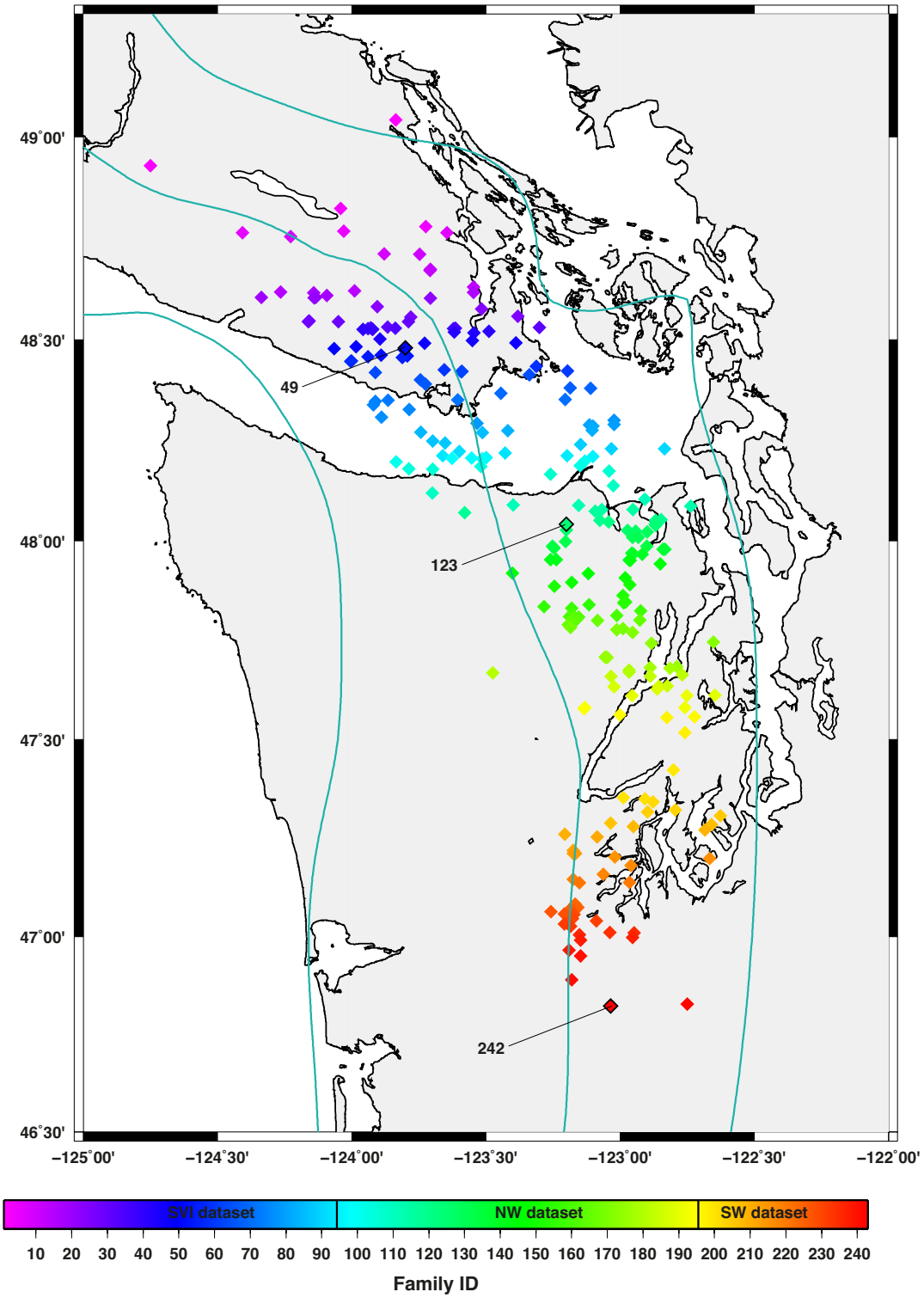

FIGURE 4.1: Map of LFE family locations in southern Vancouver Island (SVI detection catalogue) and Washington State (NW and SW detection catalogues) assembled by *Bostock et al.* [2012] and *Royer and Bostock* [2013] (see Chapter 3), respectively. Cyan lines indicate the 20, 30 and 40 km depth contours to the top of the subducting Juan de Fuca plate modeled by *Audet et al.* [2010]. Color bar legend indicates LFE family IDs ordered by latitude, from north to south and the subdivision of the 3 detection catalogues is shown by black vertical lines. The three numbered families are used in plots of figure 4.2.

4.3 Methodology

4.3.1 Tidal model

We compute time series of tidal stress using SPOTL [*Agnew*, 2012]. The currently distributed version of SPOTL calculates horizontal and shear strains from the solid Earth and load tides at the Earth's surface. To compute strain at depth on a dipping fault requires two modifications. First, we use the Boussinesq solution for a point load on a half space to compute depth-dependent Green's functions for the load tide calculations. These Green's functions are calculated using a rigidity of μ =30 GPa and Poisson's ratio, ν=0.25 [*Farrell*, 1972, *Melchior*, 1978]. Second, we assume that the strains from the body tides do not vary substantially over the depth range of interest and are approximately equal to those at the surface. Assuming that shear stresses are zero at the Earth's surface, the vertical strain can be expressed in terms of the two horizontal strains as:

$$e_{rr} = \frac{-\nu}{1-\nu}[e_{\theta\theta} + e_{\lambda\lambda}]. \tag{4.1}$$

We compute tidally induced fault-normal and up-dip shear stresses, FNS and UDSS, and their time derivatives dFNS and dUDSS, using stress tensor time series and estimates of dip and dip azimuth of the subducting Juan de Fuca plate based on a smoothed version of the model of *Audet et al.* [2010]. Positive FNS indicates extension and positive UDSS refers to thrust-promoting shear stress in the up-dip direction. These 4 tidal time series are computed at sample intervals of 15 minutes for each tremor episode in the period 2003-2013. Figure 4.2 shows an example of tidal time series FNS and UDSS for LFE families 49 (SVI), 123 (NW) and 242 (SW) (see figure 4.1 for locations). Figure 4.3 maps the time-averaged envelope amplitude of stress of each LFE family for the 4 tidal components, computed as the magnitude of the analytic tidal signal over the corresponding detection period. Envelope amplitudes for UDSS and dUDSS increase from south to north, ranging from 481 Pa to 2276 Pa for UDSS, and between 2.6 Pa/min and 17 Pa/min for dUDSS. In contrast, envelope amplitudes for FNS and dFNS are larger beneath the Strait of Juan de Fuca, where the ocean load tides have a stronger

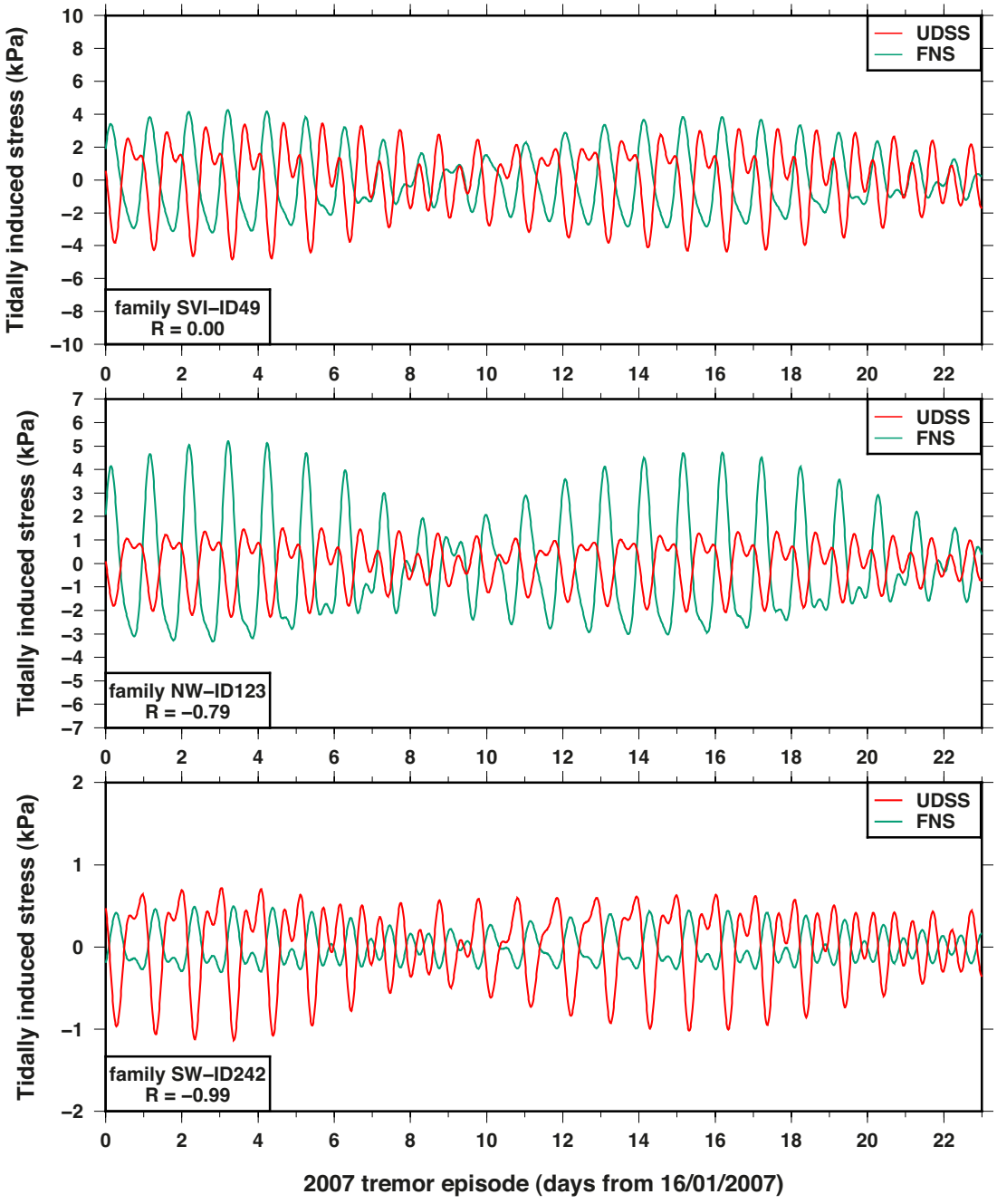

FIGURE 4.2: 2007 tremor episode time series of tidally-induced UDSS (red) and FNS (green) for LFE family 49 from the SVI detection catalogue (upper panel), LFE family 123 from the NW detection catalogue (middle panel) and LFE family 242 from the SW detection catalogue (bottom panel). The correlation coefficient R between FNS and UDSS for the given family is indicated in each panel.

influence. The amplitudes vary between 95 Pa and 5293 Pa for FNS, and between 0.42 Pa/min and 26 Pa/min for dFNS.

For 50% of the LFE locations, FNS and UDSS time series are anticorrelated with a coefficient correlation lower than -0.5. We may explain this negative correlation between FNS and UDSS by considering the relative contributions from different tidal components. The ocean load tides exert a stronger influence on the stresses in the tremor zone of northern Cascadia than the body tides by a factor that ranges from 2 to 10. This load tide influence can be divided into 3 components: the long wavelength load on the oceanic plate seaward of the trench, loading on the continental slope and shelf, and the load contribution from the inland seas, namely Georgia Strait and Puget Sound. The first contribution is the least important on account of its distance (the trench lies some 100 km southwest of the coast). As explained by *Lambert et al.* [2009], the two latter contributions are nearly opposite in phase and so contribute constructively to UDSS and destructively to FNS on that portion of the plate boundary where ETS occurs (roughly midway between the two water bodies). The offshore coastal load produces oppositely signed UDSS and FNS on the plate boundary and outweighs the contribution from the inland seas, with the result that FNS and UDSS are anticorrelated. In contrast, LFE locations beneath the Strait of Juan de Fuca (roughly 25% of the total) display the largest FNS envelope due to the additional load contribution from the Strait of Juan de Fuca resulting in weaker correlation between FNS and UDSS.

4.3.2 LFE correlation with tidal stress

For each LFE family location, we compute the tidally induced stresses and their derivatives at times corresponding to detections and compute the expected number of detections based on the amount of time spent in a particular loading condition (first relative to the sign of tidally induced stresses and stress rates, and later to the stress-magnitude range), assuming that LFE detections occur randomly in a given tremor episode. We quantify the degree of correlation of LFE occurrence with tidal stress by computing the excess value:

$$N_{ex} = \frac{\#\text{ observed detections} - \#\text{ expected detections}}{\#\text{ expected detections}}. \tag{4.2}$$

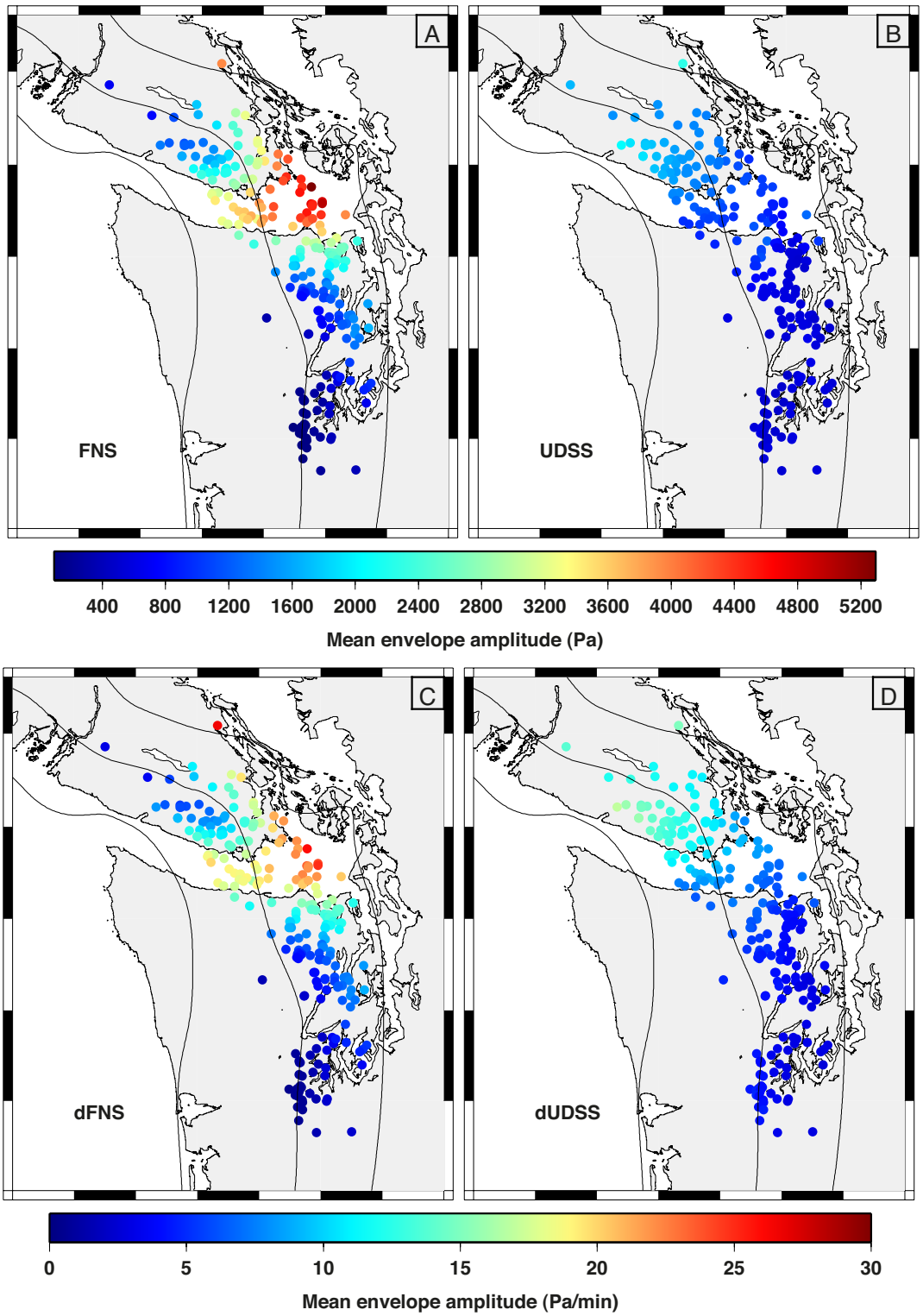

FIGURE 4.3: Map of tidal stress amplitudes. Mean tidal envelope amplitudes over detection time intervals are plotted color coded at locations of LFE families: FNS (panel A), UDSS (panel B), dFNS (panel C) and dUDSS(panel D) time series.

Positive N_{ex} values indicate a surplus of detections in the loading condition considered, and negative N_{ex} values indicate a deficit of detections. We include 95% and 99% confidence intervals by generating 25,000 random catalogues of N detections each (the number N varies with the LFE family considered, between 386 and 3575 for SVI, between 141 and 1942 for NW, and between 204 and 895 for SW) to compute a distribution of N_{ex} values. N_{ex} values that fall outside the 99% confidence interval are less than 1% likely to occur randomly assuming that tides and LFEs are uncorrelated. Figure 4.4 shows a map of LFE family locations, color coded by N_{ex} values corresponding to the 4 tidal components. We plot in figure 4.5 all possible combinations of N_{ex} values against each other. We analyze correlation between N_{ex} values and the mean stress envelope amplitudes by plotting them against each other for each tidal component, as shown in figure 4.6.

We consider how specific stress levels influence LFE occurrence by computing LFE rates as a function of the magnitude of the applied stress components. We determine the observed number of LFE detections for a particular family that falls within a given stress range (40 bins over the total stress range, set independently for each of FNS, UDSS, dFNS and dUDSS time series). The expected number of detections in each bin is then computed based on the null hypothesis that LFE origin times and tides are uncorrelated. The ratio

$$\frac{\#\text{ observed detections}}{\#\text{ expected detections}} = N_{ex} + 1, \tag{4.3}$$

is computed for each bin for a given stress component and for all families. Ratios greater than one translate to a surplus of detections and ratios lower than 1 indicate a deficit of detections compared to a random detection distribution. Results are plotted in figure 4.7.

We assign an effective phase angle to each LFE detection of a particular family using a method similar to that of *Tanaka et al.* [2002]. For each of the two pairs of components UDSS, dUDSS and FNS, dFNS, the maximum and the minimum tidal stresses are assigned to 0° and $\pm 180^\circ$, respectively. However, in contrast to the method of *Tanaka et al.* [2002], the maximum and minimum tidal stress rates are assigned

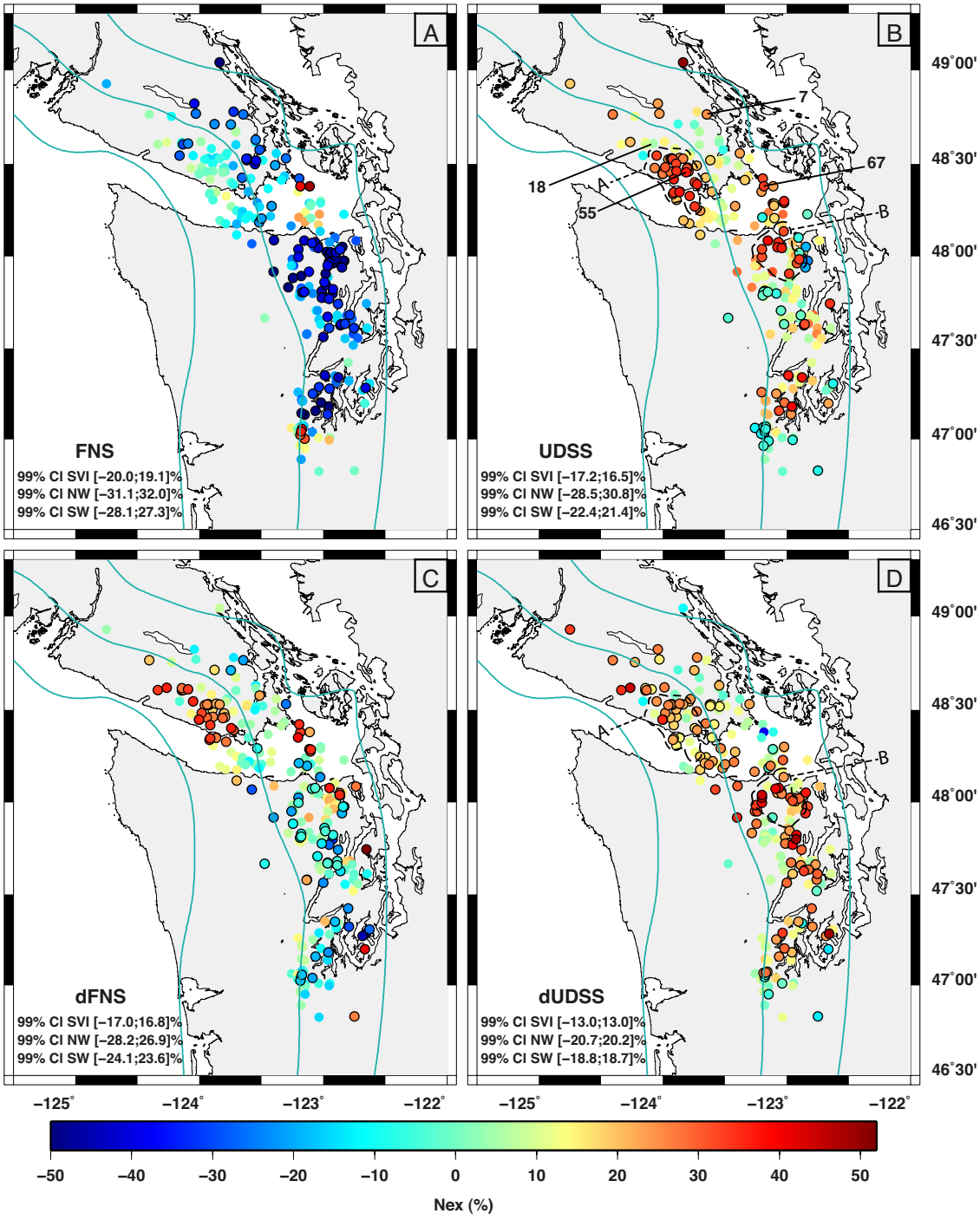

FIGURE 4.4: Map of N_{ex} values relative to the positive sign of tidally induced stresses and stress rates. LFEs are color-coded by N_{ex} values corresponding to the tidal FNS (panel A), UDSS (panel B), dFNS (panel C) and dUDSS(panel D) components. 99% confidence intervals (CI) calculated for the family with the fewest detections are given in the bottom left of each panel for each detection catalogue and significant families are indicated with black rims. The three numbered families in panel B are used in the recurrence analysis (section 4.5.3).

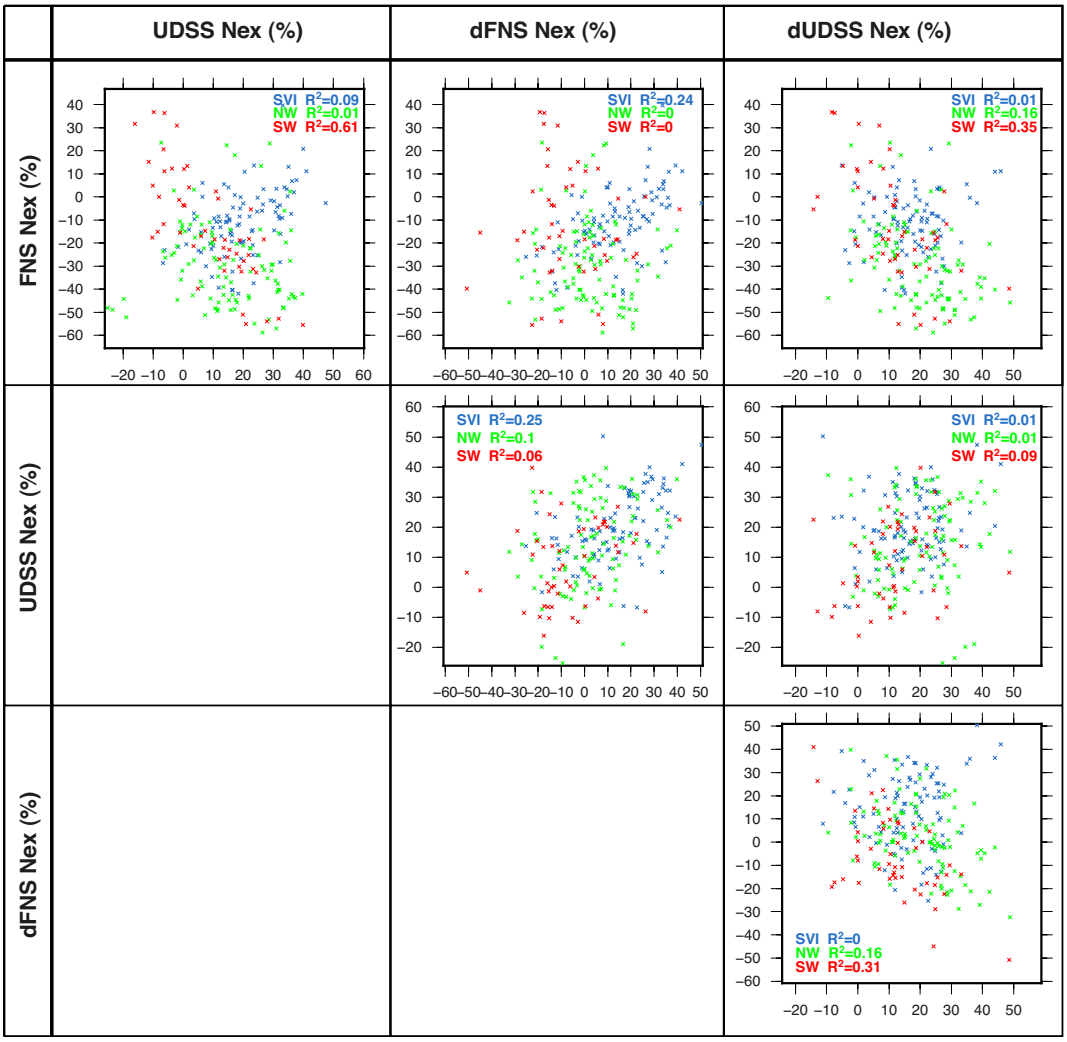

FIGURE 4.5: N_{ex} values relative to the positive sign of tidally induced stresses and stress rates are plotted against each other, for SVI (blue), NW (green) and SW (red) detection catalogues. A coefficient of determination R^2 (in this case the square of the sample correlation coefficient) is provided in each panel for the 3 detection catalogues, distinguished by different colors (blue - SVI, green - NW, red - SW). High values of R^2 indicate a strong correlation or anticorrelation between two components.

to 90° and -90°, respectively, increasing the accuracy of our assigned effective phases. The effective phase is assigned by interpolating the time of the event between times with assigned phases. We assemble the observed numbers of detections that fall within a phase angle range (here we consider 36 bins of 10°), and the expected numbers of detections in each bin are computed based on the null hypothesis that LFEs and tides are randomly correlated. We compute again the ratio $N_{ex} + 1$ for each bin of a given component pair (FNS,dFNS and UDSS,dUDSS) and for all families. Rose histograms of phases for the 3 different LFE detection catalogues are plotted in figure 4.8. A schematic phase plot with labeling is provided to aid in understanding the rose histograms. Bins

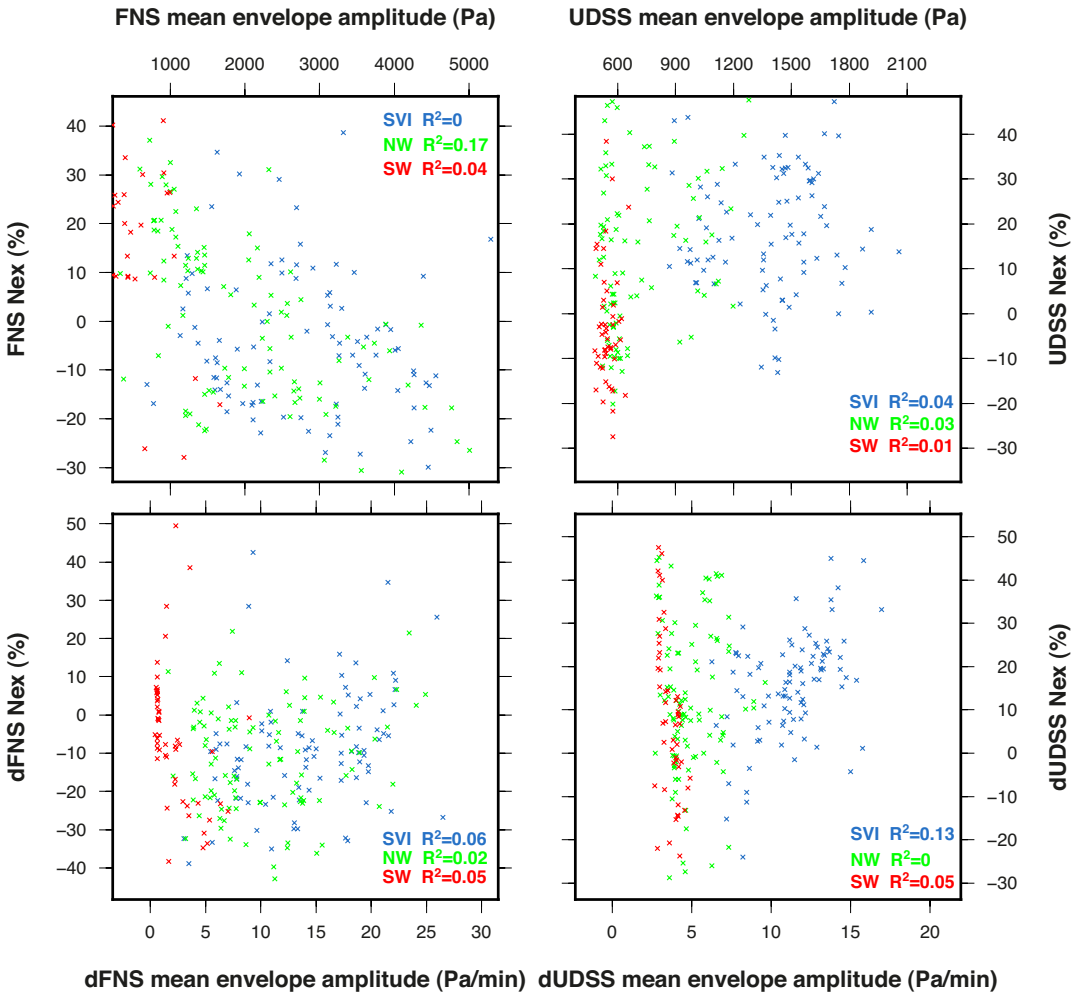

FIGURE 4.6: N_{ex} values relative to the positive sign of tidally induced stresses and stress rates plotted against the mean envelope amplitude, for each tidal component FNS (top -left), UDSS (top-right), dFNS (bottom-left) and dUDSS (bottom-right) and for detection catalogues SVI (blue), NW (green) and SW (red). A coefficient of determination R^2 (in this case the square of the sample correlation coefficient) is provided in each panel for the 3 detection catalogues, distinguished by different colors (blue - SVI, green - NW, red - SW).

that contain the expected number of detections have a radius of 1 (100% of the expected values assuming a random distribution shown by red contour). Confidence intervals corresponding to the 95% and 99% levels are also provided on each polar histogram (blue contours).

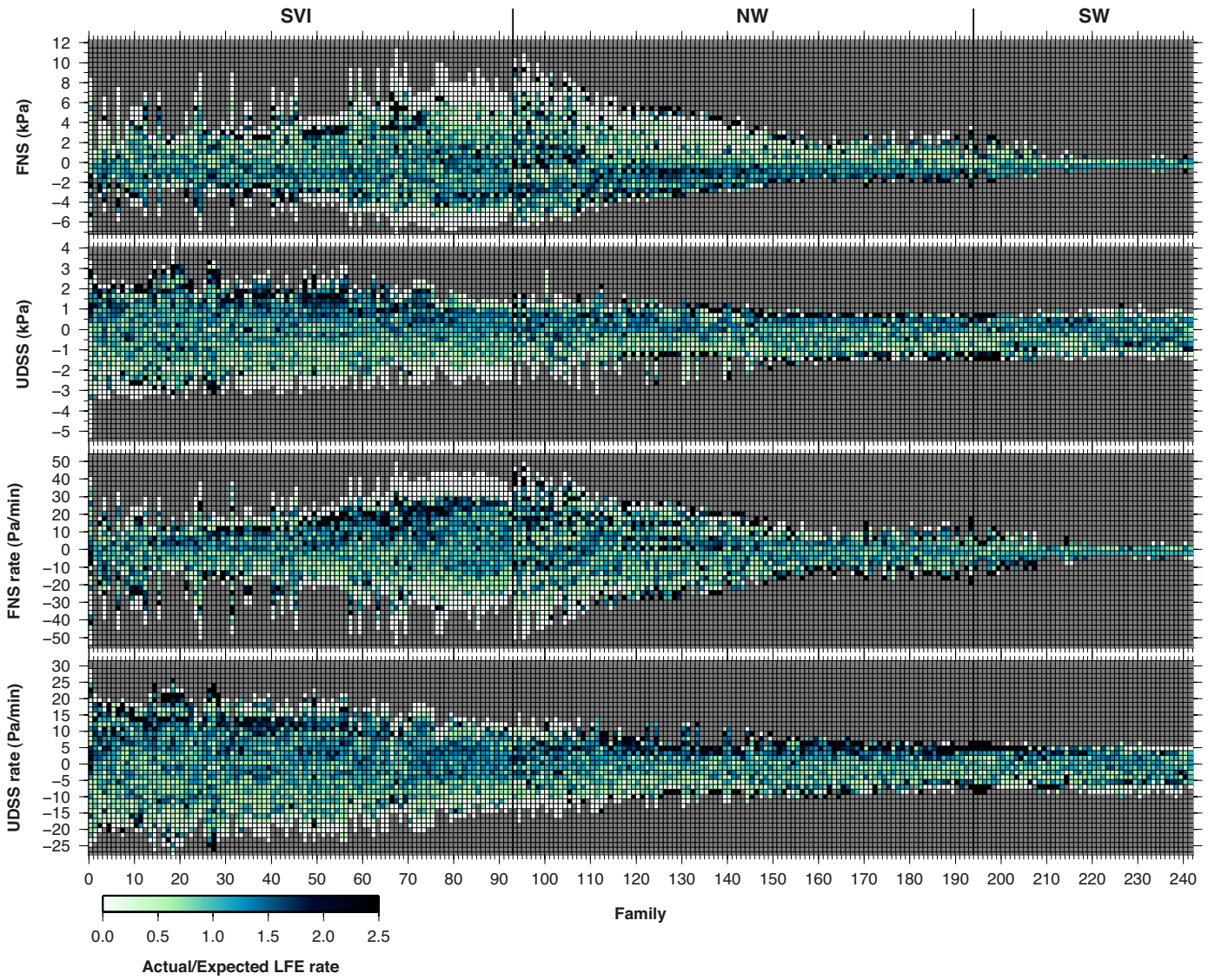

FIGURE 4.7: LFE rate plots as a function of the magnitude of the FNS (top), UDSS (middle top), dFNS (middle bottom) and dUDSS(bottom) components. Each column corresponds to an individual LFE family (ordered from north to south, all detection catalogues combined - subdivision shown by black vertical lines) and each row corresponds to a stress interval. The ratio of observed/expected number of LFE detections within a stress range is color-coded with warm colors (surplus of LFE detections, ratio greater than 1) and cold colors (deficit of LFE detections, ratio lower than 1) as shown on the color-bar legend.

4.3.3 Time dependent tidal sensitivity

Lambert et al. [2009] (figure 3 in their paper) commented that the response of Vancouver Island tremor detections to tidal stress varies through a tremor episode increasing from near zero to a finite level before falling back to zero. *Thomas et al.* [2012] observed that deep LFE families on the San Andreas fault that occur continuously generally had greater tidal sensitivity than shallower, episodic families. They interpreted the episodic families as having larger background slip rates than the continuous ones and suggested that the magnitude of tidal correlation decreases during strongly accelerated fault slip. Heidi Houston (pers. comm.) has also noted that Washington tremor detections [*Wech and Creager*, 2008] show variable tidal sensitivity over time within a given ETS episode. Here we investigate this dependence using our LFE catalogues. Most LFE families, independent of the ETS episode considered, display a steep increase in cumulative detections over the first day or two that levels off gradually thereafter. *Rubin and Armbruster* [2013] report similar behavior in their study of LFEs in Vancouver Island and note that the LFE detection rate starts high and gradually decays over the course of a few days, becoming increasingly intermittent. We subjectively define the beginning of LFE activity for a particular LFE family as the onset of the steep slope of their corresponding cumulative distributions. The percent excess value N_{ex} for the positive UDSS loading condition is computed for each of the 8 days following the beginning of activity. Figure 4.9 displays UDSS N_{ex} histograms (green bars) assembled for all families and all years (left panels), for subgroups of LFEs with high N_{ex} (regions A and B, N_{ex} >30% - middle panels - see section 4.4) and for subgroups of LFEs with low N_{ex} values (N_{ex} <10% right panels) for the SVI and NW regional catalogues. Confidence intervals at the 95% and 99% levels are indicated by the blue and red bars, respectively, and are determined by generating 25,000 random catalogues of M detections each (the number M corresponds to the number of detections contributing to each 1-day interval) to compute a distribution of N_{ex} values. Superimposed on the histograms are the percent cumulative distribution of LFE detections (blue curve) with the number of detections contributing to each 1 day-interval indicated at the bottom of each panel.

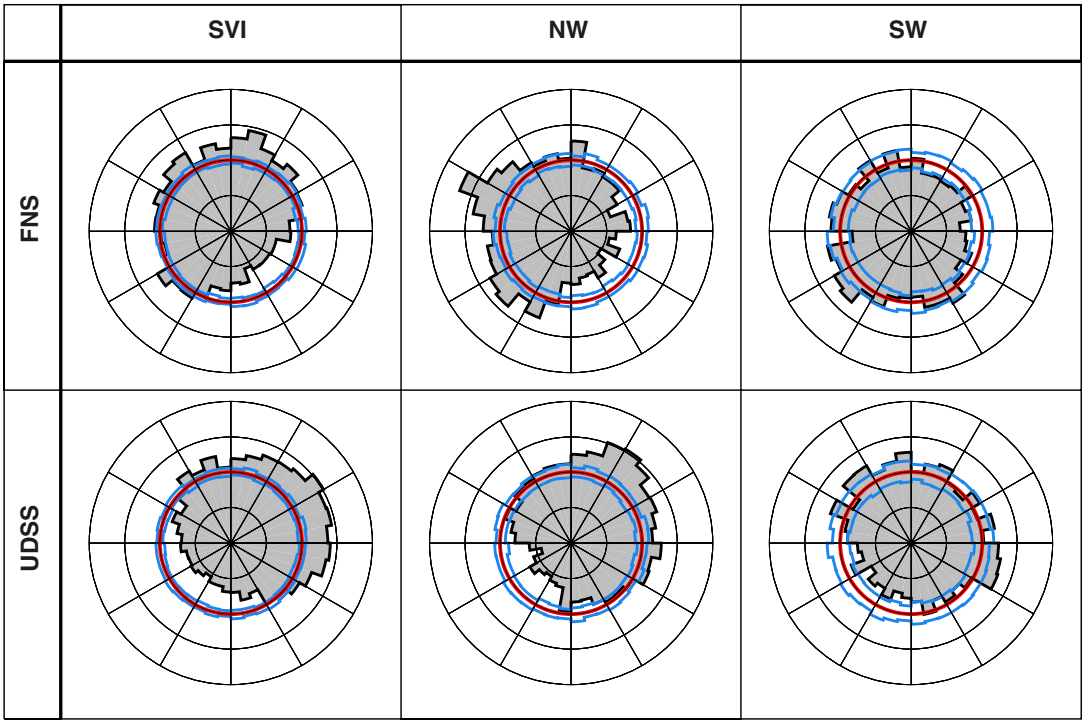

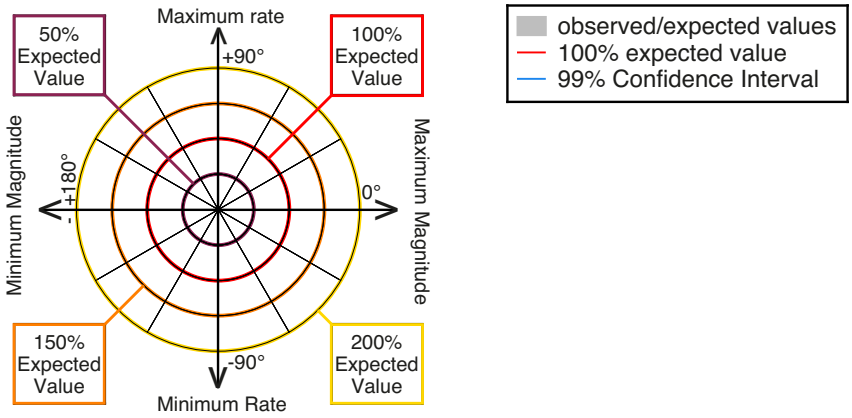

FIGURE 4.8: Bottom: schematic phase plot labeling the 50%, 100%, 150% and 200% expected values contours. Top: phase histograms. FNS (up) and UDSS (bottom) phase plots for a stack of all detections from SVI (left), NW (middle) and SW (right) detection catalogues. Gray shaded areas indicate ratio of observed over expected number of detections in each 10 degrees phase bin. Blue lines are the lower and upper limits of the 99% confidence Intervals for each bin. Red lines are the 100% expected values contours.

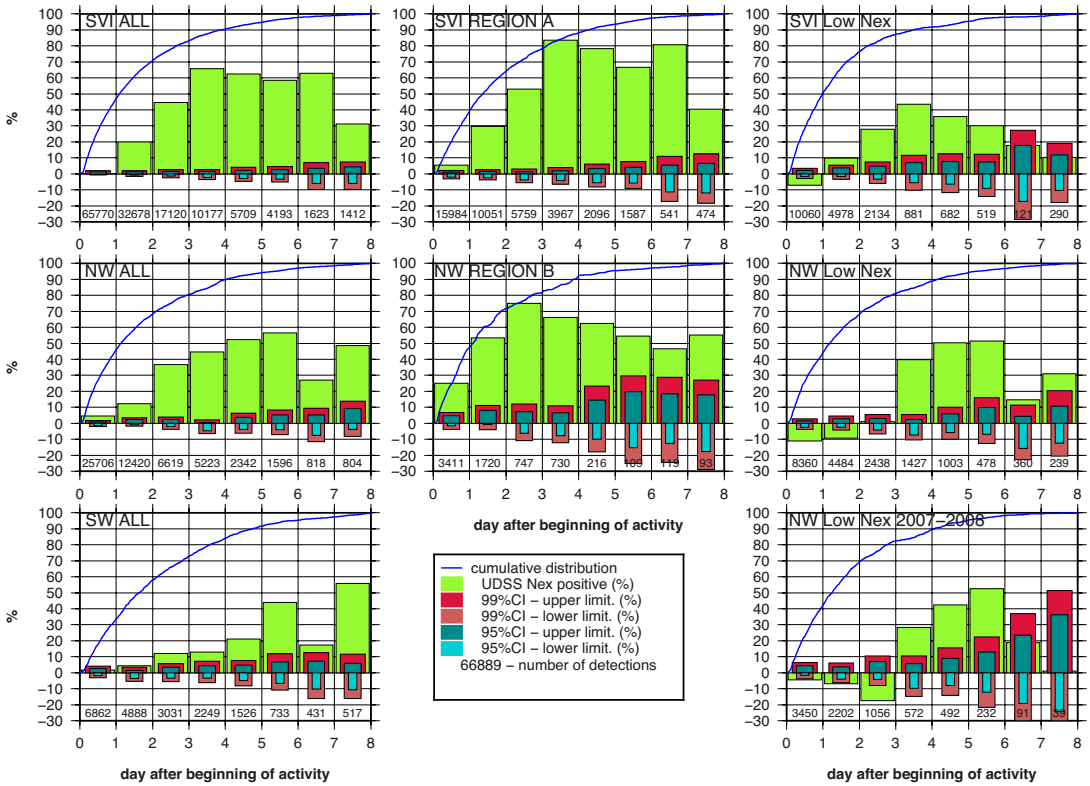

FIGURE 4.9: N_{ex} UDSS histograms for the 3 detection catalogues SVI (top), NW (middle and bottom right) and SW (bottom left). N_{ex} UDSS is computed every day up to 8 days after the beginning of activity. The percent cumulative detection distributions for each catalogue is provided (blue curve) and the associated number of detection in each 1 day-interval is given at the bottom of each panel. Lower and upper limits of 95% and 99% confidence intervals are given, distinguished by blue and red color bars, respectively.

4.3.4 Tidal sensitivity of rapid tremor reversals vs the main front

Thomas et al. [2013] noted that large, high-amplitude Rapid Tremor Reversals (RTRs) [*Houston et al.*, 2011] in northern Washington occur almost exclusively during times of positive UDSS. We use time-distance plots of our SVI LFE catalogue to identify RTRs on southern Vancouver Island and examine their sensitivity to UDSS. For each tremor episode, we project LFE family locations onto an along-strike profile and plot distance-along-strike versus time. We identify subjectively RTRs as linear streaks of LFE detections moving at high apparent velocities in the opposite direction to the main slip front. Figure 4.11 shows the location of the along-strike profile (panel a) as well as time-distance plots for the 2003 and 2012 tremor episodes (panel b).

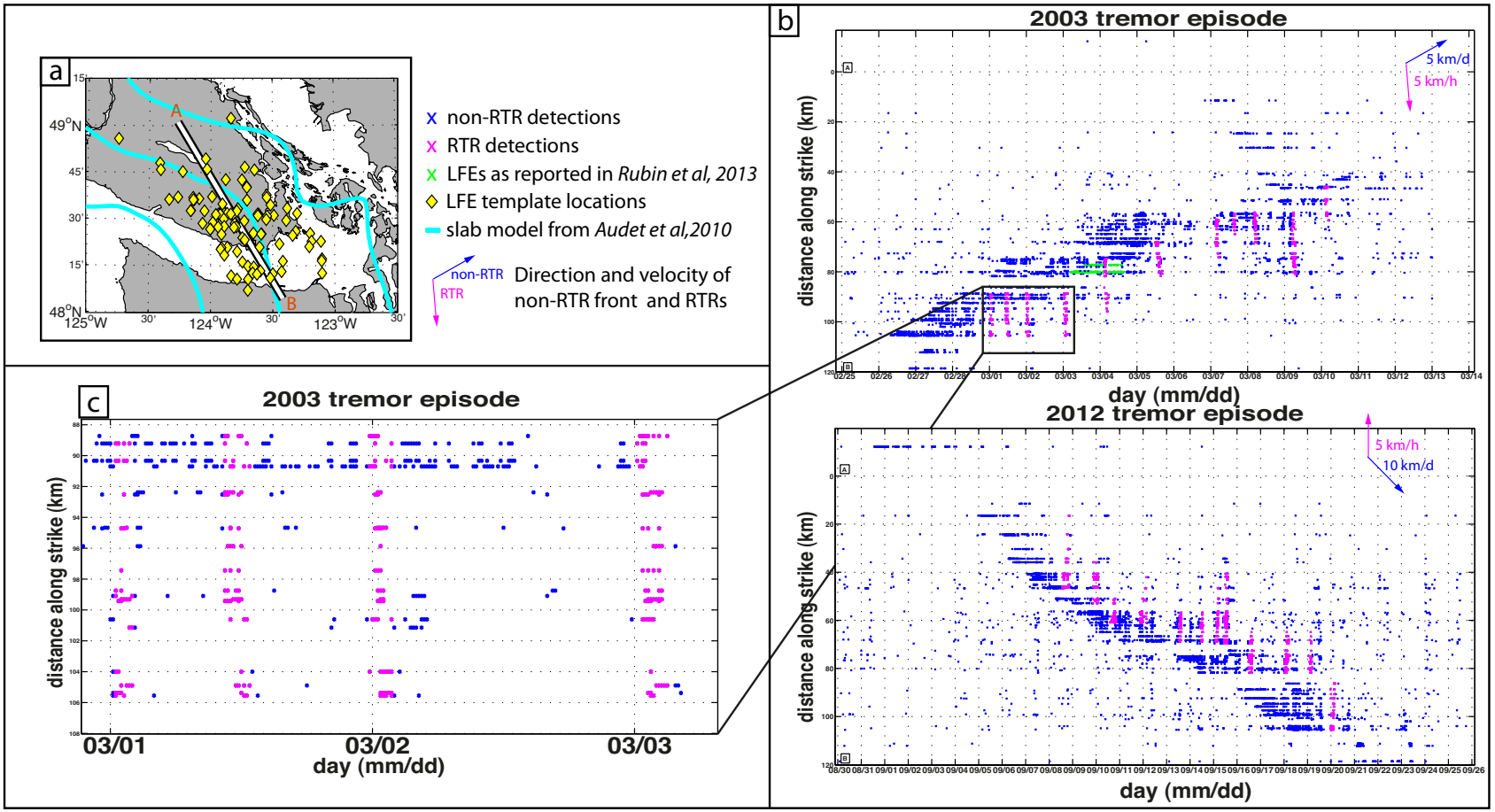

FIGURE 4.10: (a) Location of the along-strike profile used for the time-distance plot in panel b and SVI LFE locations (yellow diamonds). Cyan lines indicate the 20, 30 and 40 km depth contours to the top of the subducting Juan de Fuca plate modeled by *Audet et al.* [2010]. (b) Time-distance plots for the 2003 and 2012 tremor episodes. Blue and magenta detections represent detections from non-RTR front and RTRs, respectively. Green detections represent LFEs that participated in the small-scale secondary fronts of March 3, 2003 as reported by *Rubin and Armbruster* [2013]. Direction and along-strike velocity of non-RTR front and RTRs are provided in each plot. (c) zoom of the 2003 tremor episode between March 1 and March 3.

Note that in 2012, the main slip front propagated from NW to SE, opposite its usual direction. For each RTR, we determine the duration, the along-strike distance of propagation and the along-strike velocity. Results for all tremor episodes for which RTRs were confidently identified are reported in Tables 4.1 and 4.2.

# RTR	start time	end time	duration (hh:mm)	distance along-strike (km)	distance along-dip (km)	Velocity along-strike (km/h)
2003 - 1	01/03 00:23	01/03 02:10	1:47	16.2	7.9	9.1
2	01/03 10:25	01/03 12:53	2:28	16.7	9.5	6.8
3	01/03 23:36	02/03 01:50	2:14	16.7	9.5	7.5
4	02/03 23:56	03/03 03:17	3:31	16.7	9.5	5.0
5	04/03 02:43	04/03 05:24	2:41	20.8	10.2	7.8
6	05/03 11:59	05/03 15:20	3:21	13.4	11	4.0
7	07/03 02:36	07/03 05:03	2:54	14.9	10	5.1
8	07/03 14:26	07/03 15:59	1:33	8.1	4.7	5.2
9	08/03 03:49	08/03 07:17	2:28	12.4	11.8	5.0
10	09/03 04:36	09/03 07:44	3.08	24.5	12.7	7.8
11	10/03 10:49	10/03 04:56	3.07	13.4	6.1	4.3
2004 - 12	14/07 00:33	14/07 03:30	2:57	16.7	9.5	5.7
13	14/07 23:52	15/07 03:49	3:57	28.8	12.8	7.3
14	16/07 23:29	17/07 03:46	4:17	25.4	13.6	5.9
15	18/07 10:58	18/07 15:14	4:16	21.7	7.2	5.1
16	19/07 00:06	19/07 03:03	2:57	13.3	12.7	4.5
17	21/07 03:40	21/07 06:18	2:38	8.1	5.1	3.1
18	21/07 15:29	21/07 19:06	3:37	4.7	2.7	1.3
2005 - 19	11/09 13:24	11/09 18:39	5:15	19.1	9.5	3.6
20	12/09 03:51	12/09 00:47	4:56	14.2	7.4	2.9
21	12/09 20:56	13/09 00:33	3:37	13.1	6.1	3.6
22	13/09 21:54	14/09 03:09	5:15	19.8	7.1	3.8
23	14/09 22.12	15/09 01:29	3:17	25.4	10.0	7.6
24	15/09 06:44	15/09 11:00	4:16	10.4	6.9	2.4
25	15/09 22:50	16/09 02:46	3:54	13.4	6.9	3.4
26	16/09 23:28	17/09 03:04	3:36	12.5	6.8	3.5
27	18/09 00:45	18/09 06:59	6:14	43.1	7.1	6.9
28	19/09 11:14	19/09 17:09	5:55	22.3	8.7	3.8
2008 - 29	15/05 19:47	16/05 00:13	4:26	16.7	9.5	3.8
30	18/05 00:19	18/05 05:26	5:07	25.3	9.8	4.9
31	19/05 00:52	19/05 05:18	4:26	19.1	10.0	4.3
32	21/05 00:57	21/05 05:23	4:26	24.0	12.3	5.4
33	23/05 14:00	23/05 19:48	5:48	21.2	5.8	3.7
34	27/05 04:18	27/05 09:25	5:07	17.0	10.4	3.3

TABLE 4.1: RTRs documentation for 2003, 2004, 2005, 2008.

# RTR	start time	end time	duration (hh:mm)	distance along-strike (km)	distance along-dip (km)	Velocity along-strike (km/h)
2010 - 35	22/08 21:15	23/08 00:47	2:52	16.7	9.5	5.8
36	24/08 00:39	24/08 03:47	3:08	16.7	9.5	5.3
37	24/08 23:06	25/08 02:46	2:40	16.7	9.5	6.3
38	25/08 10:51	25/08 14:15	3:24	16.7	9.5	4.9
39	26/08 22:52	27/08 02:32	3:40	23.3	12.3	6.3
40	27/08 22:53	28/08 01:46	2:53	11.4	11.3	4.0
41	28/08 15:04	28/08 18:12	3:08	12.5	6.8	4.0
42	29/08 13:31	29/08 16:08	2:37	7.1	4.7	2.7
43	31/08 02:35	31/08 06:30	3:55	17.0	8.1	4.3
44	02/09 03:24	02/08 06:48	3:24	22.7	4.7	6.7
2011 - 45	22/08 23:39	23/08 02:29	2:50	16.7	9.5	5.9
46	23/08 21:09	23/08 23:59	2:50	16.7	9.5	5.9
47	25/08 22:31	26/08 02:32	4:01	16.7	9.5	4.2
48	26/08 07:58	26/08 11:45	4:47	11.9	6.5	2.5
49	29/08 11:20	29/08 16:32	5:12	21.0	6.7	4.0
50	30/08 13:05	30/08 15:13	2:08	12.5	6.8	5.9
51	31/08 00:40	31/08 02:47	2:07	9.0	10.9	2.5
52	01/09 02:53	01/09 05:01	2:08	8.2	10.9	3.8
2012 - 53	08/09 13:17	08/09 21:02	7:45	29.5	18.2	3.8
54	09/09 20:19	10/09 02:15	5:56	17.0	10.0	2.9
55	10/09 13:40	10/09 20:58	7:18	10.0	7.6	1.4
56	11/09 19:20	12/09 03:33	8:13	18.9	9.3	2.3
57	13/09 12:25	13/09 16:31	4:06	12.0	10.8	2.9
58	14/09 10:19	14/09 13:58	3:39	12.0	16.3	3.3
59	15/09 01:23	15/09 05:29	4:06	22.2	12.6	5.4
60	15/09 10:31	15/09 14:37	4:06	19.0	11.6	4.6
61	16/09 11:37	16/09 17:06	5:29	16.9	10.0	3.1
62	18/09 00:35	18/09 06:04	5:29	16.9	10.0	3.1
63	19/09 00:47	19/09 04:53	4:06	16.9	10.0	4.1
64	19/09 22:41	20/09 04:37	5:56	19.2	9.5	3.2

TABLE 4.2: RTRs documentation for 2010, 2011, 2012

For each LFE family, we determine the percentage of detections that take place as part of RTRs and we compute N_{ex} values corresponding to positive UDSS for both RTR detections and non-RTR detections. A summary of the results are presented in supplementary material Table B1 in Appendix B.

Following *Rubin and Armbruster* [2013], we estimate the contribution from the RTR events to the total stress drop $\Delta\tau_{sd}$ for a given LFE as:

$$\Delta\tau_{sd} = \frac{\#\text{ detections in a RTR}}{\#\text{ total detections}} \frac{D\mu}{L_s \pi}, \tag{4.4}$$

where D is the total slip accumulated at an LFE location during a tremor episode, that is $D \approx 2$ cm according to geodetic estimates [*Schmidt and Gao*, 2010, *Szeliga et al.*, 2008, *Wech et al.*, 2009], $\mu = 18$ GPa is the shear modulus (assuming V_p=6000 km/s, V_p/V_s=2.45 and ρ=3000 kg/m^3) and L_s is the width of the slip front. We can estimate the latter quantity by considering the time interval during which a given LFE is active (within an individual RTR or as part of the main front) and multiplying by the along-strike velocity (assuming propagation is dominantly along strike). Using the information in tables 4.1 and 4.2 and figure 4.11 we find that $L_s \approx 5$ km/day $\times$ 2 days ≈ 5 km/hr $\times$ 2 hours ≈ 10 km. That is, the width L_s of the actively slipping regions appears to be of the order of 10 km and approximately equivalent for the main front and RTRs.

4.3.5 Diurnal variation of LFE occurrence

Motivated by the observations of *Rubinstein et al.* [2008] and *Lambert et al.* [2009], we investigate LFE correlation with a previously described diurnal signal. *Rubinstein et al.* [2008] identified a strong peak in tremor spectra between 24 and 25 hr period and noted that the peaks of the envelope corresponding to the $\sim$ 24 hr period component of tremor do not correlate with daylight hours, when cultural noise is at its maximum. In contrast, the Vancouver Island study of *Lambert et al.* [2009] presented evidence for a significant, nontidal, daily variation in tremor activity, with higher sensitivity at midnight than at noon when noise levels are generally higher. To shed further light on the nature of this signal, we determine N_{ex} values for LFE detections falling within a given hour of the day, with results plotted in figure 4.12.

4.4 Results

4.4.1 LFE correlation with tidal stress

A concentration of LFE families in southern Vancouver Island in an up-dip region of high slab curvature centered near 48.43 N, 123.83 W, hereafter "region A", shows strongest correlation to tidal forcing during periods of positive and increasing UDSS (figure 4.4, panels B and D). In Washington state, the strongest correlation to tidal forcing during periods of positive and increasing UDSS (panels B and D) occurs for a more diffuse distribution of LFE families near the town of Sequim (hereafter "region B"). These 2 regions display a large surplus of detections with positive UDSS (N_{ex}>30%) and positive dUDSS (N_{ex}>3% up to 44%) at a significance level of 99% or greater. Away from these 2 regions, the distribution of N_{ex} values is generally more sporadics and disorganized. There appears to be little correlation between the mean tidal envelope amplitude and N_{ex} values for any of the 4 tidal components as shown in figures 4.3, 4.4 and 4.6 despite the fact that tidal amplitudes vary by over a factor of 10 across the entire region. We note that the more equivocal signature of tidal sensitivity in the SW LFE catalogue for most measures is most likely due to the reduced recording period for this array of stations, that is 2 episodes, versus 10 episodes for SVI.

A majority of LFE families display significant negative FNS N_{ex}. We performed a hypothesis test for spurious correlations (supplementary material figure S2 - for methodology, see *Thomas et al.* [2012]) and results reveal that the NW and SW LFE populations that correlated with negative FNS appear to be an aliasing effect. However, FNS N_{ex} for an LFE population beneath the northeast Olympic Peninsula cannot be explained as a spurious correlation with another stressing function.

Further details concerning the temporal dependence of LFEs within the stress cycle are revealed in figure 4.7 which displays N_{ex} binned in constant intervals of stress and stressing rate. For LFE families in "region A" (LFE #'s 29, 33, 37-39, 44, 48-53, 55, 56, 63, 66, 72, 73, 75, 84), highest sensitivity to UDSS occurs close to the positive maximum of UDSS (N_{ex} +1 >2) between 1.5 and 2.0 kPa (middle top plot - UDSS), when UDSS is increasing (N_{ex} + 1 >1.5) between 10 and 15 Pa/min (bottom plot - dUDSS). For LFE families in "region B" (LFE #'s 108, 112, 114, 119, 121, 123, 131,

133, 139, 146, 147), highest sensitivity to UDSS occurs close to the positive maximum of UDSS (N_{ex} +1 >1.5) between 1.0 and 1.5 kPa, when UDSS is increasing (N_{ex} + 1 >1.5) between 5 and 10 Pa/min. The more northerly LFEs of the SW dataset are sensitive to positive and increasing UDSS but the general sensitivity is less obvious for the entire SW dataset.

The overall sensitivity of all families to positive UDSS, dUDSS is also apparent in the stacked phase plots in figure 4.8. For SVI and NW catalogues, the majority of LFEs fail during times of large, positive UDSS and large, positive UDSS rate, with at least one preferential failure time at radial values above 150% of the expected value and with a N_{ex} + 1 value exceeding the 99% confidence interval. This leads to a $\sim$ 1.3 hour and $\sim$ 2 hour phase advance in the time of the peak radial value with respect to the peak UDSS, for SVI and NW datasets, respectively. As for previous measures, the tidal sensitivity for the SW catalogue is less clear. A majority of LFEs fail during times of large positive UDSS but negative dUDSS, above 100% of the expected value and with a N_{ex} + 1 value exceeding the 99% confidence interval.

4.4.2 Time dependent tidal sensitivity

indent Figure 4.9 displays the sensitivity of LFE occurrence as measured by N_{ex} to positive UDSS forcing as a function of time. For SVI (top) and NW (middle) catalogues and all families and years considered (left panels), sensitivity rises steeply from near zero on the first day of strong activity to a maximum $\sim$ 4 days later for SVI, and $\sim$ 6 days later for NW. Similar behavior is observed when catalogues are divided into subsets with high N_{ex} values (region A from SVI and region B from NW) and subsets with low N_{ex} values, with a shift in the maximum N_{ex} to 3 days or so later for region B. Although there is indication of a sustained increase in UDSS sensitivity 6 days after the initial onset of LFE activity for families in the SW catalogue, this pattern cannot be confirmed at the same confidence levels as the two other catalogues.

4.4.3 Tidal sensitivity of RTRs vs the main front

For 7 tremor episodes (2003-2005, 2008, 2010-2012) in southern Vancouver Island, we identify a total of 64 RTRs (Tables 4.1 and 4.2 and figure 4.11). RTRs have N_{ex}

values that greatly exceed those of the main front, propagate along strike at an average speed of 5 km/hr, and have an average duration of 4 hours. We note that, during RTRs, the non-RTR events that constitute the main front continue producing tremor. Our observations indicate that 6.8% of all detections per episode occur within individual RTRs (i.e. the ratio of detections required in (4)) as averaged over all LFE families and ETS episodes. Moreover, as many as one third of all detections for a given LFE family can occur within RTRs (see supplementary table 1), and a majority (72%) of RTRs occur exclusively during periods of positive UDSS. We further note that, in general, LFE families in "region A" possess higher percentage of RTR events (>20%). However, some LFE families with lower sensitivity to UDSS (south of "region A" and few downdip families) also possess high percentage of RTR events. We compute the stress drop associated with an LFE as part of an RTR and for 64 RTRs that include a total of 1312 "ruptures" (or LFE-RTR combinations). The mean stress drop is ~ 0.8 kPa, an order of magnitude smaller than that associated with the main slip front (and secondary fronts analyzed by *Rubin and Armbruster* [2013]).

4.5 Discussion

We now proceed to examine the implications of our observations on tidal modulation of LFEs in northern Cascadia for our general understanding of the slow slip process.

4.5.1 Spatial distribution of tidal sensitivity

The population of LFEs beneath the northeast Olympic Peninsula that correlate with compressional normal stress is enigmatic. Several authors have shown that tremor and LFEs are primarily sensitive to variations in tidally induced shear stresses and often do not respond to larger normal stress variations [*Hawthorne and Rubin*, 2010, *Thomas et al.*, 2009, 2012]. A few events in *Thomas et al.* [2012] did appear to have negative FNS correlation that those authors attributed to a releasing right-bend along the San Andreas fault. The increase in LFE rate during times of tidally induced compression is inconsistent with models of Coulomb stress transfer as increases in normal stress

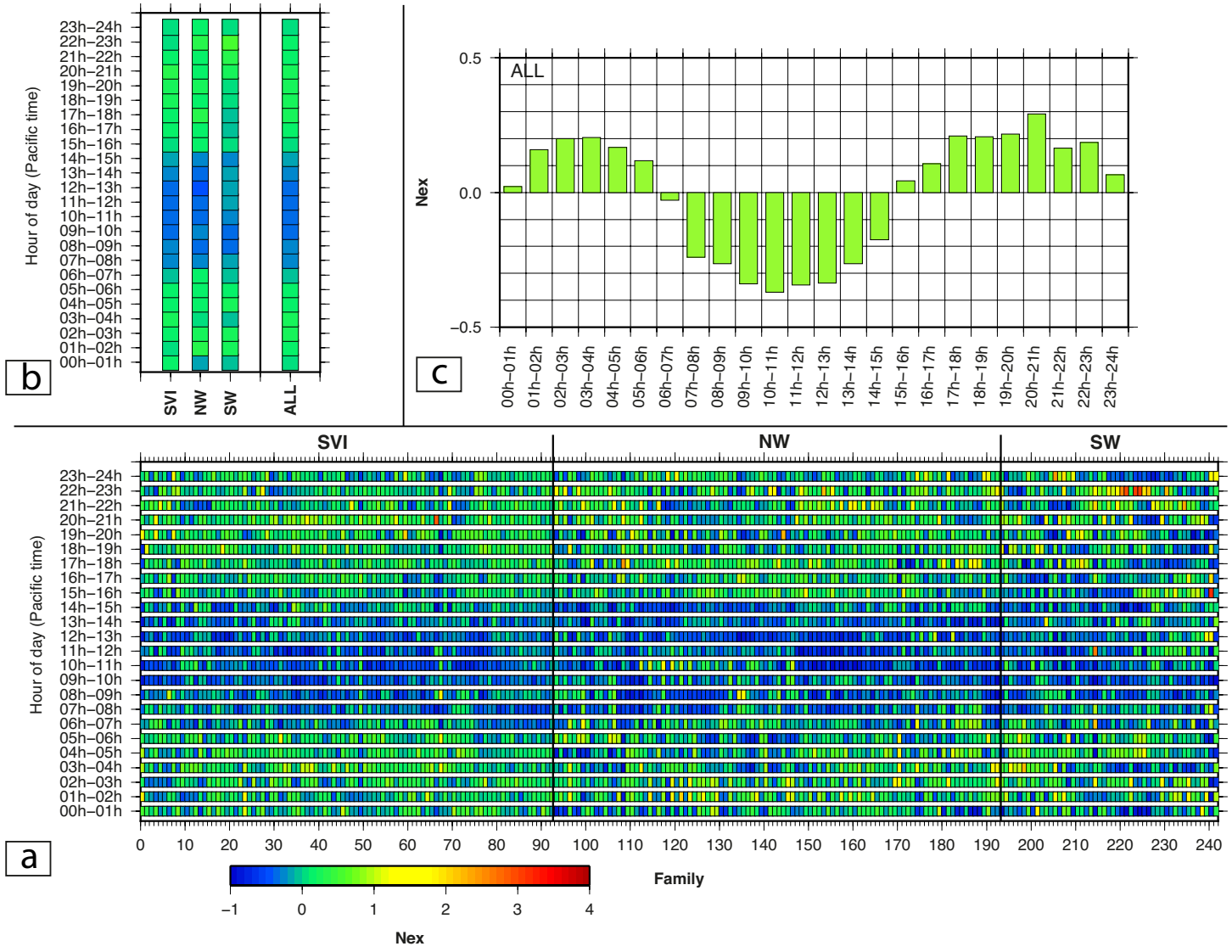

FIGURE 4.11: LFE rate plots as a function of hour of day (Pacific time). (a) Each column corresponds to an individual LFE family (ordered from north to south, all detection catalogues combined - subdivision shown by black vertical lines) and each row corresponds to an hour interval. N_{ex} values in each hour range is color-coded with colors as shown on the color-bar legend. Blue colors represent a deficit of LFE detections (N_{ex} <0), whereas green-warm colors represent a surplus LFE detections (N_{ex} >0). (b) Each column corresponds to the entire set of LFE family in each region. See (a) for color coded interpretation. (c) Histogram of N_{ex} for each hour range of a 24 hour day.

should inhibit, not promote, fault slip [*Ader et al.*, 2012]. If we account for poroelastic effects the Skempton coefficient, or the ratio of the change in pore fluid pressure due to a change in applied normal stress at undrained conditions of > 0.9 estimated by *Hawthorne and Rubin* [2010] suggests that most of the applied normal stress is buffered by corresponding increases in fluid pressure which also does not explain the negative FNS correlation. *Perfettini et al.* [2001] studied the effect of periodic normal stress changes on a spring-block system and found that the shear stress response could exhibit a range of phase lags relative to the normal stress fluctuations depending on model parameters. It is possible that effects such as those could explain the negative normal stress correlation but to fully understand the effects of changing normal stress on LFE occurrence will likely require incorporating periodic changes in normal stress into slow slip simulations.

The spatial distribution of tremor sensitivity to tidal shear-stress forcing (UDSS, Figure 4b) in northern Cascadia varies in a semi-coherent fashion across the region with localized areas, in particular southwestern Vancouver Island (Region A) and the southeastern Strait of Juan de Fuca / adjacent Washington state (Region B), displaying higher sensitivity than their surroundings. Recent studies have used various realizations of rate-and-state friction models to argue that tidal sensitivity can be interpreted as a probe of either effective stress, frictional properties, or both [*Ader et al.*, 2012, *Beeler et al.*, 2013, *Hawthorne and Rubin*, 2013, *Thomas et al.*, 2009, 2012]. Following *Beeler et al.* [2013], we can employ the observations of LFE tidal modulation and a steady-state, rate-dependent friction model to constrain the physical properties of the creeping fault. The friction model is

$$\tau = \tau_0 + a\sigma_e \ln(\frac{V}{V_L}) \tag{4.5}$$

where τ is the maximum total shear stress resistance including tidal contributions, τ_0 is shear resistance at the long-term displacement-averaged creep rate V_L, V is the creep rate of the fault surrounding an LFE patch, σ_e is effective normal stress, and a is a friction coefficient from rock experiments. By equating the ratio of slip rates V/V_L to $N_{ex} + 1 \approx 1.3$ and assuming a value for tidal stress (UDSS) amplitude $|\tau - \tau_0| = 2$ kPa,

we find $a\sigma_e = 7.6$ kPa. Assuming $a = 0.04$ (extrapolation of the rate parameter a for gabbro in hydrothermal conditions [*Liu and Rice*, 2009]), yields a mean effective normal stress of σ_e of 0.2 MPa, consistent with other model estimates between 0.2-3 MPa of *Liu and Rice* [2007] and *Hawthorne and Rubin* [2013]. In contrast, if we assume a typical lithostatic pressure gradient and hydrostatic pore pressure, the effective normal stress at a nominal depth of 30 km is $\sigma_e = 530$ MPa, or three orders of magnitude larger. The low effective normal stress implied by the analysis above is most easily explained by high pore fluid pressures near the plate boundary [*Bartlow et al.*, 2012, *Beeler et al.*, 2013, *Thomas et al.*, 2012] as supported by the independent observations of *Audet et al.* [2009].

The existence of secondary events that appear to be tidally triggered may result in underestimated effective stress values. The model used to infer effective stress above considers the influence of tides directly on the LFE asperity and indirectly via surrounding creep [*Beeler et al.*, 2013]. Within this framework, if creep is the dominant source of stress, changes in LFE rates can be interpreted as being due solely to the modulation of the main front, as secondary events have not been documented in Parkfield (either because they do not exist or because of the limited spatial resolution of the LFE dataset). In Cascadia, some LFE families possess a significant fraction of events that are related to stress changes from secondary events that the *Beeler et al.* [2013] model does not consider. For this reason the estimated effective normal stress likely represents a minimum bound. Models that consider only slip rate modulation may still be valid in some parts of Cascadia because i) highly modulated families have no events that are directly associated with identifiable RTRs (see supplementary material table S1), ii) N_{ex} values do not correlate with the percentage of RTR events in each LFE family, and iii) non-RTR populations are still weakly modulated. These observations imply that modulation of creep rate due to tidal stress and tidal triggering of secondary events are jointly responsible for the observed tidal sensitivity.

4.5.2 The role of secondary events

Secondary events are a more important component of slow slip processes than previously thought as up to 34% of events within a given LFE family occur as part of

RTRs and our preliminary analysis does not account for small-scale secondary events close to the main front [*Ghosh et al.*, 2012, *Obara et al.*, 2012, *Rubin and Armbruster*, 2013]. *Rubin and Armbruster* [2013] estimated $\sim$ 10 kPa stress drops for the main and small-scale secondary fronts. Here, we find that the average stress drop for LFEs in an RTR is $\sim$ 0.8 kPa, an order of magnitude smaller. *Hawthorne and Rubin* [2013] modeled tidal stressing on a fault that obeyed a velocity weakening-to-strengthening constitutive relation and found that secondary fronts arose frequently in their simulations. However, they ultimately concluded that their modeled fronts were not a realistic representation of actual secondary fronts because they do not repeatedly rupture the same section of fault as observed, and matching observed propagation speeds requires stress drops that are comparable to those of the main front which they considered implausibly large for their adopted model. Having equal stress drops as proposed by *Rubin and Armbruster* [2013] introduces modeling problems as it implies that the small-scale secondary fronts slip much faster than the main front in order to produce the much faster propagation speeds. This seems hard to reconcile with a single state variable friction law [*Rubin*, 2011]. In contrast, our estimate of stress drop for LFEs in an RTR is one order of magnitude smaller which means that the secondary fronts should have approximately the same slip velocity as the main front, eliminating the latter discrepancy.

The time and length scales of our RTRs and the secondary fronts of *Rubin and Armbruster* [2013] are different. For example, the difference in stress drop estimates arises primarily from contrasting estimates for the width of the slip front L_s (1 km vs 10 km) in (4). The temporal distinction between small-scale events and RTRs is evident in Figure 4.11b that displays LFEs in green that participated in the small-scale secondary fronts of March 3, 2003 as reported by *Rubin and Armbruster* [2013]. We note that the succession of small-scale secondary fronts immediately follows the main RTR on that date, extends through a second RTR on March 4 2003, and affects a different region closer to the main front. Similar observations hold for July 14, 2004 (see Figures 5 and 8 of *Rubin and Armbruster* [2013]). Furthermore, the small-scale fronts propagate at higher speeds, up to 20 km/hr, than the RTRs with speeds near 5 km/hr, an observation consistent with those of *Obara et al.* [2012].

Our results suggest that tides trigger secondary events but the specific role of tides

in nucleating secondary events is still unclear. *Thomas et al.* [2013] showed that 12 secondary events (5 RTRs and 7 streaks) during the 2010 and 2011 tremor episodes occur exclusively during thrust encouraging shear stress. Similarly, we find that 46 out of 64 RTRs occur during times of positive UDSS and have N_{ex} values that are systematically larger than non-RTR events (though we note that N_{ex} may not be an appropriate measure to quantify tidal sensitivity of RTRs). *Rubin and Armbruster* [2013] note that their small-scale fronts occur throughout the tidal cycle and repeatedly rupture the same fault region suggesting that tides alone are not a sufficient source of stress to drive small-scale secondary fronts. In the simulations of *Hawthorne and Rubin* [2013] large-scale secondary fronts result from stress recovery following the main front, tidal loading, and spatial variability in slip rate modulation due to the tides. They also found that secondary fronts rarely arose in simulations that did not incorporate tidal stressing.

4.5.3 Tidal sensitivity and LFE recurrence intervals

Motivated by the observations of variable spatial sensitivity to tidal forcing, we analyze the cumulative temporal distribution of a selection of SVI LFE families at up-dip and downdip locations over the period February 23, 2003 through July 1, 2006 to establish whether families with different tidal sensitivities might also display distinct recurrence characteristics [*Wech and Creager*, 2011]. As in the latter study, the results in figure 4.10 reveal that up-dip families (#18 : low sensitivity, #55 : high sensitivity) are characterized by large, punctuated increases in detections, principally during major ETS episodes, whereas downdip families (#67 : low sensitivity, #7 : high sensitivity) display a more continuous accumulation of detections, independent of tidal sensitivity. We further note that updip, highly modulated families in SVI possess a higher percentage of RTR events (>20%). In contrast, some downdip families that have few or no RTRs also have high N_{ex} values, indicating that tidal modulation is not only due to RTRs.

Unlike previous reports from Parkfield and Shikoku, there does not appear to be a systematic variation in tremor sensitivity with depth. On the San Andreas fault near Parkfield, deeper LFE families tend to be more sensitive to tidally induced right-lateral

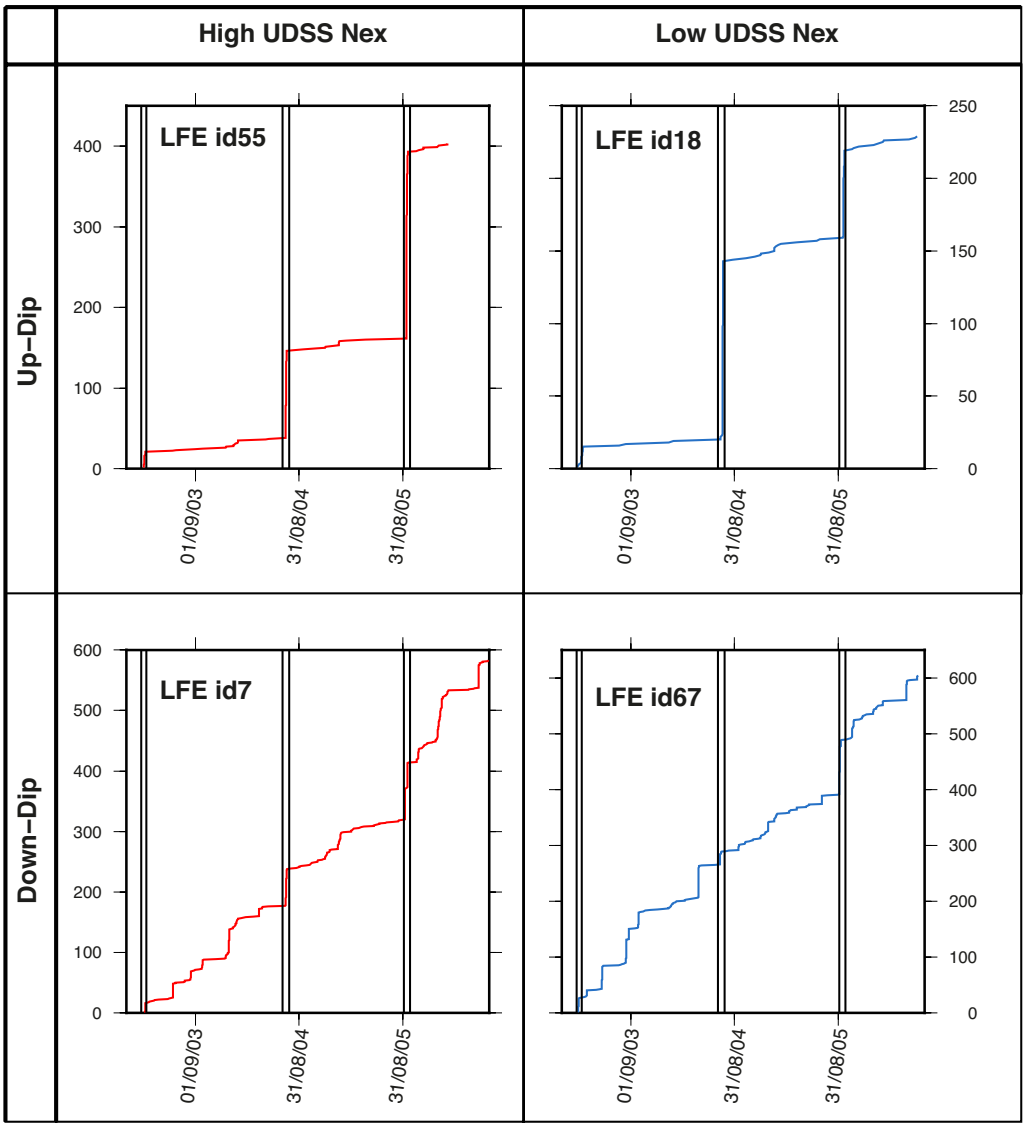

FIGURE 4.12: Cumulative distribution functions over a 3.5 year period for a selection of distinct low versus high tidal sensitivity and up-dip versus down-dip SVI LFE families. In each plot, the ordinate axis corresponds to cumulative detections and vertical black lines demarcate major ETS episodes.

shear stress than shallow ones [*Thomas et al.*, 2012] whereas in Shikoku, the highest sensitivity to tidal shear stress occurs preferentially in up-dip regions of tremor [*Ide*, 2010]. In contrast, our results suggest that tidal sensitivity must depend, at least in part, on physical properties that vary independently of depth, consistent with more general observations of laterally heterogeneous tremor distribution and strength [*Gomberg and Prejean*, 2013, *Husker et al.*, 2012]. In a study of tremor strength in northern Washington using beamforming of Array-of-Arrays data between 2009 and 2010, *Ghosh et al.* [2012] isolated several patches of elevated tremor density that coincide closely in

location with LFE families from our NW catalogue (i.e "region B") exhibiting strong tidal sensitivity.

4.5.4 Phase of LFE asperity failure relative to tidal stress

The majority of LFEs in northern Cascadia fail during times of large, positive and increasing UDSS, in contrast to observations from Parkfield where LFEs tend to occur when right lateral stressing rate has begun to decrease after the peak stress [*Thomas et al.*, 2012]. The phase relations evident in figure 4.8 for the SVI ($\sim$ 1.3 hours in advance of peak stress) and NW ($\sim$ 2 hours in advance of peak stress) subregions corroborate observations made by *Klaus* [2012]. She investigated the relation between tremor amplitude and tidal stress in northern Cascadia and observed that peak tremor amplitude precedes peak tidal stress by 1 to 2 hours. *Hawthorne and Rubin* [2010] also reported a phase advance in the tremor catalogue of *Wech and Creager* [2008] with respect to maximum shear stress.

The phase advance between peak LFE excitation and peak tidal stress may reflect how the background loading rate influences the timing of LFEs in response to the tidal load. Simulations of *Hawthorne and Rubin* [2013] produced a peak slow slip rate that was either in phase with peak tidal stress or slightly delayed (as observed in Parkfield) and cannot produce an advance. If LFEs are simply a passive response to overriding stress, one might expect peak LFE rates in phase with peak tidal stress, contrary to the observations. *Beeler et al.* [2013] used the same basic model as *Ader et al.* [2012] where LFE sources are small seismic patches that fail at a threshold stress on an otherwise creeping fault plane but allowed for the possibility that tectonic loading and the tides may directly influence LFE occurrence times. Their model equates LFE rate to the sum of stressing rate contributions from i) plate motion (negligible during slow slip events as slip rate is up to 10 times the plate rate), ii) background creep (in our case, slow slip), and iii) the tides acting directly on the LFE patch. For threshold failure, the contribution from slow slip/creep is expected to be in phase with the tides, whereas LFE occurrence due directly to tidal stressing should follow tidal stressing rate with a 90° phase advance from peak tidal stress. An intermediate phase advance between 0 and 90° can thus be achieved by balancing the contributions from ii) and iii). The

relevant coefficients depend on a range of parameters and allow us to constrain patch size L_{patch} as :

$$L_{patch} = \left[\frac{\pi^2 \Delta\tau_{ss}(1-\nu)}{\mu T \Delta V \tan\theta} + L_m^{-1} \right]^{-1} \tag{4.6}$$

Here we assume values for dimension of the main slip front $L_m = 60$ km, amplitude of tidal shear stress $\Delta\tau_{ss} = 2$ kPa, shear modulus $\mu = 18$ GPa, Poisson's ratio $\nu = 0.4$ and tidal period $T = 12.4$ hours. We estimate $\Delta V = 1.04 \times 10^{-4}$ m/hr using a linearized rate strengthening constitutive equation

$$\Delta V = \frac{V_{ss} \Delta\tau_{ss}}{a\sigma_e} \tag{4.7}$$

where V_{ss} is the steady state velocity during an SSE ($V_{ss} = 4.2 \times 10^{-4}$ m/hr , using a total slip of 2 cm and a duration of 2 days for slip at a particular asperity). Inserting phase advances θ of $\pi/6$ and $\pi/3$ results in characteristic LFE source dimensions L_{patch} of ~ 1.1 km and ~ 3.2 km, respectively.

Similarly, the model of *Ader et al.* [2012] can produce a phase advance over a range of periods defined relative to the timescale for state evolution,

$$T_\theta = \frac{2\pi D_c}{V_{ss}}, \tag{4.8}$$

From their figure 1, phase advances between $\pi/6$ and $\pi/3$ correspond to values of T/T_θ of $\sim 10^3$. Taking T=12.4 hr and $V_{ss} = 4.2 \times 10^{-4}$ m/hr implies that the characteristic length scale D_c on the order of 1 micron, in agreement with laboratory experiments [*Marone*, 1998, *Paterson and Wong*, 2005]. Finally, it is also possible that the bulk phase shifts evident in figure 4.8 result from combined effects of both modulation and triggering. For example, if slip front modulation occurs in phase with tidal shear stress [*Hawthorne and Rubin*, 2013] and the secondary events are triggered at times of peak stressing rate similar to shallow/laboratory earthquakes [*Bartlow et al.*, 2012, *Beeler and Lockner*, 2003, *Lockner and Beeler*, 1999] then the combination of those two effects could manifest as a phase between peak stress and peak stressing rate.

4.5.5 Evolution of tidal sensitivity through slow slip events.

A number of authors have suggested that tidal sensitivity changes relative to the background slip rate [*Lambert et al.*, 2009, *Thomas et al.*, 2012]. In particular, *Houston* [2013] has observed that tremor in Washington is more sensitive to tidal stressing after the main slip front has passed. Figure 4.9 demonstrates that LFE sensitivity to UDSS rises dramatically from near zero in the first day of strong activity to a maximum 4 days later suggesting that the background loading rate at the onset of slow slip is high, overwhelming the tidal influence. As the slow slip front advances, the background slip rate decreases and the sensitivity of LFEs to tides increases. These observations are in agreement with the modeling results of *Hawthorne and Rubin* [2013] who documented a relationship between slip rate and stress on the part of the fault at steady state conditions (figure 7 in their paper). More specifically, their model suggests that modulation of creep by tidal stressing is stronger at low slip rates. We also observe that a majority of RTRs occur during time of positive UDSS and associated N_{ex} are always higher than the N_{ex} of non-RTR events. It is worthwhile to note that, as shown in figure 4.11b, RTRs start few days after the first day of strong activity and therefore RTRs probably play a role in the observed increase of tidal sensitivity with time.

4.5.6 24 hour periodicity of LFE detections

The presence of a 24-hour periodicity in tremor occurrence in northern Cascadia previously documented by *Rubinstein et al.* [2008], *Wech and Creager* [2008] and *Lambert et al.* [2009] is clearly evident within the LFE catalogues as a deficit of detections between 6AM and 3PM (Pacific Daylight Savings Time) through the entire area of study (see figure 4.12). We also note a "weekend" effect with an increase in detections during working hours of weekend days, as observed in Wech's tremor catalogue (personal communication). The correspondence of this time interval with regular working hours suggests that anthropogenic cultural noise contributes to increased detection thresholds during working hours (e.g. *Rydelek and Sacks* [1989]), and that a larger proportion of events are undetected during the half-cycle of working hours. Given the timeframe of our LFE detections (e.g. 10 three-week ETS episodes recorded over 11 years for SVI),

we believe that any biassing effects on our tidal analysis due to diurnal variations are minimal.

4.6 Conclusions

We analyzed the sensitivity of LFEs to tidal forces using 3 LFE detection catalogues for northern Cascadia. We find localized areas showing higher sensitivity to UDSS than their surroundings, which suggests that tidal sensitivity must partially depend on laterally heterogeneous physical properties such as variable pore fluid pressures and/or frictional properties along the plate interface. The majority of LFEs in southern Vancouver Island and northern Washington occur during times of large, positive and increasing UDSS. The $\sim$ 1-2 hours phase advance between peak LFE excitation and peak tidal stress can be explained by balancing contributions from background slow slip and from tides acting directly on LFEs, as proposed in the model of *Beeler et al.* [2013] in which LFE sources are small seismic patches that fail at a threshold stress on an otherwise creeping fault plane.

For 7 tremor episodes in southern Vancouver Island, we identified 64 RTRs with a characteristic duration of $\sim$ 4 hours and a mean velocity of $\sim$ 5 km/hr. Secondary events are an important component of slow slip processes as up to one third of events within a given LFE family occur as part of RTRs. A majority of RTRs occur during periods of positive UDSS, with N_{ex} values larger than non-RTR events, suggesting that tides may trigger secondary events. Therefore, the observed tidal sensitivity to UDSS likely represents a combination of modulation of creep rate due to tidal stress and tidal triggering of secondary events. The average stress drop for LFEs in a RTR is estimated to be $\sim$ 0.8 kPa, one order of magnitude smaller than the estimated stress drop of the main slip front and small-scale secondary fronts estimated by *Rubin and Armbruster* [2013].

We find that that sensitivity to UDSS rises dramatically from near zero in the first day of strong activity to a maximum 4 days later. These observations are consistent with the modeling results of *Hawthorne and Rubin* [2013], who suggest that modulation of slip by direct tidal stressing is stronger well behind the main front, where the slip

speed is significantly below the "soft" speed limit set by their adopted friction law. We infer that the background loading rate at the onset of slow slip is high, overwhelming the tidal influence. As the slow slip front advances, the background slip rate decreases and the sensitivity of LFEs to tides increases. We suspect that RTRs are also partly responsible for the increase of tidal sensitivity with time as RTRs start few days after the beginning of strong activity and display high UDSS N_{ex}.

The presence of a 24-hour periodicity in tremor occurrence in northern Cascadia suggests that anthropogenic cultural noise contributes to increased detection thresholds during working hours and that a larger proportion of detections is missed during the half-cycle of working hours.

Chapter 5

Conclusions

In this final chapter, I summarize the main contributions of this thesis, discuss current limitations and present future research opportunities.

5.1 Key contributions and limitations

5.1.1 Blind deconvolution

We have implemented an analytical method that is capable of solving the blind deconvolution problem when two or more seismograms are available that share a common convolutional element (source or Green's function). We solved a system where the unknowns are the sources and source durations by using the separation of variables method [*Golub and Pereyra*, 1973]. Our solution is assembled using direct linear inversion to recover the sources and Newton's method to recover source durations. For the short time series lengths ($\sim$ 35 points) considered here we are able to recover source time functions for noise levels at 1% of the direct P-wave amplitude (or approximately 10% of scattered wave amplitudes). Our method of blind deconvolution has advantages. It does not require any assumptions concerning unknown sources beyond the restriction of minimum support, and can be used to recover source or Green's function depending on the multiplicity represented in the data set. Separation of variables is efficient as it transforms a large nonlinear problem in $\mathbf{y}$ ("pre-weighted" source function) and $\Delta\tau$ (positive change of source duration with iteration) into a large linear problem in $\mathbf{y}$ and a small nonlinear problem in $\Delta\tau$. However, at present, updating of $\Delta\tau$ proceeds slowly

through 1000's of iterations to arrive to a solution. Therefore this method is restricted to a small number of seismograms of limited duration. It is also important to note that the restriction to seismograms with noise levels at $\leq 1\%$ of the direct P-wave amplitude will limit consideration to a small proportion of observed signals.

5.1.2 Comparative study of LFE templates in northern Cascadia

Using data from Earthscope sources, POLARIS deployments and permanent networks, we generated LFE templates for southern Vancouver Island, Washington state and northern Vancouver Island, for a selection of tremor episodes between 2003 and 2012. We employed earthquake location software to determine representative LFE templates hypocentres and find that they fall within the tremor epicentral distributions, defining a distinct surface between the upper envelope of intraplate earthquakes and the lower envelope of overlying crustal seismicity. The $\sim \pm 2$ km location uncertainties do not allow us to specify precisely whether LFE hypocentres are located within the 3-4 km thick LVZ or along a very thin ($<$ 1km) surface atop. We performed moment tensor inversions for focal mechanisms and results show that SVI solutions as well as the average double couple solutions for NVI, NW and SW subarrays are consistent with shallow thrust faulting in the direction of relative plate motion. These results prompts us to conclude that LFEs are generated directly by shear slip on a comparatively sharp plate boundary.

Whether LFEs in Cascadia are distributed through a zone of several km or along a relatively sharp boundary has been a matter of debate. By using the source-scanning algorithm method to locate tremors in northern Cascadia, *Kao et al.* [2005] inferred that tremors are distributed over a depth range exceeding 40 km within a limited horizontal band. *Ghosh et al.* [2012] used multibeam-backprojection method to detect and locate tremor using multiple mini seismic arrays to map tremors in northern Cascadia over a depth range that may exceed 10km in the most easterly part where the slab is the deepest. Our results show that LFE hypocentres occur along tightly defined surfaces. These results are similar to those in southwest Japan [*Shelly et al.*, 2006] and in central Mexico [*Frank et al.*, 2013]. The conflicting results in Cascadia may be due to the poorer vertical resolution in earthquake location when only one mode (i.e S) is

employed, to the contaminating influence of simultaneous multiple arrivals for methods that do not use network combination, and to the possibility that some proportion of tremor is not due to LFEs and may have a wider depth distribution.

5.1.3 Tidal modulation of LFEs

We analyzed the influence of ocean tides on the triggering of the LFEs represented within the templates of chapter 3. We computed the sensitivities of these LFE families to the tidally induced FNS, UDSS and the corresponding time derivatives dFNS and dUDSS and we mapped their geographic variability. Two regions of LFE families show stronger correlation than their surroundings to tidal forcing during periods of positive and increasing UDSS that suggests that tidal sensitivity must partially depend on laterally heterogeneous physical properties such as variable pore fluid pressures and/or frictional properties along the plate interface. A majority of LFEs in SVI and NW fail during times of large, positive and increasing UDSS, which leads to a $\sim$1.3 hour and $\sim$2 hour phase advance between peak LFE excitation and peak tidal stress, for SVI and NW datasets, respectively. These results are consistent with a model [*Beeler et al.*, 2013] where the tidal influence has separate contributions from background slow slip and direct action on localized asperities. LFE sensitivity to UDSS rises dramatically from near 0 on the first day of strong activity in a given tremor episode to a maximum 3-4 days later. These results suggest that LFEs are modulated by tides but that the background loading rate at the onset of slow slip is high, overwhelming the tidal influence. As the slow slip front advances, the background slip rate decreases and the sensitivity of LFEs to tides increases. For 7 tremor episodes in SVI we identified 64 RTRs propagating along-strike at an average 5 km/hr, with a characteristic duration of 4 hours. We suspect RTRs to be partly responsible for the increase of tidal sensitivity of LFEs with time as RTRs start a few days after the beginning of strong activity and display higher sensitivity to UDSS than that of the main front. RTRs seem to play an important role in slow slip processes and it is likely that modulation of creep rate due to tidal stress and tidal triggering of secondary fronts are jointly responsible for the observed tidal sensitivity.

To date, the sensitivity of a group of LFEs to compressional normal stress remains

obscure. Unlike regular earthquakes occurrence for which reduced fault-normal stress is required from conventional frictional failure models, LFEs might be encouraged by clamping, implied by the sensitivity to negative FNS. Most current models of slow slip do not take into account periodic changes in normal stress and for those which incorporate changes in effective normal stress, the results are not in agreement with the observations.

5.2 Future research directions

5.2.1 Multigrid strategies in deconvolution

A major challenge in future work on the blind deconvolution problem will be to improve computational efficiency so that realistic seismograms comprising time series with $10^3 - 10^4$ points can be accommodated. Multigrid methods that work first with large sampling intervals and gradually increase sampling to achieve higher resolution may offer solutions in this regard. The main advantage of this approach lies in the fact that a large part of the computation is made on a smaller system and so fewer points need to be calculated.

5.2.2 Green's function recovery applications

If the blind deconvolution algorithm can be extended to accommodate realistic seismogram lengths (i.e 1000's of points), a key application would be the recovery of P-to-P scattering in the teleseismic P-coda, for example, pure P-reflections from the subducting crust in Cascadia. P-to-P scattering is the only modal interaction with first order sensitivity to compressional modulus (pure S-interactions and conversions are sensitive to shear modulus and density), and hence its characterization would afford independent constraints on the nature (composition, phase, temperature, fluid content) of seismic anomalies. Furthermore, characterization of pure P-scattering at teleseismic frequencies should permit more meaningful comparisons between active and passive datasets, since P-to-P scattering is the primary interaction recorded in seismic reflection profiles.

5.2.3 High resolution detection and location of LFEs using cross-station approaches

A large proportion of stations represented within LFE templates in northern Cascadia display unambiguous zero-phase, impulsive P and S arrivals upon correction to particle displacement. The near-vertical, source-receiver geometries on Vancouver Island and Washington state cause S-wave energy to be strongly excited and to show highly similar waveforms with consistent polarities on the horizontal components across the network. The high coherence of LFE waveforms can be exploited by using cross-station approaches for the detection and location of LFEs and tremor, as proposed by *Rubin and Armbruster* [2013]. As part of her thesis project, my colleague Geneviève Savard has started to develop a cross-station correlation approach based on waveform similarity, causality and multi-channel phase consistency. An initial set of LFE detections is created by using a cross-station algorithm that can be used to identify new LFE templates for network correlation detection. A fine scale relocation across hundreds to thousands of detections and across stations is then established to achieve a resolution of a few hundreds of meters. To date, she is able to resolve different modes of LFE propagation beneath Vancouver Island and Washington such as main slip front propagation to the northwest (except for 2012 for which slip propagates in the southeast direction) at about 5-10 km/day, along strike RTRs with velocities between 5 and 30 km/hr propagating in the reverse direction and streaks of LFEs migrating roughly downdip or updip with velocities of 10's of km/hr. The objective of her follow-up work will be to better map source kinematics during tremor episodes and target specific locations on the plate boundary for construction of waveform templates to be used in studies of structure and physical properties.

5.2.4 Structural studies using LFE templates

The assembly of a large suite of LFE templates can be useful for studies of subduction zone structure focussed for example on scattered waves and S-wave splitting. Recent work of *Nowack and Bostock* [2013] exploits southern Vancouver Island LFE templates as empirical Green's functions to investigate scattered waves in the P- and S-coda from the LVZ. Scattering for near-vertical paths is dominated by converted

$S-$to-P scattering in the P-coda and pure S-to-S scattering in the S-coda. 3D waveform modeling indicates that LFEs are situated <1 km below the top of the LVZ and yields estimates of LVZ thickness, velocity contrast, and V_p/V_s ratios that are consistent with results form teleseismic analyses.

LFE templates display high SNR S-waves that can be used to study crustal anisotropy in the overriding North American plate. Anisotropy refers to properties of a material that differ depending on the direction. When traveling through an anisotropic material, an S-wave is split into 2 distinct pulses, each with a different polarity and velocity. The two main sources of crustal anisotropy are cracks and preferred mineral orientation and so the mapping of anisotropy has become a proxy for the structural geology of a study area. S-wave splitting analysis using high SNR LFE templates from my work at 3-component stations across northern Cascadia indicates the presence of heterogeneous distribution of crustal anisotropy in the North American plate [*Matharu*, 2013].

5.2.5 Tidal modulation of RTRs and streaks and implication for plate boundaries

RTRs and streaks [*Houston et al.*, 2011, *Rubin and Armbruster*, 2013, *Thomas et al.*, 2013] appear to play an important role in tidal modulation of LFEs within tremor episodes as current observations show that RTRs and streaks occur exclusively during times of positive UDSS. Thus it will be important to accurately describe the different modes of migration. A method of selection based on Principal Component Analysis (PCA) has been presented by *Obara et al.* [2012] for this purpose and could be applied to our LFE dataset in northern Cascadia. By using PCA, we might better analyse the multidimensionality (3D space and time) of our LFE catalogues to gain an improved understanding of spatio-temporal interrelationships. PCA transforms the original interrelated variables into a new set of uncorrelated variables call Principal Components (PCs). The objective is to find a coordinate transformation such that the variance of the LFE catalogue along the PC axes is maximized. To extract different modes of migration from LFE catalogues, one might consider different time scales as the main front, RTRs and streaks propagate at different velocities in different directions.

The combination of high resolution mapping of LFEs and PCA analysis in northern Cascadia could improve the quality of RTR and streak characterization considerably and consequently our understanding of the evolution in time and space of LFE sensitivity to tidal stresses.

Bibliography

Abers, G. A., L. S. MacKenzie, S. Rondenay, Z. Zhang, A. G. Wech, and K. C. Creager (2009), Imaging the source region of Cascadia tremor and intermediate-depth earthquakes, *Geology*, *37*, 1119–1122, doi:10.1130/G30143A.1.

Ader, T. J., J.-P. Ampuero, and J.-P. Avouac (2012), The role of velocity-neutral creep on the modulation of tectonic tremor activity by periodic loading, *Geophys. Res. Lett.*, *39*(16), doi:10.1029/2012GL052326.

Agnew, D. C. (2012), SPOTL: Some programs for ocean tide loading, *SIO Tech. Rep. Scripps Inst. Oceanogr.*

Aster, R. C., B. Borchers, and C. H. Thurber (2005), *Parameter estimation and inverse problem*, Elsevier Academic Press.

Audet, P., M. G. Bostock, J.-P. Mercier, and J. F. Cassidy (2008), Morphology of the Explorer-Juan de Fuca slab edge in northern Cascadia: Imaging plate capture at a ridge-trench-transform triple junction, *Geology*, *36*, 895–898, doi:10.1130/G25356A.1.

Audet, P., M. G. Bostock, N. I. Christensen, and S. M. Peacock (2009), Seismic evidence for overpressured subducted oceanic crust and megathrust fault sealing, *Nature*, *457*, 76–78, doi:10.1038/nature07650.

Audet, P., M. G. Bostock, D. C. Boyarko, M. R. Brudzinski, and R. M. Allen (2010), Slab morphology in the Cascadia fore arc and its relation to episodic tremor and slip, *J. Geophys. Res.*, *115*, B00A16, doi:10.1029/2008JB006053.

Bartlow, N. M., D. A. Lockner, and N. M. Beeler (2012), Laboratory triggering of stick-slip events by oscillatory loading in the presence of pore fluid with implications for physics of tectonic tremor, *J. Geophys. Res.*, *117*, B11,411, doi:10.1029/2012JB009452.

Beeler, N. M., and D. A. Lockner (2003), Why earthquakes correlate weakly with the solid Earth tides: effects of periodic stress on the rate and probability of earthquake occurrence, *J. Geophys. Res.*, *108(B8)*, doi:10.1029/2001JB001518.

Beeler, N. M., A. M. Thomas, R. Bürgmann, and D. R. Shelly (2013), Inferring fault rheology from low-frequency earthquakes on the San Andreas, *J. Geophys. Res.*, *118*, 5976–5990, doi:10.1002/2013JB010118.

Booth, D., and S. Crampin (1985), Shear wave polarization on a curved wavefront at an isotropic free surface, *Geophys. J. R. Astron. Soc.*, *83(1)*, 31–45, doi:10.1111/j.1365-246X.1985.tb05154.x.

Bostock, M. G. (2007), Theory and observations-teleseismic body-wave scattering and receiver-side structure, *Seismology and Structure of the Earth, Elsevier*, *1*, 219–246.

Bostock, M. G. (2013), The Moho in subduction zones, *Tectonophysics*, *609*, 547–557, doi:10.1016/j.tecto.2012.07.007.

Bostock, M. G., and N. I. Christensen (2012), Split from slip and schist: Crustal anisotropy beneath northern Cascadia from non-volcanic tremor, *J. Geophys. Res.*, *117*, B08,303, doi:10.1029/2011JB009095.

Bostock, M. G., and J. C. Vandecar (1995), Upper mantle structure of the northern Cascadia subduction zone, *Can. J. Earth Sci.*, *32*, 1–12, doi:10.1139/e95-001.

Bostock, M. G., A. A. Royer, E. H. Hearn, and S. M. Peacock (2012), Low frequency earthquakes below southern Vancouver Island, *Geochem. Geophys. Geosys.*, *13*, 11, doi:10.1029/2012GC004391.

Braunmiller, J., and J. Nabelek (2002), Seismotectonics of the Explorer region, *J. Geophys. Res.*, *107(B10)*, 2208, doi:10.1029/2001JB000220.

Brown, J. R., G. C. Beroza, and D. R. Shelly (2008), An autocorrelation method to detect low frequency earthquakes within tremor, *Geophys. Res. Lett.*, *38*, L16,305, doi:10.1029/2008JL034560.

Burdick, S., C. Li, V. Martynov, T. Cox, J. Eakins, T. Mulder, L. Astiz, F. L. Vernon, G. L. Pavlis, and R. D. van der Hilst (2008), Upper mantle heterogeneity beneath North America from travel time tomography with global and USArray Transportable Array data, *Seismol. Res. Lett.*, *79(3)*, 384–392, doi:10.1785/gssrl.79.3.384.

Buttkus, B. (1975), Homomorphic filtering, theory and practice, *Geophys. Prospect.*, *23(4)*, 712–748, doi:10.1111/j.1365-2478.1975.tb01555.x.

Cadicheanu, N., M. V. Ruymbeke, and P. Zhu (2007), Tidal triggering evidence of intermediate depth earthquakes in the Vrancea zone (Romania), *Nat. Hazards Earth Syst. Sci.*, *7(6)*, 733–740, doi:10.5194/nhess-7-733-2007.

Calkins, J. A., G. A. Abers, G. Ekström, K. C. Creager, and S. Rondenay (2011), Shallow structure of the Cascadia subduction zone beneath western Washington from spectral ambient noise correlation, *J. Geophys. Res.*, *116*, B07,302, doi: 10.1029/2010JB007657.

Cerveny, V., L. Klimes, and I. Psencik (1987), Complete seismic ray tracing in complex 3-D structures, *In: D. Doornbos (Ed.), Seismological Algorithms, Academic Press, N.Y.*, pp. 89–168.

Chu, R., B. Schmandt, and D. V. Helmberger (2012), Juan de Fuca subduction zone from a mixture of tomography and waveform modeling, *J. Geophys. Res.*, *117(B3)*, doi:10.1029/2012JB009146.

Clowes, R. M., M. T. Brandon, A. G. Green, C. J. Yorath, A. S. Brown, E. R. Kanasewich, and C. Spencer (1987), LITHOPROBE- southern Vancouver Island: Cenozoic subduction complex imaged by deep seismic reflections, *Can. J. Earth Sci.*, *24(1)*, 31–51, doi:10.1139/e87-004.

Clowes, R. M., M. T. Brandon, A. G. Green, C. J. Yorath, A. S. Brown, E. R. Kanasewich, and C. Spencer (1990), Deep, high-amplitude refections from a major shear zone above the subducting Juan de Fuca plate, *Geology*, *18*, 1091–1094, doi:10.1130/0091-7613(1990)018⟨1091:DHARFA⟩2.3.CO;2.

Dragert, H., R. D. Hyndman, G. C. Rogers, and K. Wang (1994), Current deformation and the width of the seismogenic zone of the northern Cascadia subduction thrust, *J. Geophys. Res.*, *99*, 653–668, doi:10.1029/93JB02516.

Dragert, H., K. Wang, and T. S. James (2001), A silent slip event on the deeper Cascadia subduction interface, *Science*, *292*, 1525, doi:10.1126/science.1060152.

Enescu, D., and B. D. Enescu (1999), Possible cause-effect relationships between Vrancea (Romania) earthquakes and some global geophysical phenomena, *Nat. Hazards*, *19(2-3)*, 233–245, doi:10.1023/A:1008095708316.

Farrell, W. E. (1972), Deformation of the Earth by surface loads, *Rev. Geophys. Space. Phys.*, *10(3)*, 761–797, doi:10.1029/RG010i003p00761.

Frank, W., N. M. Shapiro, V. Kostoglodov, A. L. Husker, M. Campillo, J. S. Payero, and G. A. Prieto (2013), Low-frequency earthquakes in the Mexican sweet spot, *Geophys. Res. Lett.*, *40*, 2661–2666, doi:10.1002/grl.50561.

Gallego, A., R. M. Russo, D. Comte, V. Mocanu, R. E. Murdie, and J. C. VanDecar (2013), Tidal modulation of continuous nonvolcanic seismic tremor in the Chile triple junction region, *Geochem. Geophys. Geosyst.*, *14*(4), 851–863, doi:10.1002/ggge.20091.

Ghosh, A., J. E. Vidale, J. Sweet, K. C. Creager, A. Wech, H. Houston, and E. Brodsky (2010), Rapid, continuous streaking of tremor in Cascadia, *Geochem. Geophys. Geosys.*, *11*, Q12,010, doi:10.1029/2010GC003305.

Ghosh, A., J. E. Vidale, and K. C. Creager (2012), Tremor asperities in the transition zone control evolution of slow earthquakes, *J. Geophys. Res.*, *117*, B10,301, doi:10.1029/2012JB009249.

Gibbons, S. J., and F. Ringdal (2006), The detection of low magnitude seismic events using array-based waveform correlation, *Geophys. J. Int.*, *165*, 149–166, doi:10.1111/j.1365-246X.2006.02865.x.

Gogonenkov, G. N. (1990), Seismic prospecting for sedimentary formations, *A.A. Balkema - Russian Translation Series*, *76*, 219.

Golub, G. H., and V. Pereyra (1973), The differenciation of pseudo-inverses and nonlinear least squares problems whose variables separate, *SIAM J. Numer. Anal.*, *10(2)*, 413–432, doi:10.1137/0710036.

Golub, G. H., and V. Pereyra (2003), Separable nonlinear least squares: the variable projection method and it applications, *Inverse Problems*, *Vol 19*, R1–R26, doi:10.1088/0266-5611/19/2/201.

Gomberg, J., and S. Prejean (2013), Triggered tremor sweet spots in Alaska, *J. Geophys. Res.*, *118*, 6203–6218, doi:10.1002/2013JB010273.

Green, A. G., R. M. Clowes, C. J. Yorath, C. Spencer, E. R. Kanasewish, M. T. Brandon, and A. S. Brown (1986), Seismic reflection imaging of the subducting Juan de Fuca plate, *Nature*, *319(6050)*, 210–213, doi:10.1038/319210a0.

Hansen, P. C. (1998), *Rank-deficient and discrete III-posed problems: numerical aspects of linear inversion*, vol. 4, SIAM Monogr. Math. Model. Comput., doi:10.1137/1.9780898719697.

Hansen, R. T. J., M. G. Bostock, and N. I. Christensen (2012), Nature of the low velocity zone in Cascadia from receiver function waveform inversion, *Earth Planet. Sci. Lett.*, *337-338*, 25–38, doi:10.1016/j.epsl.2012.05.031.

Hawthorne, J. C., and A. M. Rubin (2010), Tidal modulation of slow slip in Cascadia, *J. Geophys. Res.*, *115*, B09,406, doi:10.1029/2010JB007502.

Hawthorne, J. C., and A. M. Rubin (2013), Tidal modulation and back-propagating fronts in slow slip events simulated with a velocity-weakening to velocity-strenghtening friction law, *J. Geophys. Res.*, *118*, 1216–1239, doi:10.1002/jgrb.50107.

Houston, H. (2013), ETS and tidal stressing: Fault weakening after the main slip pulse, *EOS Trans. Am. Geophys. U., presented at 2013 Fall Meeting AGU, San Francisco, Calif. 9-13 Dec.*

Houston, H., B. G. Delbridge, A. G. Wech, and K. C. Creager (2011), Rapid tremor reversals in Cascadia generated by a weakened plate interface, *Nature Geosci.*, *4*, 404–409, doi:10.1038/ngeo1157.

Husker, A. L., V. M. Cruz-Atienza, D. Legrand, N. M. Shapiro, J. Payero, M. Campillo, and E. Huesca-Pérez (2012), Temporal variations of non−volcanic tremor (NVT)

locations in the Mexican subduction zone: finding the NVT sweet spot, *Geochem. Geophys. Geosys.*, *13*, Q03,011, doi:10.1029/2011GC003916.

Ide, S. (2010), Striations, duration, migration and tidal response in deep tremor, *Nature*, *466(7304)*, 356–9, doi:10.1038/nature09251.

Ide, S., D. R. Shelly, and G. C. Beroza (2012), Mechanism of deep low frequency earthquakes: further evidence that deep non-volcanic tremor is generated by shear slip on the plate interface, *Geophys. Res. Lett.*, *34*, L03,308, doi:10.1029/2006GL028890.

Kao, H., S.-J. Shan, H. Dragert, G. Rogers, J. F. Cassidy, and K. Ramachandran (2005), A wide depth distribution of seismic tremors along the northern Cascadia margin, *Nature*, *436*, 841–844, doi:10.1038/nature03903.

Kao, H., S. J. Shan, H. Dragert, and G. Rogers (2009), Northern Cascadia episodic tremor and slip: a decade of tremor observations from 1997 to 2007, *J. Geophys. Res.*, *114*, B00A12, doi:10.1029/2008JB006046.

Kikuchi, M., and H. Kanamori (1991), Inversion of complex body waves - III, *Bull. Seismol. Soc. Am.*, *81*, 2335–2350.

Klaus, A. (2012), Modulation of Cascadia tremor amplitude by tidal stresses, *MSc thesis, University of Washington.*

Klein, F. W. (2002), User's guide to Hypoinverse-2000, a FORTRAN program to solve for earthquake locations and magnitudes, *U.S. Geol. Surv.*, *Open File Rep.*, 02–171.

Knopoff, L. (1964), Earth tides as a triggering mechanism for earthquakes, *Bull. Seismol. Soc. Am.*, *54(6)*, 1865–1870.

Kumar, P., R. Kind, and X. Yuan (2010), Receiver function summation without deconvolution, *Geophys. J. Int.*, *180*, 1223–1230, doi:10.1111/j.1365-246X.2009.04469.x.

Kurtz, R. D., J. M. Delaurier, and J. C. Gupta (1990), The electrical conductivity distribution beneath vancouver island: a region of active plate subduction, *J. Geophys. Res.*, *95(B7)*, 10,929–10,946, doi:10.1029/JB095iB07p10929.

Lambert, A., H. Kao, G. Rogers, and N. Courtier (2009), Correlation of tremor activity with tidal stress in the northern Cascadia subduction zone, *J. Geophys. Res.*, *114*, B00A08, doi:10.1029/2008JB006038.

Langston, C. S. (1977), The effect of planar dipping structure on source and receiver responses for constant ray parameter, *Bull. Seism. Soc. Am.*, *67*, 1029–1050, doi: 10.1/1.128.7468.

Langston, C. S. (1981), Evidence for the subducting lithosphere under southern Vancouver Island and western Oregon from teleseismic P wave conversions, *J. Geophys. Res.*, *86*, 3857–3866, doi:10.1029/JB086iB05p038578.

Liu, Y., and J. R. Rice (2007), Spontaneous and triggered aseismic deformation transients in a subduction fault model, *J. Geophys. Res.*, *112(B9)*, doi:10.1029/ 2007JB004930.

Liu, Y., and J. R. Rice (2009), Slow slip predictions based on granite and gabbro friction data compared to GPS measurements in northern Cascadia, *J. Geophys. Res.*, *114(B9)*, doi:10.1029/2008JB006142.

Lockner, D. A., and N. M. Beeler (1999), Premonitory slip and tidal triggering of earthquakes, *J. Geophys. Res.*, *104(B9)*, 20,133–20,151, doi:10.1029/1999JB900205.

Marone, C. (1998), Laboratory-derived friction laws and their application to seismic faulting, *Annu. Rev. Earth Planet. Sci.*, *26(1)*, 643–696, doi:10.1146/annurev.earth. 26.1.643.

Matharu, G. (2013), Crustal anisotropy in a subduction zone forearc: Northern Cascadia, *M.sc. Thesis, University of British Columbia*.

Mazzucchelli, P., and P. Spagnolini (2001), Least-square multichannel deconvolution, *Eage*, *55(7)*, 169.

McCaffrey, R. A. A. Q., R. King, R. Wells, G. Khazaradze, C. Williams, C. Stevens, J. Vollick, and P. Zwick (2007), Fault locking, block rotation and crustal deformation in the Pacific Northwest, *Geophys. J. Int.*, *169*, 1315–1340, doi:10.1111/j.1365-246X. 2007.03371.x.

McCrory, P. A., J. L. Blair, F. Waldhauser, and D. H. Oppenheimer (2012), Juan de Fuca slab geometry and its relation to Wadati-Benioff zone seismicity, *J. Geophys. Res.*, *117*, B09,306, doi:10.1029/2012JB009407.

Melchior, P. (1978), The tides of the planet Earth, *Pergamon, Oxford, UK*.

Mercier, J.-P., M. G. Bostock, J. F. Cassidy, K. Duefer, J. B. Gaherty, E. J. Garnero, J. Revenaugh, and G. Zandt (2009), Body-wave tomography of western Canada, *Tectonophysics*, *475*, 480–492, doi:10.1016/j.tecto.2009.05.030.

Michaelson, C. A., and C. S. Weaver (1986), Upper mantle structure from teleseismic P wave arrivals in Washington and northern Oregon, *J. Geophys. Res.*, *91*, 2077–2094, doi:10.1029/JB091iB02p02077.

Miller, M. M., T. Melbourne, D. J. Johnson, and W. Q. Summer (2002), Periodic slow earthquakes from the Cascadia subduction zone, *Science*, *295(5564)*, 2423, doi: 10.1126/science.1071193.

Miyazawa, M., and J. Mori (2005), Detection of triggered deep low frequency events from the 2003 Tokachi-oki earthquake, *Geophys. Res. Lett.*, *32*, L10,307, doi:10.1029/ 2005GL022539.

Nakata, R., N. Suda, and H. Tsuruoka (2008), Non−volcanic tremor resulting from the combined effect of Earth tides and slow slip events, *Nature Geosci.*, *1*, 676–678, doi:10.1016/j.tecto.2005.09.013.

Nowack, R. L., and M. G. Bostock (2013), Scattered waves from low frequency earthquakes and plate boundary structure in northern Cascadia, *Geophys. Res. Lett.*, *40*, 4238–4243, doi:10.1002/grl.50826.

Obara, K. (2002), Nonvolcanic deep tremor associated with subduction in southwest Japan, *Science*, *296*, 1679–1681, doi:10.1126/science.1070378.

Obara, K., T. Matsuzawa, S. Tanaka, and T. Maeda (2012), Depth-dependent mode of tremor migration beneath Kii Peninsula, Nankai subduction zone, *Geophys. Res. Lett.*, *39*(10), doi:10.1029/2012GL051420.

Obrebski, M., R. M. Allen, F. Pollitz, and S.-H. Hung (2011), Lithosphere–asthenosphere interaction beneath the western United States from the joint inversion of body-wave travel times and surface-wave phase velocities, *Geophys. J. Int.*, *185(2)*, 1003–1021, doi:10.1111/j.1365-246X.2011.04990.x.

Paterson, M. S., and T.-F. Wong (2005), *Experimental Rock Deformation-The Brittle Field (2nd ed)*, 347 pp., Springer, New York.

Peng, Z., and K. Chao (2008), Non−volcanic tremor beneath the Central Range in Tawain triggered by the 2001 M_w 7.8 Kunlun earthquake, *Geophys. J. Int.*, *175*, 825–829, doi:10.1111/j.1365-246X.2008.03886.x.

Peng, Z., J. E. Vidale, K. C. Creager, J. L. Rubinstein, J. Gomberg, and P. Bodin (2008), Strong tremor near Parkfield, CA, excited by the 2002 Denali Fault earthquake, *Geophys. Res. Lett.*, *35*, L23,305, doi:10.1029/2008GL036080.

Perfettini, H., J. Schmittbuhl, J. R. Rice, and M. Cocco (2001), Frictional response induced by time-dependent fluctuations of the normal loading, *J. Geophys. Res.*, *106(B7)*, 13,455–13,472, doi:10.1029/2000JB900366.

Rasmussen, J., and E. Humphreys (1988), Tomographic image of the Juan de Fuca plate beneath Washington and western Oregon using teleseismic P-wave travel times, *Geophys. Res. Lett.*, *15*, 1417–1420, doi:10.1029/GL015i012p01417.

Rietsch, E. (1997a), Euclid and the art of wavelet estimation, Part 1: Basic algorithm for noise free data, *Geophysics*, *62(6)*, 1931–1938, doi:10.1190/1.1444293.

Rietsch, E. (1997b), Euclid and the art of wavelet estimation, Part 2: Robust algorithm and field data examples, *Geophysics*, *62(6)*, 1939–1946, doi:10.1190/1.1444294.

Rogers, G., and H. Dragert (2003), Episodic tremor and slip on the Cascadia subduction zone: the chatter of silent slip, *Science*, *300(5627)*, 1942–1943, doi:10.1126/science.1084783.

Rowe, C. A., R. C. Aster, B. Borchers, and C. J. Young (2002), An automatic, adaptive algorithm for refining phase picks in large seismic data sets, *Bull. Seismol. Soc. Am.*, *92*, 1660–1674, doi:10.1785/0120010224.

Royer, A. A., and M. G. Bostock (2013), A comparative study of low frequency earthquake templates in northern Cascadia, *Earth Planet. Sci. Lett.*, doi:10.1016/j.epsl.2013.08.040.

Rubin, A. M. (2011), Designer friction laws for bimodal slow slip propagation speeds, *Geochem. Geophys. Geosyst.*, *12(4)*, doi:10.1029/2010GC003386.

Rubin, A. M., and J. G. Armbruster (2013), Imaging slow slip fronts in Cascadia with high precision cross-station tremor locations, *Geochem. Geophys. Geosys.*, *14*, doi:10.1002/2013GC005031.

Rubinstein, J. L., J. E. Vidale, J. Gomberg, P. Bodin, K. C. Creager, and S. D. Malone (2007), Non−volcanic tremor driven by large transient shear stresses, *Nature*, *448*, 579–582, doi:10.1038/nature06017.

Rubinstein, J. L., M. L. Rocca, J. E. Vidale, K. C. Creager, and A. G. Wech (2008), Tidal modulation of nonvolcanic tremor, *Science*, *319*, 186, doi:10.1126/science.1150558.

Rubinstein, J. L., J. Gomberg, J. E. Vidale, A. G. Wech, H. Kao, K. C. Creager, and G. Rogers (2009), Seismic wave triggering of nonvolcanic tremor, episodic tremor and slip, and earthquakes on Vancouver Island, *J. Geophys. Res.*, *114*, B00A01, doi:10.1029/2008JB005875.

Rydelek, P. A., and I. S. Sacks (1989), Testing the completeness of earthquake catalogues and the hypothesis of self-similarity, *Nature*, *337*, 251–253, doi:10.1038/337251a0.

Rydelek, P. A., I. S. Sacks, and R. Scarpa (1992), On tidal triggering of earthquakes at Campi Flegrei, Italy, *Geophys. J. Int.*, *109(1)*, 125–135, doi:10.1111/j.1365-246X.1992.tb00083.x.

Sacchi, M. D., and T. J. Ulrych (2000), Nonminimum-phase wavelet estimation using higher order statistics, *The Leading Edge*, *19(1)*, 80–83, doi:10.1190/1.1438466.

Schmidt, D. A., and H. Gao (2010), Source parameters and time-dependent slip distributions of slow slip events on the Cascadia subduction zone from 1998 to 2008, *J. Geophys. Res.*, *115(B4)*, doi:10.1029/2008JB006045.

Schuster, A. (1897), On lunar and solar periodicities of earthquakes, *Proc. R. Soc. Lond.*, *61*, 455–465, doi:10.1098/rspl.1897.0060.

Shearer, P. M. (1991), Imaging global body wave phases by stacking long-period seismograms, *J. Geophys. Res.*, *96*, 20,353–20,364, doi:10.1029/91JB00421.

Shelly, D. R., and J. L. Hardebeck (2010), Precise tremor source locations and amplitude variations along the lower-crustal central San Andreas Fault, *Geophys. Res. Lett.*, *37*, L14,301, doi:10.1029/i2010GL043672.

Shelly, D. R., G. C. Beroza, S. Ide, and S. Nakamura (2006), Low-frequency earthquakes in Shikoku, Japan, and their relationship for episodic tremor and slip, *Nature*, *442*, 188–191, doi:10.1038/nature04931.

Shelly, D. R., G. C. Beroza, and S. Ide (2007), Non-volcanic tremor and low-frequency earthquakes swarms, *Nature*, *446*, 305–307, doi:10.1038/nature05666.

Shudde, R. H., and D. R. Barr (1977), An analysis of earthquake frequency data, *Bull. Seismol. Soc. Am.*, *67(5)*, 1379–1386.

Simpson, J. F. (1967), Earth tides as a triggering mechanism for earthquakes, *Earth Planet. Sci. Lett.*, *2(5)*, 473–478, doi:10.1016/0012-821X(67)90192-6.

Soyer, W., and M. Unsworth (2006), Deep electrical structure of the northern Cascadia (British Columbia, canada) subduction zone: Implications for the distribution of fluids, *Geology*, *34(1)*, 53–56, doi:10.1130/G21951.1.

Stavinschi, M., and J. Souchay (2003), Some correlations between earthquakes and Earth tides, *Acta Geod. Geoph. Hung.*, *38(1)*, 77–92, doi:10.1556/AGeod.38.2003.1.

Szeliga, W., T. I. Melbourne, M. Santillan, and M. Miller (2008), GPS constraints on 34 slow slip events within the Cascadia subduction zone, 1997-2005, *J. Geophys. Res.*, *113(B4)*, doi:10.1029/2007JB004948.

Tanaka, S., M. Ohtake, and H. Sato (2002), Evidence for tidal triggering of earthquakes as revealed from statistical analysis of global data, *J. Geophys. Res.*, *107(B10)*, 2211, doi:10.1029/2001JB001577.

Tanaka, S., H. Sato, S. Matsumura, and M. Ohtake (2006), Tidal triggering of earthquakes in the subducting Philippine sea plate beneath the locked zone of the plate interface in the Tokai region, Japan, *Tectonophysics*, *417(1–2)*, 69 – 80, doi: 10.1016/j.tecto.2005.09.013.

Thomas, A. M., R. M. Nadeau, and R. Burgmann (2009), Tremor-tide correlations and near-lithostatic pore pressure on the deep San Andreas fault, *Nature*, *462*, 1048–1051, doi:10.1038/nature08654.

Thomas, A. M., R. Bürgmann, D. R. Shelly, N. M. Beeler, and M. L. Rudolph (2012), Tidal triggering of low frequency earthquakes near Parkfield, California: Implications for fault mechanics within the brittle-ductile transition, *J. Geophys. Res.*, *117*, B05,301, doi:10.1029/2011JB009036.

Thomas, T. W., J. E. Vidale, H. Houston, K. C. Creager, J. R. Sweet, and A. Ghosh (2013), Evidence for tidal triggering of high-amplitude rapid tremor reversals and tremor streaks in northern Cascadia, *Geophys. Res. Lett.*, *40*, 4254–4259, doi:10.1002/grl.50832.

Tribolet, J. M. (1978), Applications of short-time homomorphic signal analysis to seismic wavelet estimation, *Geoexploration*, *16(1–2)*, 75 – 96, doi:10.1016/0016-7142(78)90008-X.

Ulrych, T. J. (1971), Application of homomorphic deconvolution to seismology, *Geophysics*, *36(4)*, 650, doi:10.1190/1.1440202.

Vidale, J. E., D. C. Agnew, M. J. S. Johnston, and D. H. Oppenheimer (1998), Absence of earthquake correlation with Earth tides: an indication of high preseismic fault stress rate, *J. Geophys. Res.*, *103(B10)*, 24,567–24,572, doi:10.1029/98JB00594.

Vinnik, L. P. (1977), Detection of waves converted from P to SV in the mantle, *Phys. Earth Planet. Inter.*, *15(1)*, 39–45, doi:10.1016/0031-9201(77)90008-5.

Waldhauser, F. (2001), HypoDD_A program to compute double-difference hypocenter locations, *U.S. Geol. Surv.*, *Open File Rep.*, 01–113.

Wang, K., H. Dragert, and H. J. Melosh (1994), Finite element study of uplift and strain across Vancouver Island, *Can. J. Earth Sci.*, *31*, 1510–1522, doi:10.1139/e94-134.

Wech, A., K. C. Creager, and T. I. Merlbourne (2009), Seismic and geodetic constraints on Cascadia slow slip, *J. Geophys. Res.*, *114*, B10,316, doi:10.1029/2008JB006090.

Wech, A. G., and K. C. Creager (2007), Cascadia tremor polarization evidence for plate interface slip, *Geophys. Res. Lett.*, *34*, L22,306, doi:10.1029/2007GL031167.

Wech, A. G., and K. C. Creager (2008), Automated detection and location of Cascadia tremor, *Geochem. Geophys. Geosys.*, *35*, L20,302, doi:10.1029/2008GL035458.

Wech, A. G., and K. C. Creager (2011), A continuum of stress, strength and slip in the Cascadia subduction zone, *Nature Geosci.*, *4*, 624–628, doi:10.1038/ngeo1215.

Weglein, A. B., and B. G. Secrest (1990), Wavelet estimation for a multidimensional acoustic or elastic earth, *Geophysics*, *55(7)*, 902–913, doi:10.1190/1.1442905.

Appendix A

Supplementary material for Chapter 3

The supplementary material contains a table and 4 figures that support the analysis and interpretation of low frequency earthquake (LFE) templates presented in the text. Table A1 presents the parameters employed in double-difference travel-time inversion for LFE locations. LFE epicentres from double-difference travel-time inversion are plotted in figure A1. Figure A2 plots depth profiles of LFE hypocentres determined using Hyp2000. Condition numbers for inverse system employed in moment tensor inversion are shown in figure A3 whereas figure A4 displays histograms of strike, dip and rake of LFEs assuming shallower nodal plane is fault plane. All citations appear in main reference list.

IDAT	NITER	WTCCP	WTCCS	WRCC	WDCC	WTCTP	WTCTS	WRCT	WDCT	DAMP
3	8	0.01	0.01	-9	-9	1	1	-9	-9	50
	8	0.01	0.01	-9	-9	1	1	-9	8	50
	8	1	1	-9	2	0.01	0.01	6	8	40
	8	1	1	5	2	0.01	0.01	6	8	40
	8	1	1	5	0.5	0.01	0.01	6	8	40

TABLE A.1: Parameters employed in hypoDD inversion. We use both catalog data and cross-correlation data through 40 iterations. IDAT: Data type. In our case, 3 means that we use both catalog and cross-correlation data. NITER: Number of iterations with the setting parameters. WTCCP, WTCCS: Weights for *P*-wave, *S*-wave cross-correlation data. WRCC, WRCT: Cutoff threshold for outliers located on the tails of the cross-correlation,catalog data. WDCC, WDCT: Maximum event separation distance [km] for cross-correlation data, catalog data. WTCTP,WTCTS: Weights for catalog *P*-wave, *S*-wave data. DAMP: Damping factor for least-squares solution.

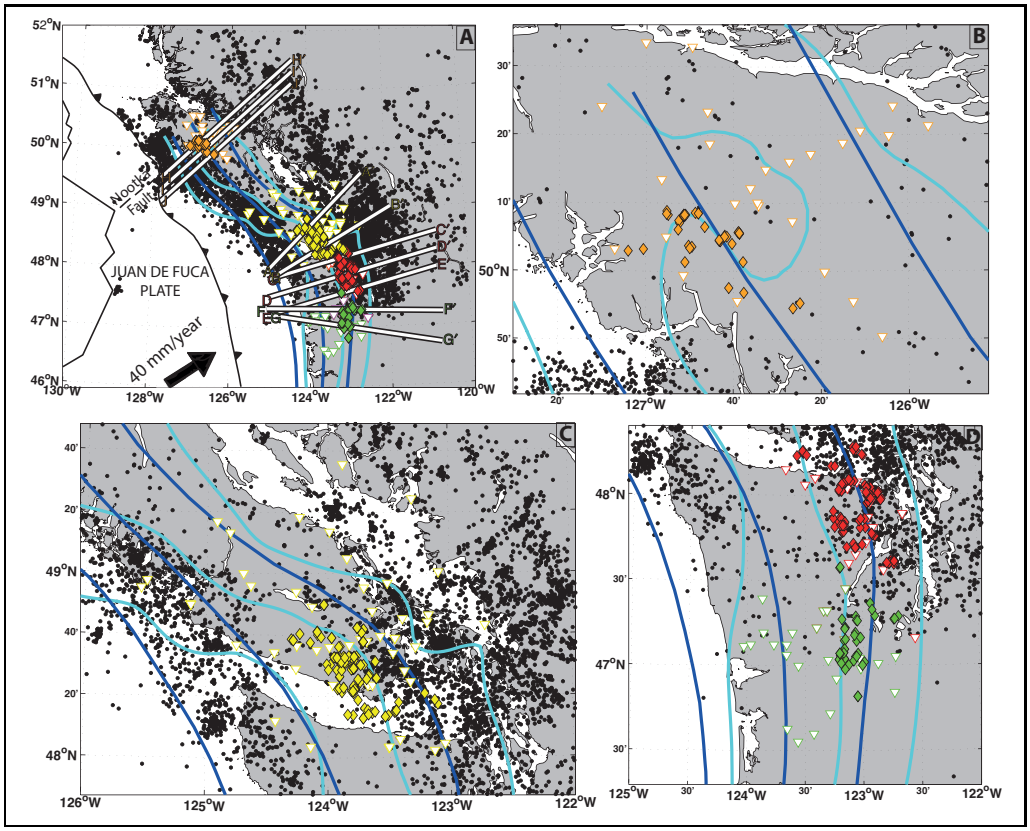

FIGURE A.1: Map of LFE locations from hypoDD inversion. Orange, red and green diamonds are LFE locations for the NVI, NW and SW datasets, respectively. Yellow diamonds are locations of LFEs in southern Vancouver Island determined by Bostock et al (2012). Cyan and blue lines indicate the 20, 30 and 40km depth contours to the top of the subducting Juan de Fuca pate modeled by Audet et al (2010) and McCrory et al (2012), respectively.

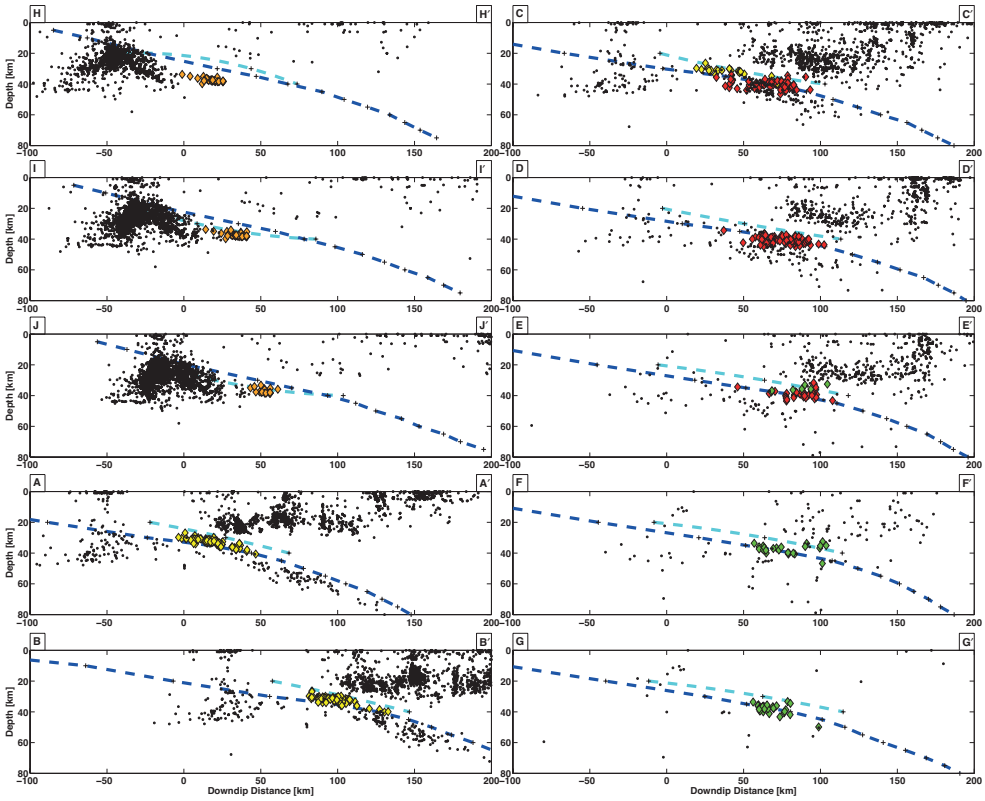

FIGURE A.2: Depth profiles A-A' to J-J' of seismicity in northern Cascadia. Black dots represent regular earthquake locations for the period 1985-2012. Orange, yellow, red and green diamonds are LFE locations from Hyp2000 inversion for NVI, SVI, NW and SW datasets, respectively. Dashed cyan and blue lines represent estimates of the subducting Juan de Fuca plate from the Audet et al (2010) and McCrory et al (2012) models, respectively.

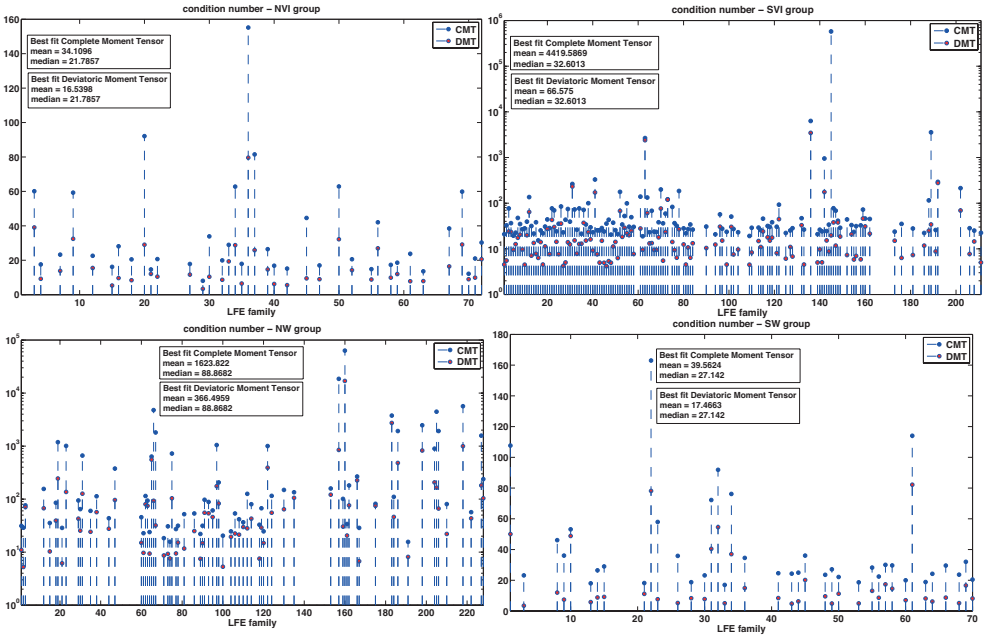

FIGURE A.3: Condition number of the symmetric matrix that enters the normal equations in moment tensor inversion.

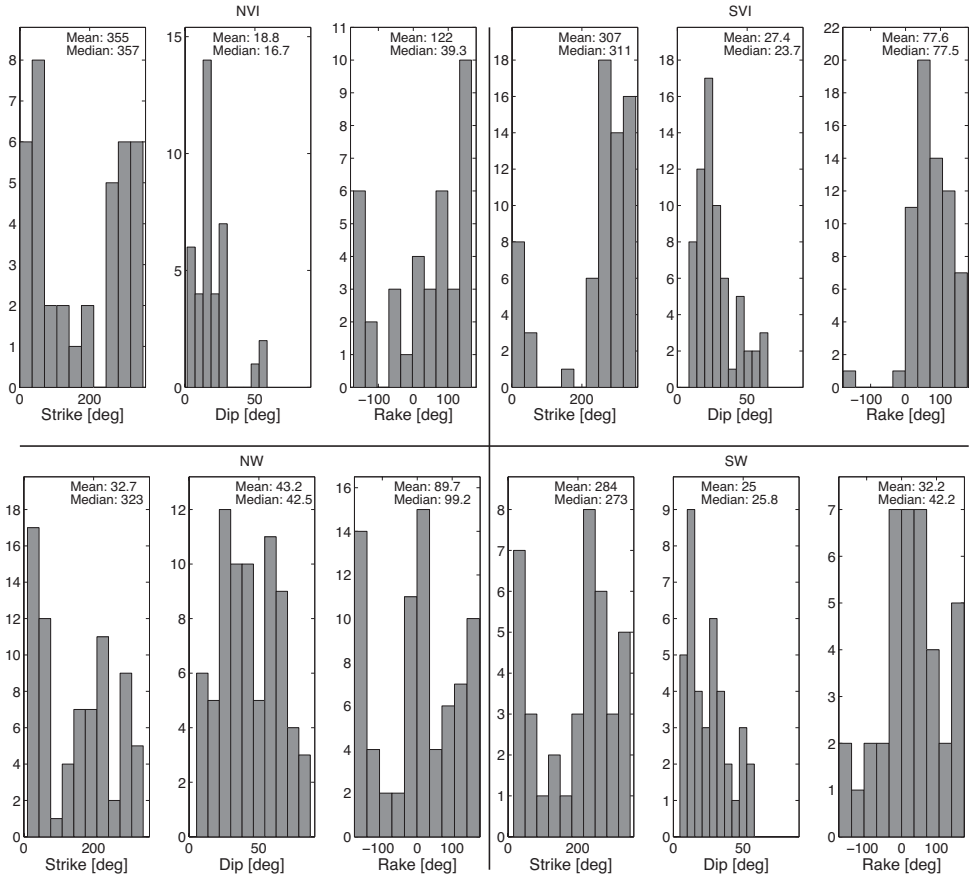

FIGURE A.4: Histograms of strike, dip and rake distribution from moment tensor inversion for NVI, SVI ,NW and SW groups.

Appendix B

Supplementary material for Chapter 4

The supplementary material contains a table and a figure that support the analysis and interpretation of tidal modulation of low frequency earthquakes (LFEs) presented in the text. Table B1 summarizes tidally induced up-dip shear stress (UDSS) and fault normal stress (FNS) N_{ex} values for Rapid Tremor Reversals (RTRs) and non-RTR events for each LFE family in southern Vancouver Island. Figure B1 plots hypothesis testing results with the null hypothesis that LFEs are influenced by FNS component only. For the complete methodology, see *Thomas et al.* [2012].

# LFE	UDSS Nex (%)	FNS Nex (%)	# of detections	% of RTRs	UDSS Nex RTR (%)	UDSS Nex non-RTR (%)	FNS Nex RTR (%)	FNS Nex non-RTR (%)
1	55.65	-76	413	0	NaN	55.65	NaN	-76
2	19.07	-11.8	1156	0	NaN	19.07	NaN	-11.8
3	20.71	-30.96	1335	0	NaN	20.71	NaN	-30.96
4	20.28	-25.91	1043	2.11	83.33	18.93	-100	-24.36
5	26.06	-27.93	1687	0.47	100	25.87	-100	-27.63
6	23.75	8.07	1181	0.68	100	23.23	-100	8.88
7	25.83	-19.75	936	2.99	86.67	24.24	-100	-17.23
8	5.95	-7.17	1089	0.55	100	5.43	-100	-6.78
9	-14.75	-14.12	402	3.73	-50	-13.4	83.33	-17.68
10	-8.91	-13.4	1374	8.01	-3.33	-9.39	10.64	-15.51
11	3.96	5.62	1637	8.74	40.26	0.50	-42.62	10.27
12	4.72	11.06	1023	6.84	47.37	1.56	-53.33	15.84
13	11.08	-21.96	599	20.37	74.24	-5.02	-90.38	-4.43
14	11.36	11.41	1261	10.23	-9.23	13.71	26.32	9.72
15	-1.78	7.69	1031	2.52	-30.77	-1.01	16.67	7.69
16	5.71	-13.56	744	13.98	80.36	-6.07	-79.55	-2.57
17	7.37	-9.62	1533	10.44	25.32	5.29	-10.67	-9.5
18	-2.96	-27.89	1088	9.93	46.3	-8.42	-38	-26.77
19	3.85	9.43	1118	2.42	-7.69	4.14	84.62	7.54
20	-0.88	-30.73	1146	12.57	30.99	-5.25	-28.36	-30.92
21	0.16	-10.46	1264	12.18	27.63	-3.64	-11.11	-10.36
22	7.35	-12.3	1597	18.28	55.19	-3.34	-69.6	0.54
23	4.92	-5.62	1008	11.41	18.97	3.11	-27.45	-2.79
24	-8.68	-30.88	668	8.83	78.13	-17.48	-88	-25.38

# LFE	UDSS Nex (%)	FNS Nex (%)	# of detections	% of RTRs	UDSS Nex RTR (%)	UDSS Nex non-RTR (%)	FNS Nex RTR (%)	FNS Nex non-RTR (%)
25	14.52	-10.65	1303	8.21	92.73	7.5	-36.96	-8.45
26	1.47	-4.32	1322	27.46	43.32	-14.57	-68.55	20
27	-2.69	-17.89	609	6.73	-75	2.53	-31.58	-16.92
28	-7.27	-26.89	563	2.31	-50	-5.97	-33.33	-26.74
29	28.83	-16.9	1683	9.98	63.86	24.93	0	-18.9
30	14.84	-7.13	1944	25.62	50.98	2.43	-60.73	11.3
31	20.96	-18.12	1366	30.01	66.5	1.46	-22.58	-16.4
32	12.64	-27.81	354	5.37	100	8.54	-100	-23.78
33	31.12	-16.61	1816	34.36	68.06	11.8	-15.28	-17.3
34	22.14	-8.22	813	31	71.65	0	-23.89	-1.19
35	21.82	-44.11	925	12.43	64.52	15.7	-72	-40.11
36	12.25	-37.04	1127	11.18	56.72	6.9	-87.04	-30.79
37	30.76	-14	1749	34.31	67.11	11.56	-7.94	-17.17
38	28.25	-18.85	1993	31.21	67.31	10.56	-20.21	-18.35
39	32.28	-24.27	1781	33.24	65.42	15.54	-16.12	-28.47
40	20.63	-12.81	1145	31.44	66.29	-0.26	-12.57	-12.91
41	4.03	-8.25	989	11.12	89.66	-6.7	-48.94	-3.18
42	24.03	-46.35	921	12.6	67.74	17.72	-76	-42.07
43	9.46	-40.04	1317	18.45	71.32	-4.57	-79.05	-31.17
44	34.77	-15.17	1962	27.32	80.83	17.49	-13.36	-15.85
45	14.78	-42.41	1100	18	77.14	1.05	-75.29	-35.05
46	5.83	-22.13	813	5.04	95.24	1.02	-94.44	-18.18
47	23.21	-23.12	1117	15.76	68.89	14.94	-37.18	-20.48
48	33.33	-4.3	1802	33.02	75.09	12.77	6.14	-9.45

# LFE	UDSS Nex (%)	FNS Nex (%)	# of detections	% of RTRs	UDSS Nex RTR (%)	UDSS Nex non-RTR (%)	FNS Nex RTR (%)	FNS Nex non-RTR (%)
49	37.59	-9.48	1883	21.83	91.83	22.49	-4.84	-10.78
50	28.62	9.59	1217	17.75	86.79	15.75	-8	13.39
51	35.91	-7.46	1710	23.27	87.62	20.18	7.18	-11.91
52	40.77	-2.46	1842	21.66	88.38	27.62	33.51	-12.57
53	37.86	-5.79	2012	20.23	87.38	25.28	12.43	-10.27
54	35.38	-2.79	1316	23.78	91.61	17.54	22.76	-10.75
55	44.65	1.12	983	21.26	98.1	30.59	13.68	-2.27
56	24.62	-1.45	2547	20.42	78.82	10.85	15.42	-5.78
57	23.94	-2.33	1582	21.93	74.12	10.07	18.75	-8.25
58	18.6	-10.77	691	7.81	74.07	13.88	-52.17	-7.3
59	20.55	-29.16	1754	20.24	90.16	2.91	-39.24	-26.6
60	38.27	-30.12	583	2.74	87.5	36.8	57.14	-32.64
61	12.2	-11	2098	10.82	92.37	2.47	-73	-3.39
62	9.32	-6.73	2955	10.52	91.98	-0.44	-69.57	0.68
63	40.93	6.69	1649	16.01	98.47	29.93	56.56	-2.81
64	21.07	-8.58	701	7.28	73.08	16.97	-40.91	-6.05
65	35.5	-6.19	1066	17.26	92.47	23.6	-4.76	-6.48
66	35.24	-7.81	1411	16.3	93.1	24.25	-9.62	-7.46
67	34.83	39.49	366	2.19	100	33.33	0	41.18
68	22.98	52.68	522	0	NaN	22.98	NaN	52.68
69	9.46	-9.55	812	8.25	85.71	2.58	-10.34	-9.48
70	24.31	15.22	962	2.29	90.91	22.73	11.11	15.59
71	21.7	-17.95	869	9.55	46.51	18.77	-13.51	-18.18
72	36.35	8.06	1380	14.64	100	25.47	6.45	8.33

# LFE	UDSS Nex (%)	FNS Nex (%)	# of detections	% of RTRs	UDSS Nex RTR (%)	UDSS Nex non-RTR (%)	FNS Nex RTR (%)	FNS Nex non-RTR (%)
73	33.89	5.37	1917	12.36	96.58	25.09	19.44	3.39
74	25.42	-1.98	1437	11.48	101.22	15.37	22.67	-5.16
75	37.23	15.18	1396	11.1	98.72	29.53	0	17.08
76	15.61	0	1324	8.46	100	7.78	-11.76	1.09
77	18.6	4.89	1524	0	NaN	18.6	NaN	4.89
78	18.49	6.99	1427	0	NaN	18.49	NaN	6.99
79	21.31	-25.33	1365	8.06	75.44	16.54	-4.17	-27.17
80	33.16	4.01	1538	22.04	60.92	25.08	-32.47	14.31
81	26.38	-3.44	1666	20.95	54.4	18.95	-3.16	-3.51
82	15.36	-12.3	1136	13.29	55	9.04	-25	-10.36
83	14	-4.47	1300	14.54	66.34	5.07	-40	1.61
84	8.73	-14.95	1874	7.95	61.04	4.24	-33.85	-13.21
85	12.22	-13.93	891	14.93	62.5	3.41	-25	-11.99
86	12.07	-1.73	1611	0	NaN	12.07	NaN	-1.73
87	3.81	-16.5	1833	9.93	42.71	-0.46	-35.8	-14.48
88	13.82	-7.38	1570	13.44	64.1	5.99	-34.74	-3.27
89	18.95	-4.53	1754	19.27	52.17	11.02	-35.29	2.81
90	5.22	-18.09	1984	9.53	42.31	1.31	-39.29	-15.95
91	16.67	-6.92	1215	15.97	44.95	11.3	-28.41	-2.82
92	14.27	-18.82	1678	15.32	56.55	6.62	-43.97	-14.15
93	16.36	-15.48	2062	8.73	57.14	12.34	-59.26	-11.31

TABLE B.1: UDSS and FNS N_{ex} values for RTRs and non-RTR events for each LFE family in southern Vancouver Island.

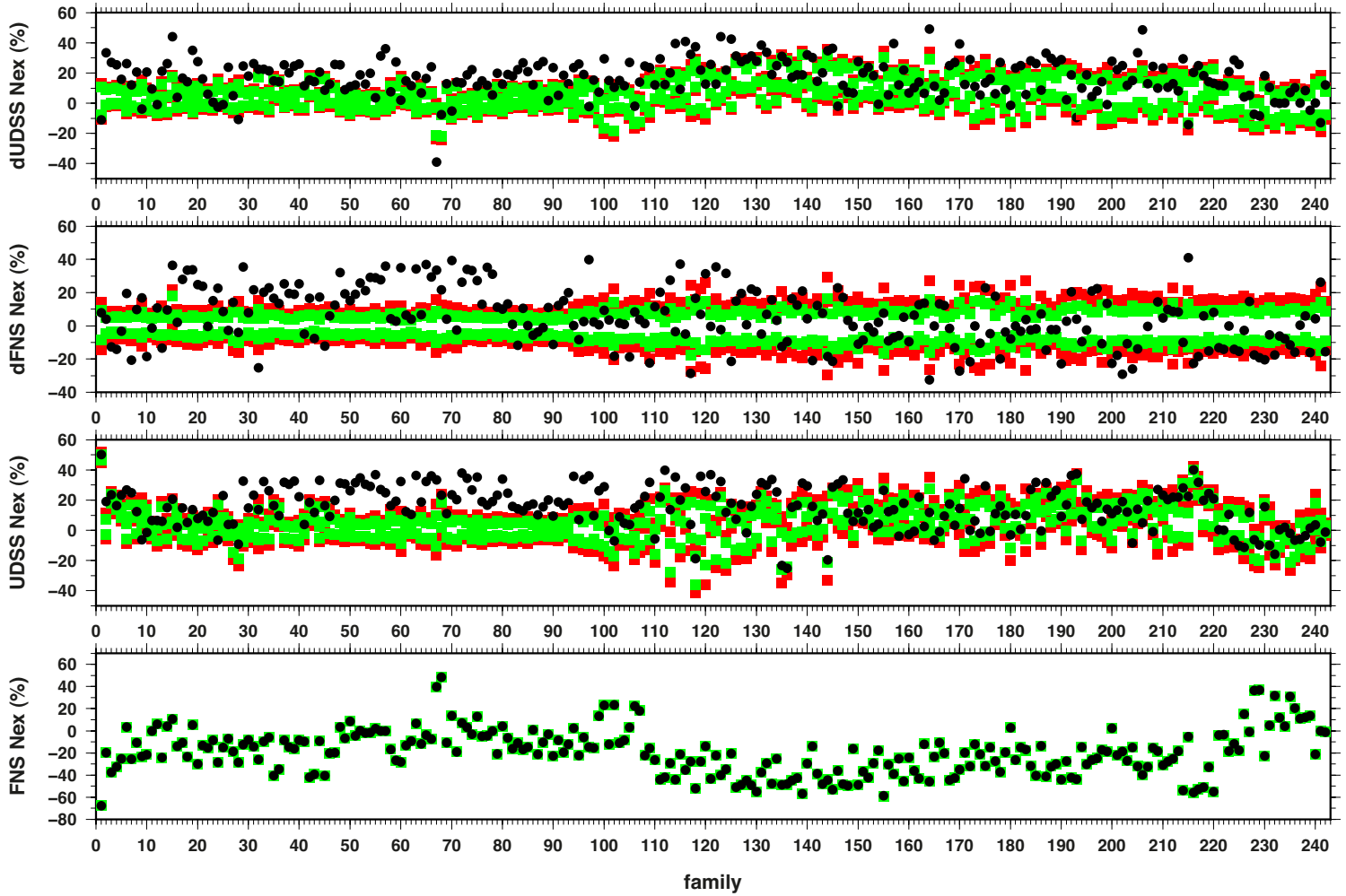

FIGURE B.1: Hypothesis testing results with the null hypothesis that LFEs are influenced by FNS component only. Black dots represent N_{ex} values of the tidal component mentioned in each panel. Green and red squares are the lower and upper limits of the 95% and 99% confidence interval. For the complete methodology, see *Thomas et al.* [2012].